Dissertation

submitted to the

Combined Faculties of the Natural Sciences and Mathematics

of the Ruperto-Carola-University of Heidelberg, Germany

for the degree of

Doctor of Natural Science

Put forward by

Diplom-Physikerin Natalie Miriam Raettig

Born in: Darmstadt, Germany

Oral Examination: October 18th 2012

Global Baroclinic Instability and its Implications on Planet Formation

Referees: Priv.-Doz. Dr. Hubert Klahr

Prof. Dr. Cornelis P. Dullemond

Abstract

In this thesis we analyze a form of non magneto hydrodynamic turbulence which could be described as disk weather since it forms vortices due to baroclinic effects. We want to find out if and how these vortices influences planet formation. The focus is on angular momentum transport and how efficient vortices can trap particles.

We estimate disk properties from observations and derive radial Brunt-Väisälä frequencies as well as cooling time-scales. Then we analyze the baroclinic amplification of vortices and the particle concentration therein. We use 2D as well as 3D local shearing box simulations with the PENCIL CODE to investigate the problems.

In 2D, we conduct a comprehensive study of a broad range of various entropy gradients, thermal cooling and thermal relaxation times covering the parameter space relevant for protoplanetary disks. We measure the Reynolds stresses as a function of our control parameters and see that there is angular momentum transport even for entropy gradients as low as $\beta \equiv -d\ln S/d\ln r = 1/2$. The amplification-rate of the perturbations appears to be proportional to β^2. The saturation level of Reynolds stresses on the other hand seems to be proportional to $\beta^{1/2}$. All entropy gradients will lead to Reynolds stresses of $10^{-3} - 10^{-2}$ which shows that baroclinic vortices are a feasible mechanism for transporting angular momentum.

The concentration of particles of different sizes in baroclinic vortices is first analyzed in 2 dimensions. Because we expect strong particle accumulations, particle feedback onto the gas is included. Particles accumulate inside the vortices and the local dust-to-gas ratios become high enough to trigger the streaming instability even for initial dust-to-gas ratios as low as $\varepsilon_0 = 10^{-4}$.

In 3 dimensional unstratified gas simulations we verify previous result. Once particles, that feel vertical gravity, with normalized friction times of $St = 0.05$and $St = 1.0$, and $\varepsilon_0 = 0.01$ are included, the vortex column in the mid-plane is strongly perturbed. Yet, when the initial dust-to-gas ratio is decreased the vortices remain stable and function as efficient particle traps. Streaming instability is triggered even for the lowest $\varepsilon_0 = 10^{-4}$ and smallest particle sizes ($St = 0.05$) we assumed, showing a path for planetesimal formation in vortex cores from even low global amounts of cm-sized particles.

Zusammenfassung

In dieser Arbeit untersuchen wir eine Turbulenz nicht magnetischer Natur, die auch als "Scheibenwetter" bezeichnet werden kann, da sie, auf Grund barokliner Effekte, Wirbel erzeugt. Wir wollen herausfinden, welchen Einfluss diese Wirbel auf die Planetenentstehung haben. Dabei konzentrieren wir uns auf den Drehimpulstransport, sowie die Möglichkeit Teilchen in den Wirblen zu sammeln.

Aus Beobachtungen leiten wir Scheibeneigenschaften wie die radiale Brunt-Väisälä Frequenz und Zeitskalen für Kühlprozesse her. Dann untersuchen wir die barokline Verstärkung von Wirbeln, und die Ansammlung von Teilchen in diesen Wirbeln. Dazu benutzen wir 2D und 3D Simulationen mit dem PENCIL CODE.

In 2D machen wir eine Parameterstudie, die den für protoplanetare Scheiben relevanten Bereich abdeckt. Dabei variieren wir die Werte des Entropiegradienten $\beta \equiv -d\ln S/d\ln r$, sowie die thermischen Kühl- und Relaxationszeiten. Sogar für so niedrige Entropiegradienten wie $\beta = 0.5$ messen wir Reynoldsspannungen, die zu einem hinreichenden Transport von Drehimpuls führen. Die Wachsumsraten der Wirbel ist proportional zu β^2, wohingegen die Reynoldsspannungen nur proportional zu $\beta^{1/2}$ sind. Für alle verwendeten Entropiegradienten messen wir Reynoldsspannungen zwischen 10^{-3} und 10^{-2}, was beweist, dass barokline Wirbel eine Möglichkeit sind Drehimpuls in protoplanetaren Scheiben zu transportieren.

Wir untersuchen die Konzentration von Teilchen in Wirbeln zu untersuchen in 2D Simulationen aus. Da wir hohe Teilchenkonzentrationen in den Wirbeln erwarten, wird der Einfluss der Teilchen auf das Gas berücksichtigt. Die Teilchen sammeln sich in Wirbeln an. Sogar für solch geringe Anfangswerte des Staub-zu-Gas Verhältnisses wie $\varepsilon_0 = 10^{-4}$ erreichen wir Konzentrationen, die ausreichen um die Strömungsinstabilität auszulösen.

In 3 dimensionalen, ungeschichteten Gassiumlationen können wir vorangegangene Ergebnisse bestätigen. Sobald Teilchen, die die vertikale Gravitation spüren und ein initiales Staub-zu-Gas Verhältnis von $\varepsilon_0 = 0.01$ haben, hinzugefügt werden, wird die Wirbelsäule in der Mittelebene stark gestört. Wird jedoch der Anfangswert des Staub-zu-Gas Verhältnises verringert bleibt die Säule stabil. Selbst für die kleinsten getesteten Teilchen und den niedrigsten Anfangswert des Staub-zu-Gas Verhältnises wird die Strömungsinstabilität ausgelöst. Dies zeigt eine Möglichkeit auf, wie im Inneren eines Wirbels, aus nur geringen Mengen von cm großen Staubteilchen, Planetesimale gebildet werden können.

Contents

List of Figures

List of Tables

Chapter 1

Introduction

1.1 Historical Overview

The question of how our Earth came into existence is as old as humankind itself. While the old Greeks pondered on the question whether there were other worlds besides ours, in the 17th century scientists started to wonder how the Earth and the other planets were formed.

For example, René Descartes (1644) postulated that the Earth was formed out of a vortex with the Sun in its center. For him, the entire universe was filled with aether and full of such vortices. This already suggested that there could be many more Solar Systems in addition to our own.

In 1755, Immanuel Kant proposed a different idea in his *Universal Natural History and Theory of Heaven*. Here, there was a huge nebula in which particles collide, lose energy, eventually forming the Sun. The left over nebula material revolves around the Sun. Condensations in this residual nebula then form the planets. It is interesting that Kant explains the formation of planets such that small particles merely stick together in a first stage and later on, after they have reached a certain size, will gravitationally attract larger bodies: this idea is not too different from today's standard scenario.

Other exponents of these so called nebular hypotheses were Pierre-Simon de Laplace and Young (1832). In their theory, the Solar atmosphere spread out over the entire Solar System. Rings formed in this ellipsoid, from which planets condensed.

A different scenario was capturing, such as the Chamberlin-Moulton hypothesis (Chamberlin, 1901, 1916; Moulton, 1905; Jeans, 1931a). According to them, there was a close encounter between the Sun and another star early on in the Sun's life. This caused a disruption of the Sun's surface which lead to the

eruption of huge flares. Solid bodies, so called planetesimals, condensed out of these flares, and after several collisions with each other formed the planets.

All theses hypotheses were disproved in part or completely over the years. Finally, in the 1940s, Carl-Friedrich von Weizsäcker (1943) took elements of previous hypotheses and combined them with current state of the art physics. He proclaimed that planets are a byproduct of star formation. Around the young central star there is a flat cloud of gas with solar composition, i.e. mostly gas with some heavy elements. In this disk, angular momentum is transported outward and matter inwards towards the star. This transport happens via turbulent eddies which rotate on concentric rings around the planet. On the concentric rings between an "eddy-ring" solid matter is accumulated, which eventually forms planets through collisions.

Although not entirely correct in detail, this picture is the foundation of today's planet formation theory.

1.2 From Star Formation to Protoplanetary Disks and Planet Formation

Today we know that planets form in disks around young stars. A star is born out of a large molecular cloud. Initially, this cloud is in thermal equilibrium, which means that there is a balance between gravitational and pressure forces. Once there is an imbalance and the gravitational forces outweigh the pressure forces, collapse occurs. This is the case when a condensation in the cloud has reached the Jeans mass (Jeans, 1931b). The gas collapses into a disk and a central object. Most of the mass collapses in the center and forms the star (Hoyle, 1960; Cameron, 1962; Terebey et al., 1984), whereas about 30% does not fall directly onto the central object. Since the initial cloud was not static, but rather in rotation, angular momentum conservation leads to the formation of a disk out of this 30%. Eventually most of the disk matter will be accreted onto the star (Hartmann et al., 1998). About 98% of the disk consists of H and H_2. The remaining 2% are heavy elements both in form of micron sized solid material (Mathis et al., 1977) or molecular gas.

A comprehensive theory of disk evolution has to meet many different requirements. For example, it has to explain the redistribution of mass and angular momentum. Most of the mass has to be transported onto the central object, but a small fraction needs to be saved in form of planets, while the angular momentum has to be transported outward or be deposited into the said planets. The process of gas giant formation itself has to be rather fast, since observed disk-lifetimes are only of the order of a few million years (Calvet et al., 2000; Haisch et al., 2001; Sicilia-Aguilar et al., 2006a,b). Another difficulty is that the

observed population of exoplanets, 777 planets on August 5^{th} 2012[1], shows a huge variety of masses, semi-major axes, eccentricities and inclinations. Up until 1995, theorists had concentrated on explaining the Solar System. However, when Mayor and Queloz (1995) found the first exoplanet, it turned out that is was a planet of several Jupiter masses, but on an orbit much closer to its star than Mercury is to our Sun. For these objects the expression "hot Jupiters" was coined.

This shows that planet formation is indeed a complex problem with many stages and outcomes. It is difficult to cover every element of planet formation in one huge theory or simulation. The approach nowadays is rather to divide planet formation into substeps, analyze these substeps individually, and then, in the end, put everything back together in Monte-Carlo simulations and population synthesis models (Mordasini et al., 2009). Of course, the different substeps have to be connected with one another, which leads to an active conversation in this multidisciplinary field.

We now divide our overview on planet formation into two sections, one which deals with disk evolution and angular momentum transport, and the other that focuses on the actual formation of planets.

1.2.1 Disk Evolution

When we talk about disk evolution the questions are how the dynamics work, and what the thermodynamic structure and chemical composition are. Due to rotation and angular momentum conservation, the initial cloud will flatten out and form a thin disk around the star. This disk has a smaller vertical height H close to the star and a larger one further away. Generally the vertical height is small compared to the radial extend of the disk, so that the dimensionless scale-height $h \equiv H/r \ll 1$. Radially, the disk can extend up to a few 100 AU (e.g. Andrews et al., 2009). The upper and lower parts which are illuminated by the star are optically thin, while the inner parts are much colder and optically thick to stellar radiation. A sketch of a vertical cut through a disk is shown in figure 1.1.

Dynamically the disk is likely in near geostrophic balance. This means that the gas does not move on Kepler-orbits with the Keplerian-velocity $u_{\mathrm{K}} = (GM_\star/r)^{1/2}$ where G is the gravitational constant, $M_\star$ the mass of the star and r the distance to the star.

About 2% of the disk mass consists of solid particles. Initially, these particles are spread out homogeneously throughout the entire disk. Due to the vertical component of gravity, they sink down to the mid-plane of the disk.

[1] http://www.exoplanet.org

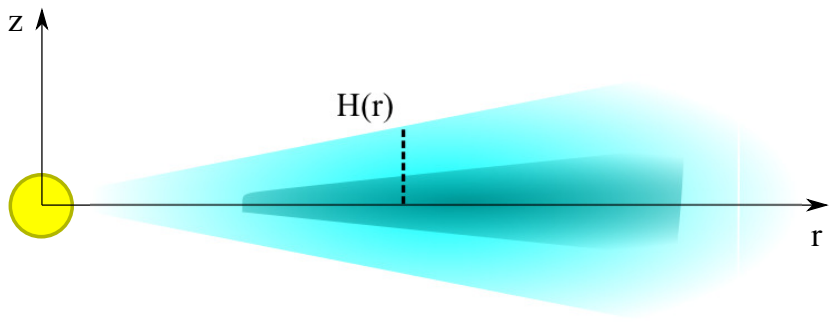

Figure 1.1 Sketch of a protoplanetary accretion disk. Shown is the $r - z$ (radial and vertical) plane. The light blue area indicates the ionized areas of the disk. Here MRI is possible. The dark shaded area is too dust rich to be ionized. Since the MRI cannot exist in this area it is called "dead-zone" (Gammie, 1996; Turner and Drake, 2009).

The larger particles will settle faster than the smaller ones. Once they are in the mid-plane, they drift radially inwards towards the star. How exactly this happens will be described later on in the thesis.

The redistribution of the disk gas happens in a way that matter is locally transported inwards while angular momentum is transported outwards. Since angular momentum is bound to matter it needs to be deposited somewhere. Consequently some of the outer disk gas moves outwards. This is known as viscous spreading (Weizsäcker, 1943; Lüst and Schlüter, 1955; Lynden-Bell and Pringle, 1974).

The question is now, what causes this angular momentum transport? Naively one can think that molecular viscosity ν can take this role. However, the mycrophysical viscous time scale is of the order of 10^{13}yr, which is much longer than the observed life-times of up to 10^{7}yr and even longer than the age of the universe itself (Ji et al., 2006; Armitage, 2009). This means that there has to be another mechanism responsible for the mass transport. Shakura and Sunyaev (1973) proposed that the transport mechanism can be attributed to a turbulent viscosity ν_t with a yet unknown origin. A simple way to parametrize the strength of this viscosity is to estimate the typical length scale and velocity of the system. In a disk this is the scale height of the disk and the local sound speed c_s. This leads to the so called α-prescription

$$\nu_t = \alpha c_s H, \tag{1.1}$$

where α is a dimensionless parameter that describes the strength of the angular momentum transport. From now on we omit the index t for the turbulent viscosity. When we talk about viscosity, we always mean the turbulent viscosity.

One task for astronomers is to find a physical mechanism that can provide α-values which lead to viscosities that match observed accretion rates and life times of disks. This is not an easy task at all. Since the linear stability analysis of the hydrodynamic system leads to the Rayleigh criterium which says that disks are linearly stable when the specific angular momentum increases with increasing radius (Goldreich and Lynden-Bell, 1965; Safronov, 1972; Papaloizou and Pringle, 1984, 1985). This condition is fulfilled in all parts of the disk.

However, once a disk is sufficiently ionized that magnetic fields can couple to the disk gas we get a different picture (Velikov, 1959). If weak magnetic fields are present in the disk, the system will be linearly unstable and infinitesimal perturbations which are applied to the disk will be enough to trigger the unstable state. This effect is known as the magneto-rotational instability (MRI) and was applied to planetary accretion disks for the first time by Balbus and Hawley (1991, 1998). Yet not all parts of the disks will offer the ionization degree needed to start MRI. It seems unlikely that the cold dusty region is adequately ionized for magnetic fields to couple to the gas (see figure 1.1). Therefore this inner region is called "dead-zone" (Turner and Drake, 2009).

Since the precise ionization structure is still under debate (Turner and Drake, 2009), as is the interplay between active and dead-zones, there is still interest in studying purely hydrodynamic turbulence in circumstellar disks. Klahr and Bodenheimer (2003) found such a hydrodynamic instability that creates anti-cyclonic vortices in three-dimensional radiation hydrodynamical simulations of baroclinic disks, which they interpreted to be a kind of baroclinic instability (BI) modified for the Keplerian shear profile. Here, the idea is that observed protoplanetary disks have a non-zero radial entropy gradient $\beta_s \equiv -d\ln s/d\ln r$, where s is the entropy, and are indeed not barotropic but rather baroclinic, which means that planes of constant pressure and constant density are misaligned, driving a thermal wind, e.g. vertical shear. In a linear stability analysis that followed (Klahr, 2004) it was shown that this instability can only be of non-linear nature (see also Cabot, 1984; Knobloch and Spruit, 1986).

Thermal relaxation turned out to be crucial when Petersen et al. (2007a,b) studied baroclinic vortex amplification using an incompressible approximation. In fact, thermal relaxation or diffusion, alongside the entropy gradient, are the key ingredients to establishing the baroclinic feedback that strengthens vortices in baroclinic disks.

1.2.2 Giant and Terrestrial Planet Formation

For the process of planet formation itself, two paradigms were developed: the gravitational collapse model and the core accretion model. Whereas the gravitational collapse model is applicable only to giant gaseous planets, the core accretion model can be used to form both gas giants and rocky planets.

Gravitational Collapse Model

The idea of the gravitational-collapse model for planet formation is basically the same as for gravitational collapse leading to star formation. The only difference is that the action takes place in a protoplanetary disk instead of a huge amorphous cloud. The gas in a cloud or disk collapses when self-gravity and thermal pressure are no longer in equilibrium. This occurs when gravity is stronger than thermal pressure, which tries to push matter apart. Instability can be determined through the Toomre-parameter (Toomre, 1964).

$$Q = \frac{c_s \Omega}{\pi G \Sigma}. \tag{1.2}$$

Here c_s is the sound speed, G the gravitational constant, Σ the gas surface density in the disk, and Ω the angular frequency. The Toomre-parameter balances pressure against gravity. If $Q \lesssim 1$ collapse can occur. But for this to happen there are several constraints that the disk must meet. It must remain nearly isothermal by cooling sufficiently fast: the collapse time, controlled by the cooling time, has to be shorter than the shear time-scale. Otherwise, shear will tear the collapsing clump apart (Janson et al., 2012). Conditions which allow for collapse are only likely to appear in protoplanetary disks at large radii (e.g. Boss, 1997, 2000, 2007; Rice et al., 2005; Meru and Bate, 2010).

Core Accretion Model

Roughly speaking, the gravitational collapse model works from large scale to small scale. The core accretion on the other hand starts at the smallest scales and grows to large ones (Mizuno, 1980; Pollack et al., 1996). Most of the dust is initially in μm size (Mathis et al., 1977). When these particles collide they simply stick together and thus grow to larger bodies (Dominik and Tielens, 1997). Unfortunately this hit-and-stick mechanism cannot go on to arbitrary sizes. Eventually dust aggregates will be too large and their collisional velocities too high to merely stick. Instead, they fragment into small pieces (Dullemond and Dominik, 2005; Tanaka et al., 2005; Blum and Wurm, 2008; Brauer et al., 2008). Recently even more barriers have been found in addition to this fragmentation barrier. Zsom et al. (2010) and Güttler et al. (2010) found the bouncing barrier,

where particles bounce off of each other and Okuzumi (2009); Okuzumi et al. (2011a,b) found the charging barrier, where particles repel each other due to the intrinsic electrical charge they bear. Even if particles overcome all these barriers, their radial drift becomes very fast: they will drift into the star before growing to bodies massive enough to accrete further matter (Birnstiel et al., 2010).

A mechanism to circumvent this critical size regime is needed. One proposed by Goldreich and Ward (1973) is the gravitational collapse of particles. For this a high overdensity of particles needs to be reached. In a disk without turbulence these high density enhancements can be reached via dust sedimentation. However, Weidenschilling (1980) found that even in a laminar disk, dust sedimentation induces a vertical shear which can lead to the Kelvin-Helmholz instability and thus prevents gravitational collapse. More recently, however, Johansen et al. (2006a) found that turbulence can actually help the concentration process. They showed that sufficiently decoupled dust can accumulate in high pressure regions induced by the MRI. If these accumulations reach high enough densities then gravitational collapse can happen, directly forming planetesimals which are both large enough not to be strongly affected by radial drift, and also massive enough to gravitationally accrete smaller dust grains.

Once there are many planetesimals in a disk, they can form planetary cores or planetary embryos. Eventually gas will also be accreted (e.g. Wetherill and Stewart, 1989; Thommes et al., 2003; Armitage, 2009; Ormel et al., 2010). When the solid core and gaseous envelope have similar mass, contraction happens and cooling becomes very efficient. Gas runaway accretion starts and will go on until the planet's feeding zone is empty (Mizuno, 1980): a giant gas planet has formed. Terrestrial planets can also form via this mechanism, although they do not reach the phase of gas accretion and therefore stay small.

Additional effects like migration (e.g. Papaloizou and Lin, 1984; Ward, 1997; Masset, 2002; Tanaka et al., 2002; Bate et al., 2003; Papaloizou et al., 2007), the Kozai-mechanism (Kozai, 1962; Lithwick and Naoz, 2011) or mean motion resonances among planets (Weidenschilling and Davis, 1985) are responsible for the final location of the planet.

1.3 About this Thesis

Two of the challenges for protoplanetary disk and planet formation theory that were mentioned in the introduction are the mechanism by which angular momentum transport occurs in weakly ionized disks and how planetesimals

form. These are points that I want to focus on in this thesis, especially how the baroclinic instability can contribute to the solution of these challenges.

First the disk properties need to be determined, before I can analyze the properties of baroclinic vortices in accretion disks. This is done in chapter 2.

Once disk parameters like the Brunt-Väisälä frequencies and cooling processes are constrained, the focus is shifted to the baroclinic instability, or more exactly, on the baroclinic vortex amplification (BVA). The goal of this chapter is to show whether baroclinic vortices can exist in accretion disks and, if they do, to determine the strength of the angular momentum transport. To do this I conduct an extensive parameter study using the parameters that were determined in chapter 2. Special attention is paid to the dependence of growth-times and α-values on the global entropy gradient β_s.

In chapters 4 and 5 I will analyze the particle accumulation in baroclinic vortices. Here the goal is to find out how much of a certain particle species is needed to achieve conditions that may lead to gravoturbulent planetesimal formation.

In chapter 4 2 dimensional simulations of a baroclinic disk with particles of various sizes ($St = 0.01$, $St = 0.05$, $St = 1.0$ and $St = 20.0$) will be performed. The particle concentration inside the vortices will be measured. I will not only perform simulations with an initial dust-to-gas ratio of $\varepsilon_0 = 0.01$ but also decrease this value to $\varepsilon_0 = 10^{-3}$ and $\varepsilon_0 = 10^{-4}$ to see with how much material is required to achieve high levels of particle accumulation can be achieved. Additionally, collisional velocities between particles will be measured, and compare those results to studies of particle collisions in a different kind of turbulence, see e.g. Ormel and Cuzzi (2007).

In chapter 5 the 2 dimensional simulations are extended to 3 dimensional ones. Here the gas is vertically unstratified but vertical gravity is included for particles which is appropriate for highly settled particles. We will briefly compare pure gas simulations with the literature (Lesur and Papaloizou, 2010; Lyra and Klahr, 2011) and then include $St = 0.05$ and $St = 1.0$ particles. Again different initial dust-to-gas ratios are tested to see the effects that different particle concentrations have onto the vortex structure and to analyze the efficiency of vortex trapping.

Finally, I conclude in chapter 6.

Chapter 2

How Baroclinic are Accretion Disks?

2.1 Introduction

The linear stability of a barotropic rotating fluid depends on the radial shear rate (Rayleigh Criterion). More precisely, if the specific angular momentum j increases radially then the fluid is stable and if it decreases radially, turbulence is generated (e.g. the Princeton Experiment: Schartman et al. (2006)). This stability criterion is met in accretion disks, where $j \propto R^{1/2}$ as well as in rigidly rotating planetary atmospheres with $j \propto R^2$. One speaks of a barotropic stable flow. Without applying additional physics to the system, the flow will remain stable indefinitely and no turbulence can be expected. In accretion disks this additional physics can be, for instance, self-gravity for sufficiently cold and massive disks or it can be magnetic fields leading to the magneto-rotational instability (Balbus and Hawley, 1991) if the disk is sufficiently ionized.

The earth atmosphere on the other hand is little impressed by self gravity or magnetic fields. Instabilities such as local winds, atmospheric circulation, cyclonic and anti-cyclonic storms, jet streams and many more exist. This entire manifold of non-laminar flows is created due to local temperature gradients or global temperature gradients between equator and poles (Vallis, 2006). In a non-rotating system these temperature gradients (which also form pressure and entropy gradients) would lead to large convective cells between the equator and the arctic regions, yet Coriolis forces do not permit such large scale flows. Therefore a northward push of warm air leads to a thermal wind in the easterly direction (in the northern hemisphere of the earth) until the pressure gradient gets compensated by the additional centrifugal acceleration above the mean rotation rate of the earth. Likewise the colder equator ward flow generates a wind in the westerly direction and if both patches of air are on top of each other (warm over cold) then this will lead to vertical shear between the

westerly blowing colder air and the easterly blowing warmer air on top of it. This thermal wind phenomenon is the basic state of the baroclinic instability in planetary atmospheres.

The baroclinic instability occurs in non-axisymmetric modes where the warm air is sliding in the opposite direction of the colder air below, thus releasing potential energy (for a detailed discussion see the book by Vallis, 2006). For the baroclinic instability in planetary atmospheres, one can assume a rigid rotating fluid, in which case the non-axisymmetric perturbations can not be sheared out. This instability has also been studied in the interior of rotating stars (Tassoul, 2000) and has been discussed in the context of accretion disks (Cabot, 1984). Nevertheless Knobloch and Spruit (1986) have shown in their work that radial buoyancy is too small in comparison to the radial shear, thus the baroclinic instability as described above is prevented form operating.

Nevertheless, we want to stress that the thermal wind phenomenon occurs in all accretion disks because they cannot be stricktly barotropic, e.g. have the same entropy everywhere. In other words, a strictly isentropic disk would be too special a case to be realized in nature. In general, temperature and density decrease with distance from the star. The first is partly an effect of lesser stellar heating at larger distance from the star. In addition, at least for disks which actively accrete matter onto their central object, the release of potential energy per accreted mass is also much stronger in the steeper potential well closer to the star than further away from the center of gravity. The density decreases radially because of several effects. First, the residual vertical gravity in the system corotating with the disk at a certain radius falls off with distance, compressing the disk less vertically. Second, dumping angular momentum rich mass from the molecular cloud onto a disk results in high densities close to the star and lower densities at larger distances for geometrical reasons. Third, in order to maintain a constant accretion rate $\dot{M} \sim \Sigma\nu \sim \rho r\nu$ for a viscous lifetime of the entire disk, surface density of the disk gas has to scale inversely to the viscosity in the gas. In protoplanetary accretion disks we typically find radially increasing kinematic viscosities (see also the α prescription of Shakura and Sunyaev (1973) $\nu = \alpha H^2\Omega \sim r^{1/2}$) and therefore densities have to decrease radially. The combination of thermal and density gradient may then create vertical shear, e.g. a thermal wind, which should be common to all these disks. The subject of this chapter is to discuss the detailed structure of local radial pressure gradients vs. entropy gradients. We will see that the heat trapping properties of the opacity will strongly determine the direction in which entropy gradients will point.

While studying thermal convection in global models of protoplanetary accretion disks, Klahr and Bodenheimer (2003) found anti-cyclonic vortices forming in their 3D radiation hydrodynamical models. When they simplified the numerical set up to 2D vertically integrated models, thus removing the vertical

convective motion of the disk, they still found the formation of vortices when there was a radial entropy gradient. In simulations where this gradient was set to zero, no vortices formed. Inspired by this finding they proposed that a baroclinic instability might be responsible for this phenomenon. Yet Klahr (2004) and others (Johnson and Gammie, 2005) found no linear instability for typical values of the radial buoyancy in protoplanetary disks. Buoyancy shall here refer to the radial Brunt-Väisälä frequency:

$$N^2 = -\frac{1}{\gamma}\left(\frac{H}{r}\right)^2 \beta_K \beta_p \Omega^2, \tag{2.1}$$

with γ the adiabatic index of the gas, $\beta_K = -d\ln K/d\ln r$ the radial entropy[2] and $\beta_p = -d\ln p/d\ln r$ the radial pressure gradient. Even the Brunt-Väisälä frequency might be imaginary, indicating radial buoyancy, one has to compare the growth rates to the shear rate in the disk, which is expressed in the Richardson number

$$Ri = -\frac{2}{3\gamma}\left(\frac{H}{R}\right)\beta_K \beta_p. \tag{2.2}$$

Positive values larger than a critical threshold, $Ri > Ri_c$ indicate that shear destabilizes the system despite stabilizing radial stratification, typically leading to a Kelvin-Helmholz instability. If on the other hand $Ri < -1$ then buoyancy leads to radial convection, as the shear is too weak to suppress it. Yet, as we will discuss in the following sections in detail, the expected range of Richardson numbers is negative, but $\mid Ri \mid \ll 1$. Thus shear stabilizes the radial buoyancy, or in other words the linear growth rates of perturbations in vorticity, due to the radial buoyancy, are lower than the shear rates in these disks. Nevertheless, vorticity indeed grows in baroclinic disks, not in an exponential way, but only linearly (see Klahr, 2004).

The baroclinic instability in its formulation for a planetary system cannot spontaneously form vortices in disks, as they would immediately be suppressed by shear. Nonetheless, while the initial formation of vortices in protoplanetary disks from small perturbations is still a poorly understood problem[3], there has been progress for the non-linear stage of the perturbation. Recently,

[2]Actually, K is the potential temperature which is connected to the entropy s via $s = c_v \ln K/K_0$, where c_v is the specific heat at constant volume. In the next chapter we will change our notation and rather use entropy s instead of K.

[3]Please note that the Papaloizou Pringle Instability (1984) (see Lovelace et al. (1999); Li et al. (2000, 2001) for a more general formulation as Rossby-Wave Instability) can form vortices from infinitesimal perturbations, but needs a sufficiently strong local extremum in potential vorticity. Such a local extremum might be produced at interfaces between magnetically active and dead zones of a disk (see Varnière and Tagger (2006); Lyra and Mac Low (2012)), but this must be a local phenomenon and can most likely not be invoked as the source for the majority of vortices in baroclinic accretion disks. Studies of the dynamics of Rossby Wave generated vortices in baroclinic disks with thermal relaxation are still missing.

Petersen et al. (2007a,b) have shown that vortices in baroclinic disks are amplified when there is a sufficiently strong thermal relaxation process operating, turning the vortices into entropy transporting radial convection cells. The strength of the amplification depends on the strength of the radial buoyancy, the viscosity of the fluid and the thermal relaxation rate of the dusty gas. In chapter 3 we perform a parameter study for such systems and find an amplification of vortices even for the low radial buoyancy of $N^2 = -1.78 \times 10^{-3}$.

The occurrence of the baroclinic instability, or more precisely the amplification and growth of vortices, depends on critical parameters like the entropy and pressure gradients as well the thermal relaxation of the disk (Petersen et al. (2007a,b); Klahr (2004) and chapter 3). In the past, there have been many modelling studies (Bell et al., 1997; D'Alessio et al., 1998; Dullemond et al., 2006) on the thermodynamic structure of observed disks (Hartmann et al., 1998; Sicilia-Aguilar et al., 2006a,b; Andrews et al., 2009, 2010). We take these models one step further to derive the parameters controlling the baroclinic state of the disk for real observed disks from star formation regions, like in the Ophiuchus cloud.

Andrews et al. (2009, 2010) used observed radial density profiles and modelled them with viscous accretion disk models, e.g. by calculating an α viscosity value for the measured mass accretion rate. Using their best fits to the radial surface density profiles

$$\beta_\Sigma = -\frac{d\log\Sigma}{d\log r} = 0.9 \pm 0.2 \tag{2.3}$$

we can already estimate that the viscosity profile is $\nu \propto r^{\beta_\Sigma}$ because a steady state accretion disk has to possess a radially constant accretion rate $\partial_r \dot{M} = \partial_r \Sigma \nu = 0$. Using the α ansatz, $\nu = \alpha c_s^2/\Omega$ determines the radial temperature gradient to be

$$\beta_T = -\frac{d\log T}{d\log r} = 1.5 - \beta_\Sigma = 0.6 \pm 0.2, \tag{2.4}$$

for a constant α. It might seem as a surprise that the pressure has a constant slope of

$$\beta_p = -\frac{d\log p}{d\log r} = 1.5, \tag{2.5}$$

independent of the radial density profile, but this is a consequence of constant accretion rate and the original hypothesis of Shakura and Sunyaev (1973) that viscous stresses are proportional to the local pressure. The entropy gradient can now be derived from the temperature and surface density gradients ($\beta_K = \beta_T - [\gamma - 1]\beta_\Sigma$) as

$$\beta_K = -\frac{d\log K}{d\log R} = 1.5 - \gamma\beta_\Sigma = 0.28 \pm 0.27, \tag{2.6}$$

with K as a potential temperature like representative for entropy following the polytropic equation of state $p = K\Sigma^\gamma$ with $\gamma = 1.353$ the 2D adiabatic index. These values are always positive, indicating the unstable regime of entropy gradients, violating the radial Schwarzschild criterion as expressed by negative values for the square of the Brunt-Väisälä frequency $N^2 < 0$.

Bell et al. (1997) (see also D'Alessio et al., 1998) have shown that accretion disks even with a radially constant α value can not be modelled by a single temperature and density slope. The temperature dependence of the Rosseland mean opacity defines the temperature gradient between the midplane T_c and the surface of the disk $T_{\rm eff}$ via the optical depth τ_R, thus $T_c^4 \approx \left(\tau_R + \frac{1}{\tau_R} + const\right) T_{\rm eff}^4$ (see Hubeny, 1990, for a detailed discussion) with *const* being a constant. While it is easy to investigate the structure of a disk that is already more or less uniquely defined by these two parameters, it is awkward to study the stability properties of a disk which by construction must be already unstable by one mechanism or another in order to have a non-zero accretion rate and thus a non-vanishing α value. In the best case we can ultimately only study whether a disk with already acting turbulence is able to maintain a baroclinically unstable structure, allowing baroclinicity to be the continuous driver of the turbulence. If on the other hand we find accreting disks to have typically a baroclinic stable stratification, i.e. $N^2 > 0$, then we have shown that the turbulence in these regions is incompatible with driving from baroclinic effects.

First we summarize what would be expected for the radial entropy gradients from various disk modeling attempts, where accretion luminosity is neglected. Afterwards we describe our 1+1D modeling of accreting and illuminated accretion disks. Then we summarize our results.

2.2 Thermodynamic Structure of Disks

2.2.1 Non-Accreting Disks

Passively illuminated disks have been widely studied for the interpretation of observations of passive disks around T Tauri stars (Natta et al., 2000). The disk geometry and density structure described by Chiang and Goldreich (1997, 1999) has a very steep surface density gradient of $\beta_\Sigma = 1.5$. Thus in order to have radial decreasing entropy, the temperature has to drop faster than $\beta_T > 0.53$, which is not the case in the modelling of spectral energy distributions as was done in Chiang and Goldreich (1999); but note that the surface density profile fit is biased by the slope at large radii whereas little can be concluded from this study for the local surface density profiles at distances $R < 10\,\mathrm{AU}$,

especially when accretion luminosity has to be considered. The surface density distributions assumed in the Pascucci test (2004), on the other hand, assume such a shallow surface density profile that any temperature gradient $\beta_T > 0$ would produce a positive entropy gradient value β_K as well.

2.2.2 Accreting Disks

In the following we will directly use models of disks which include both irradiation and accretion luminosity. As pointed out by Dullemond et al. (2007) a profile as steep as $\beta_\Sigma = 1.5$ would require a completely flat temperature distribution which is inconsistent with a constant accretion rate and α viscosity.

As was pointed out by Bell et al. (1997) an accreting disk can not have a constant surface density profile ($\beta_\Sigma = const$) for all radii. For a given global accretion rate $\dot{M}$ and viscosity parameter α, the local surface density is a function of the local optical depth of the disk and thus of the temperature dependent Rosseland mean opacity κ of the dust grains. For the opacities we use the table provided in Bell and Lin (1994).

D'Alessio et al. (1998, 1999, 2001) have provided data sets for irradiated accretion disks and we checked our own simulation results against their data. The D'Alessio data itself was too coarse to determine smooth local temperature and surface density gradients, and thus we had to run our own models based on Bell et al. (1997), with the inclusion of irradiation.

1+1D disks models

The determining parameters for these models are the accretion rate $\dot{M}$ and the viscosity value α. The first parameter sets the local accretion luminosity, while as the second parameter determines the value of surface density Σ needed to achieve $\dot{M}$. The accretion (effective) temperature of the disk, if not irradiated, is

$$\sigma T_{\rm acc}^4 = \frac{3\dot{M}\Omega^2}{8\pi}\left(1-\sqrt{\frac{R_\star}{r}}\right) \tag{2.7}$$

with σ the Stefan-Boltzmann constant, R_* the stellar radius and Ω the Keplerian frequency at disk radius r. To calculate the total effective temperature of the disks one has to add the irradiated flux $F_{\rm irr} = \sigma T_{\rm irr}^4$ thus

$$T_{\rm eff}^4 = T_{\rm acc}^4 + T_{\rm irr}^4. \tag{2.8}$$

The irradiation temperature can be calculated from the stellar effective temperature $T_\star$ and stellar radius under the simplifying but not crucially relevant

assumption of an impact angle $\theta \approx 0.05 \sim H/r$ between disk surface and incoming radiation (see Dullemond et al. 2006):

$$T_{\mathrm{irr}} = T_\star \left(\frac{R_\star}{r} \right)^{1/2} (\sin\theta)^{1/4} . \tag{2.9}$$

To solve for the vertical structure of the disk we use a shooting method as described in Bell et al. (1997) to simultaneously solve 3 equations. The first for hydrostatic pressure p

$$\partial_z p = -g_z \rho, \tag{2.10}$$

with $g_z = -\Omega^2 z$ the vertical component of stellar gravity and ρ the gas density. The second for vertical heat transport via flux limited diffusion of radiation energy density

$$\partial_z T(z) = -\frac{\kappa \rho F(z)}{4 a_R c \lambda T(z)^3} \tag{2.11}$$

with $F(z)$ the radiative flux at z, a_R the radiation constant, c the speed of light and λ a Levermore and Pomraning like flux limiter. Finally a third equation for the local generation of heat flux due to viscous dissipation

$$\partial_z F(z) = \frac{9}{4} \frac{G M_\star \nu \rho}{r^3}. \tag{2.12}$$

As mentioned before, the resulting values for vertically integrated density Σ and pressure p agree well with the tabulated values provided by d'Alessio.

As a test case we plot in figure 2.1 the radial structure for a disk with $\dot{M} = 1 \times 10^{-7}\, M_\odot/\mathrm{yr}$, an assumed efficiency of turbulent diffusion of angular momentum of $\alpha = 3 \times 10^{-3}$ around a T-Tauri star with $T_\star = 4300\, K$ and $R_\star = 2\, R_\odot$ (model test in table 2.1). The dotted line shows in the temperature plot shows the disk surface temperature if the disk was only heated up by viscous accretion whereas the dashed line shows the temperature of the disk if it was only heated via irradiation. At inner radii, the surface temperature of the disk (lower solid line in the plot) is dominated by viscous heating. Since the surface temperature is a combination of both heating processes, and also because the optical depth changes with radius and height, the surface temperature no longer has a constant slope. This also reflect in the derived mid-plane temperature and surface density. These values can be translated into gradients for vertical integrated pressure (see figure 2.2) β_p and entropy β_K as well as an effective $\beta = \sqrt{\beta_p \beta_K}$ value as controlling parameter for the numerical experiments we conduct in chapter 3. Note that the derived gradients are no longer constant and include spikes as a result of including irradiation as well as viscous heating and the integration. Also the model is not vertically isothermal, so the temperature varies vertically. Therefore the gradient of the vertically integrated pressure is no longer $\beta_p = 1.5 = const$, but varies radially.

Table 2.1. Models

model	$\dot{M}$ $\left(M_\odot \mathrm{yr}^{-1}\right)$	α
test	1×10^{-7}	3×10^{-3}
Oph1	1×10^{-7}	8×10^{-2}
Oph2	1×10^{-8}	3×10^{-3}
Oph3	3×10^{-9}	5×10^{-4}
Oph4	3×10^{-10}	6×10^{-4}

Finally we calculate the Richardson number for this model in figure 2.3 along with the thermal diffusion time for the model as it follows from opacity, temperature and density in the mid-plane of the disks, calculated as

$$\tau_{\mathrm{diff}} = H^2/D = \frac{H^2 \rho \kappa}{\lambda 4 c a_R T_{\mathrm{eff}}^3}. \tag{2.13}$$

Ophiuchus Models

For the disks in the Ophiuchus star forming region we took the data of four representative cases from Andrews et al. (2009, 2010) (see table 2.1). We did not vary the stellar properties in the derivation of the 1+1D disk structures, but this could be done in future studies.

As one can see from figures 2.4 - 2.11 in all of the studies cases one finds extended regions with radially pointing outward pressure and entropy, which also reflects in the negative Richardson numbers. Only the inner about 0.2 AU of three of the disks show positive values (of $-\beta_K$), which indicates stability with respect to baroclinic vortex amplification, e.g. stable radial stratification. The reason for this inverse entropy gradient lies in the radially increasing optical depth in this region, because of the shape of the inner dust evaporation front. Regardless, as soon as dust is evaporated the MRI works perfectly, and the baroclinic effects do not have to be invoked to drive angular momentum transport. It is also interesting to note that the disks have more strongly negative Richardson numbers with increasing values α, which would be expected if radial buoyancy drives the disk evolution. Thermal relaxation is typically between a tenth and 100 local orbital periods, values that in numerical experiments also lead to the excitation of baroclinic vortices.

2.3 Discussion and Conclusions

In this chapter we derived disk properties using a 1+1D model. The model is based upon a constant accretion rate $\dot{M}$ and constant α value. For the effective temperature the accretion temperature as well as the irradiation temperture from the central star were considered. As reference values for $\dot{M}$ and α we use disk properties derived by Andrews et al. (2009, 2010) from observations of the Ophiucus star forming region.

The derived disk structures show radially declining entropy for all sample disks except for the very inner region of some of the disks. The modeling parameter for our numerical experiments in the next chapter $\beta = \sqrt{\beta_p \beta_K}$ shows values between 0.2 up to 1.5. The necessary condition for baroclinic instability $-1 < Ri < 0$ is fulfilled in most parts of the disk. The radii where this condition is not fulfilled coincide with radially increasing entropy. A wide radial range meets the necessary requirements of the baroclinic instability.

Another important modeling parameter for baroclinic vortex amplification is the thermal diffusion time. Its values lie between 0.1 orbital periods, in the outer parts of the disk, and 100 orbital periods. This gives us all relevant parameters for conducting our numerical experiments in the next chapter.

For the modeling in this chapter we kept the stellar parameters ($R_\star$ and $M_\star$) constant. For future studies these properties should also be varied.

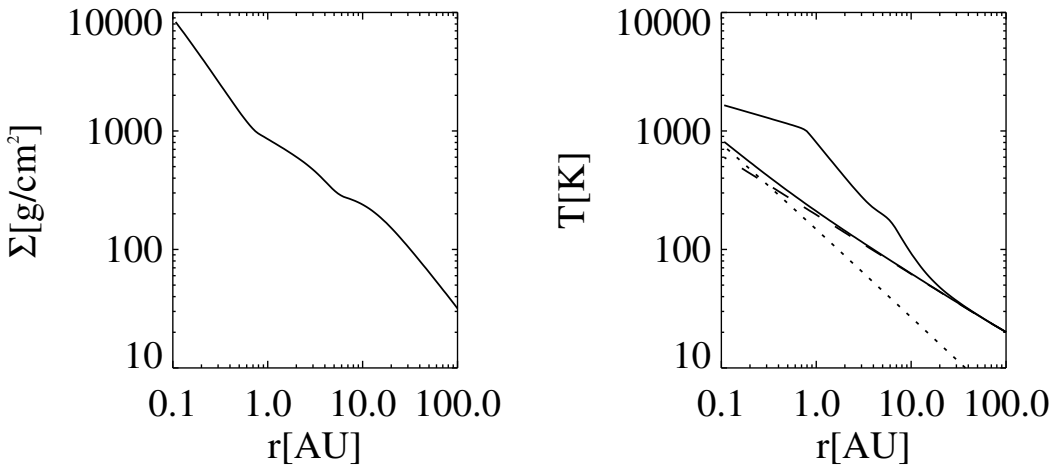

Figure 2.1 Temperature and surface density structure of a protoplanetary accretion disk with an accretion rate of $\dot{M} = 1 \times 10^{-7} M_{\odot}/\mathrm{yr}$, an assumed efficiency of turbulent diffusion of angular momentum of $\alpha = 3 \times 10^{-3}$ around a T-Tauri star with $T_{\mathrm{eff}} = 4300K$ and $R_{\star} = 2R_{\odot}$ (model test in table 2.1). The dashed line is the surface temperature if the disk was only heated by stellar radiation and the dashed line shows the surface temperature if the disk was only heated up via viscous heating. these two processes make up the effective surface temperature (lower solid line). The upper solid line shows the derived mid-plane temperature.

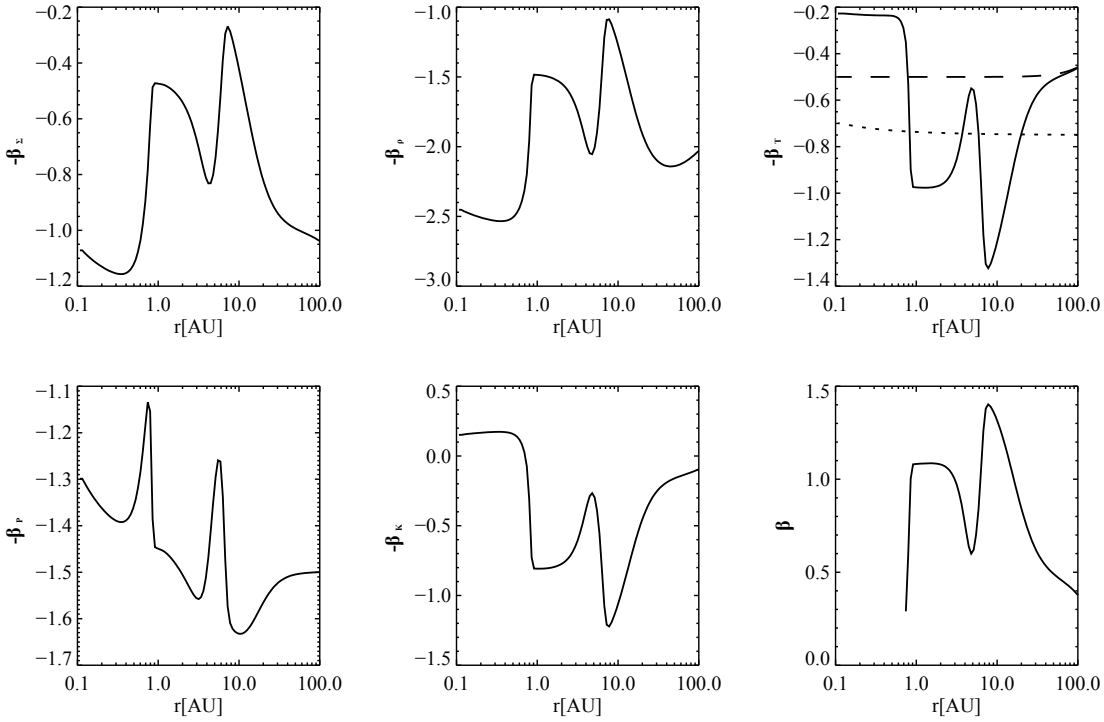

Figure 2.2 Radial gradients in a protoplanetary accretion disk with an accretion rate of $\dot{M} = 1 \times 10^{-7} M_{\odot}/\mathrm{yr}$, an assumed efficiency of turbulent diffusion of angular momentum of $\alpha = 3 \times 10^{-3}$ around a T-Tauri star with $T_{\mathrm{eff}} = 4300K$ and $R_{\star} = 2R_{\odot}$ (model test in table 2.1).

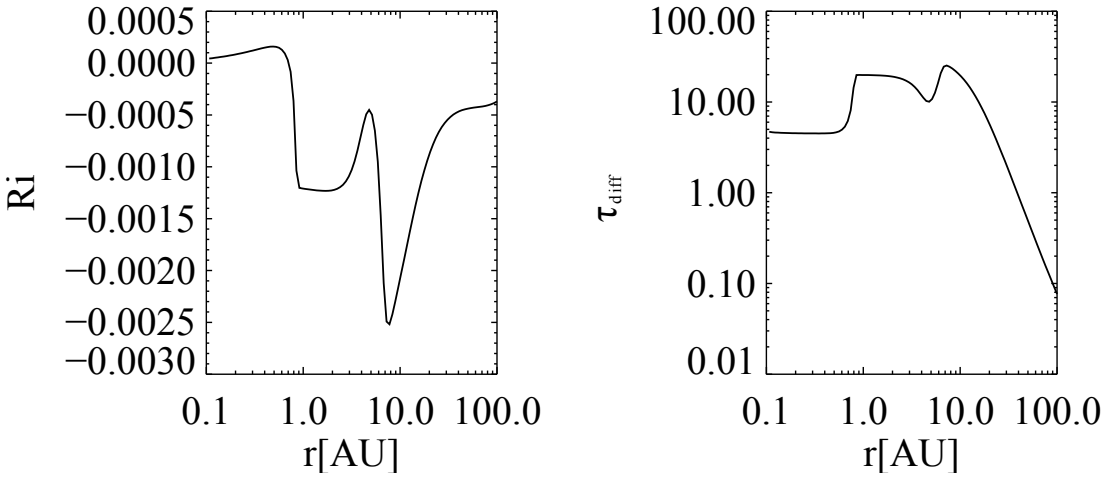

Figure 2.3 Richardson number and thermal diffusivity in a protoplanetary accretion disk with an accretion rate of $\dot{M} = 1 \times 10^{-7} M_{\odot}/\mathrm{yr}$, an assumed efficiency of turbulent diffusion of angular momentum of $\alpha = 3 \times 10^{-3}$ around a T-Tauri star with $T_{\mathrm{eff}} = 4300K$ and $R_{\star} = 2R_{\odot}$ (model test in table 2.1).

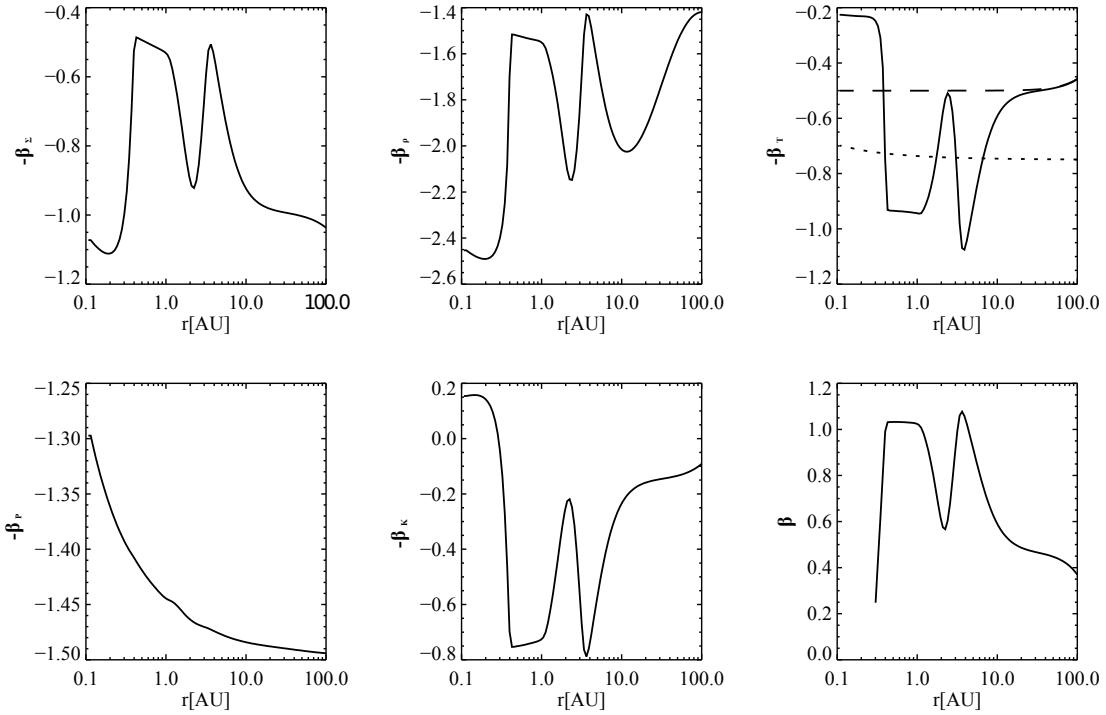

Figure 2.4 Radial gradients in a protoplanetary accretion disk with an accretion rate of $\dot{M} = 1 \times 10^{-7} M_\odot/\mathrm{yr}$, an assumed efficiency of turbulent diffusion of angular momentum of $\alpha = 8 \times 10^{-2}$ around a T-Tauri star with $T_{\mathrm{eff}} = 4300K$ and $R_\star = 2R_\odot$ (model Oph1 in table 2.1).

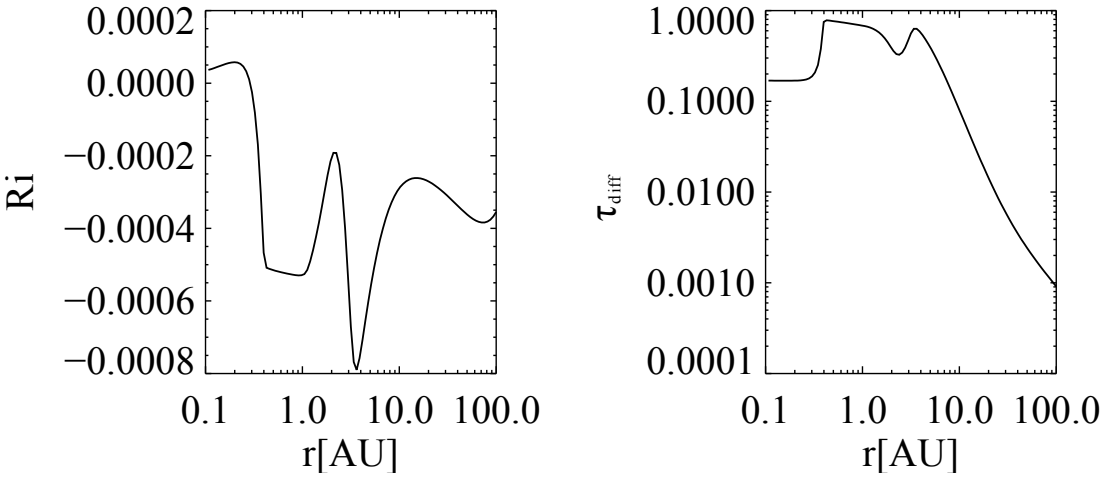

Figure 2.5 Richardson number and thermal diffusivity in a protoplanetary accretion disk with an accretion rate of $\dot{M} = 1 \times 10^{-7} M_\odot/\mathrm{yr}$, an assumed efficiency of turbulent diffusion of angular momentum of $\alpha = 8 \times 10^{-2}$ around a T-Tauri star with $T_{\mathrm{eff}} = 4300K$ and $R_\star = 2R_\odot$ (model Oph1 in table 2.1).

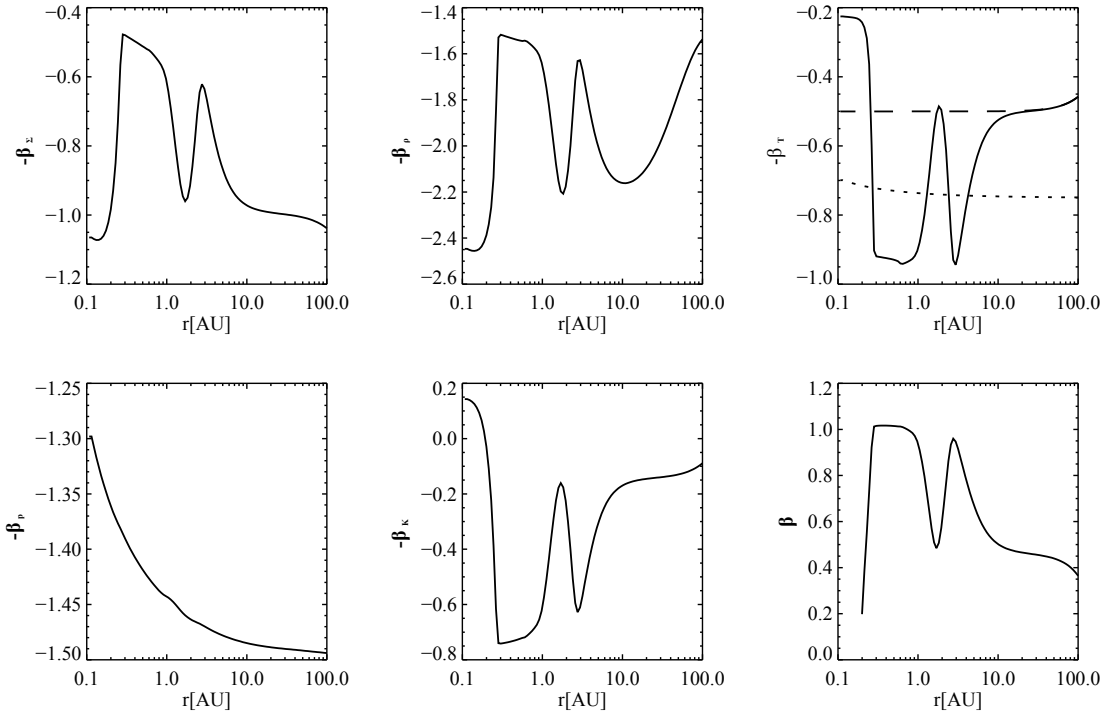

Figure 2.6 Radial gradients in a protoplanetary accretion disk with an accretion rate of $\dot{M} = 1 \times 10^{-8} M_\odot/\mathrm{yr}$, an assumed efficiency of turbulent diffusion of angular momentum of $\alpha = 3 \times 10^{-3}$ around a T-Tauri star with $T_{\mathrm{eff}} = 4300K$ and $R_\star = 2R_\odot$ (model Oph2 in table 2.1).

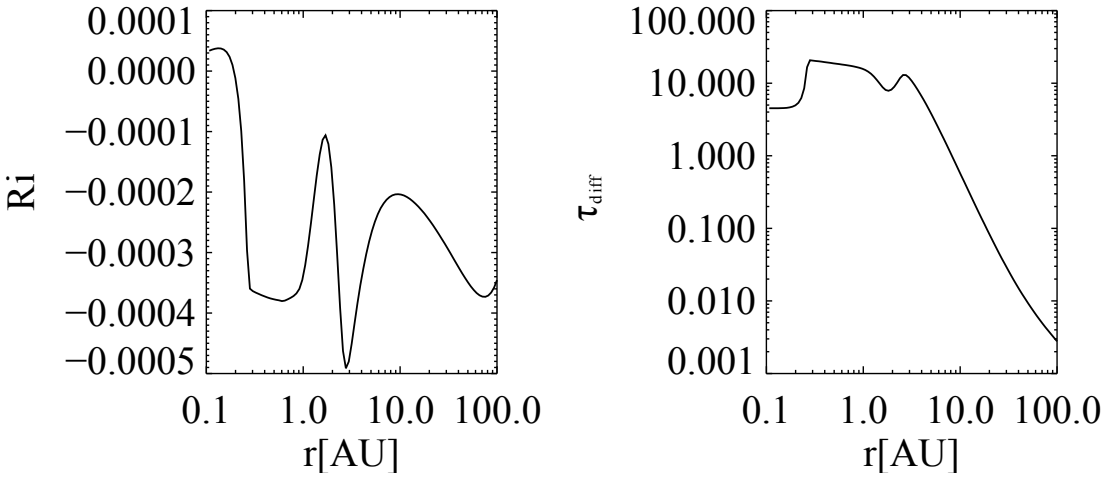

Figure 2.7 Richardson number and thermal diffusivity in a protoplanetary accretion disk with an accretion rate of $\dot{M} = 1 \times 10^{-8} M_\odot/\mathrm{yr}$, an assumed efficiency of turbulent diffusion of angular momentum of $\alpha = 3 \times 10^{-3}$ around a T-Tauri star with $T_{\mathrm{eff}} = 4300K$ and $R_\star = 2R_\odot$ (model Oph2 in table 2.1).

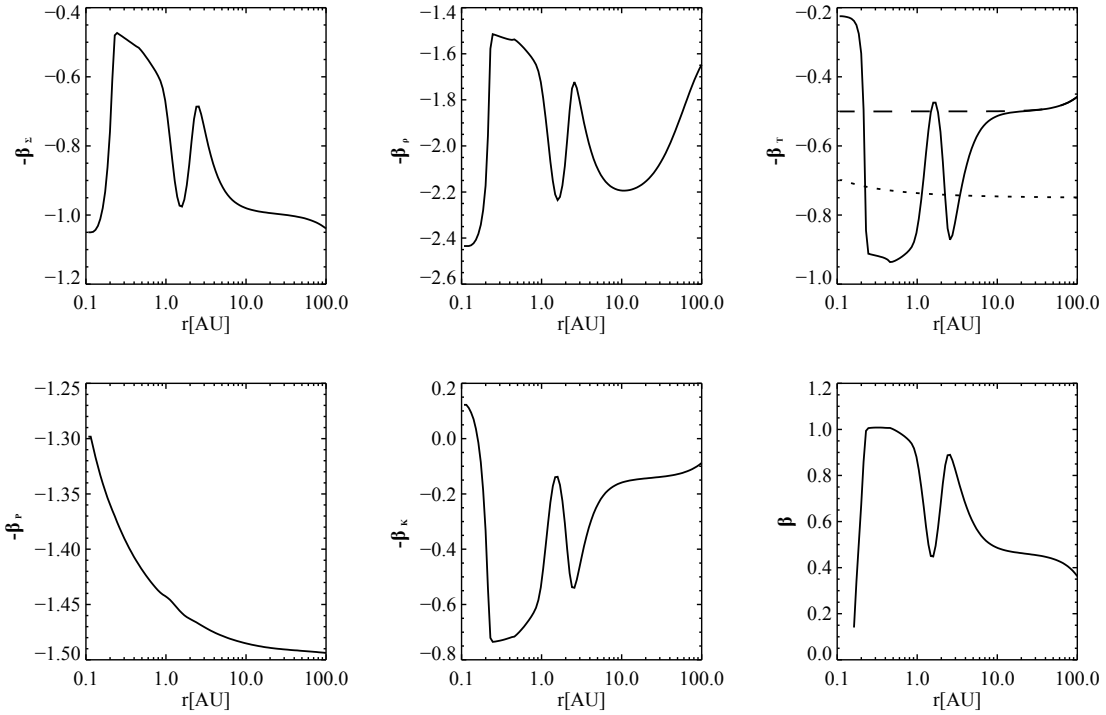

Figure 2.8 Radial gradients in a protoplanetary accretion disk with an accretion rate of $\dot{M} = 3 \times 10^{-9} M_\odot/\mathrm{yr}$, an assumed efficiency of turbulent diffusion of angular momentum of $\alpha = 5 \times 10^{-4}$ around a T-Tauri star with $T_{\mathrm{eff}} = 4300K$ and $R_\star = 2R_\odot$ (model Oph3 in table 2.1).

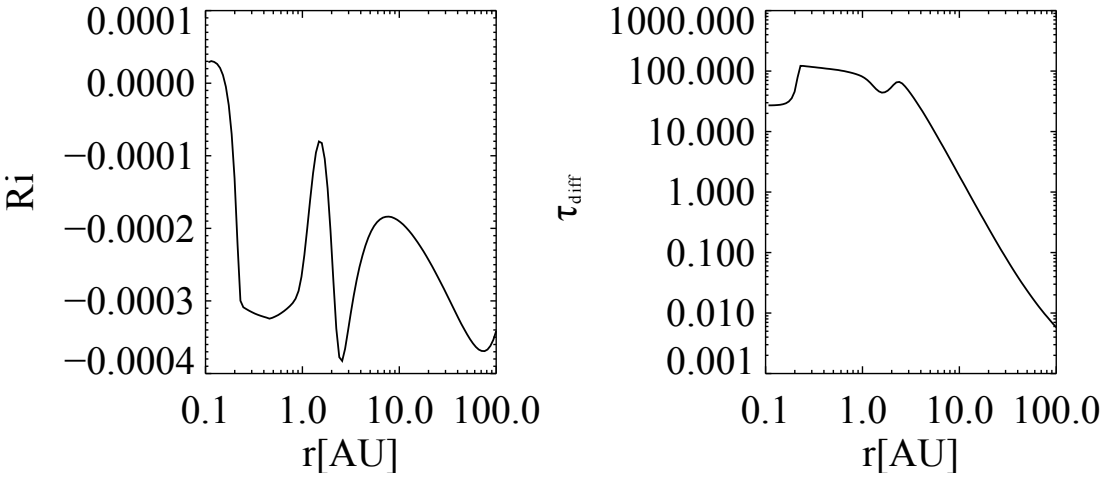

Figure 2.9 Richardson number and thermal diffusivity in a protoplanetary accretion disk with an accretion rate of $\dot{M} = 3 \times 10^{-9} M_\odot/\mathrm{yr}$, an assumed efficiency of turbulent diffusion of angular momentum of $\alpha = 5 \times 10^{-4}$ around a T-Tauri star with $T_{\mathrm{eff}} = 4300K$ and $R_\star = 2R_\odot$ (model Oph3 in table 2.1).

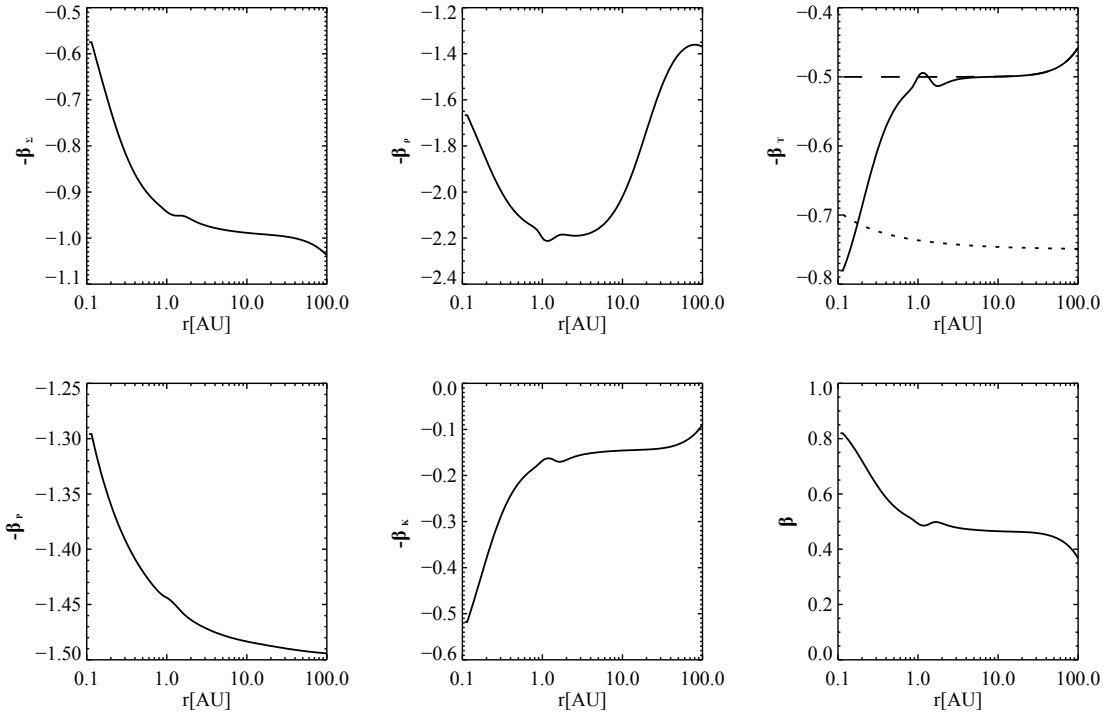

Figure 2.10 Radial gradients in a protoplanetary accretion disk with an accretion rate of $\dot{M} = 3 \times 10^{-10} M_\odot/\mathrm{yr}$, an assumed efficiency of turbulent diffusion of angular momentum of $\alpha = 6 \times 10^{-4}$ around a T-Tauri star with $T_{\mathrm{eff}} = 4300K$ and $R_\star = 2R_\odot$ (model Oph4 in table 2.1).

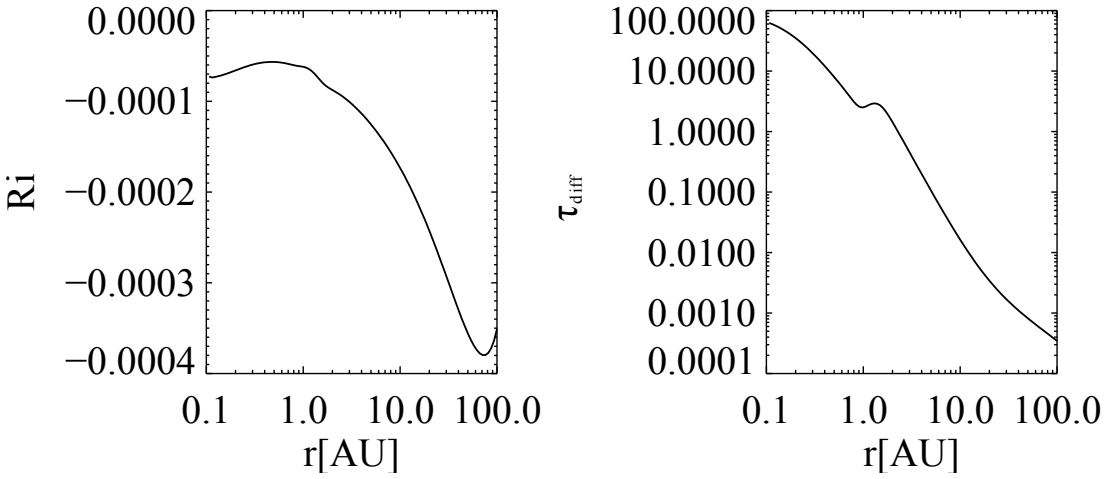

Figure 2.11 Richardson number and thermal diffusivity in a protoplanetary accretion disk with an accretion rate of $\dot{M} = 3 \times 10^{-10} M_\odot/\mathrm{yr}$, an assumed efficiency of turbulent diffusion of angular momentum of $\alpha = 6 \times 10^{-4}$ around a T-Tauri star with $T_{\mathrm{eff}} = 4300K$ and $R_\star = 2R_\odot$ (model Oph4 in table 2.1).

Chapter 3

A Parameter Study for the Baroclinic Disk Instability

3.1 Introduction

As mentioned in the introduction the preferred method to transport angular momentum in a disk, the MRI, needs adequately ionized gas that the magnetic field couples to the gas. Yet, it is unclear that every disk possesses a high enough ionization fraction (Gammie, 1996; Turner and Drake, 2009). Therefore there remains interest in hydrodynamical instabilities. Klahr and Bodenheimer (2003) found a hydrodynamical instability creating anti-cyclonic vortices in 3 dimensional radiation hydrodynamical simulations of baroclinic disks, e.g. with a radial entropy gradient and thus vertical shear, which they assumed to be a kind of baroclinic instability (BI) modified for the Keplerian shear profile. As was shown in the last chapter, observed protoplanetary disks have a non-zero radial entropy gradient $\beta_s = -d\ln s/d\ln r$, where s is the entropy and r the radial distance to the star, and are indeed not barotropic but rather baroclinic, which means that the planes of constant pressure and constant density are misaligned, driving a thermal wind, e.g. vertical shear.

Thermal relaxation turned out to be crucial when Petersen et al. (2007a,b) studied baroclinic vortex amplification using an incompressible approximation. In fact thermal relaxation or heat diffusion is a key ingredient to establishing the baroclinic feedback that keeps vortices growing in baroclinic disks.

While both effects, i.e. the baroclinic instability (BI) and baroclinic vortex amplification (BVA), are a result of the superadiabatic radial stratification of a disk, they are not to be confused. An operating linear baroclinic instability (compare Cabot, 1984; Knobloch and Spruit, 1986) would be able to create vortices in disks from infinitesimal perturbations, whereas the baroclinic vortex amplification deals with the growth of existing vortical perturbations, for

which Lesur and Papaloizou (2010) used the term "subcritical baroclinic instability".

The occurrence of a classical BI in the disk in its geophysical definition is still under debate and shall be discussed elsewhere. There are three possibilities: 1.) there is a classical BI working in protoplanetary disks creating the initial vortices, 2.) there is another instability (see the discussion in Klahr, 2004) for example Kelvin-Helmholz instability creating vortices from vorticity maxima in sheared waves or 3.) small vortical perturbations are triggered from other effects, e.g. waves from the MHD active region of the disks or maybe from the waves emitted by vortices at other radii. In any case the finite amplitude vortices then grow as described by the BVA until they reach a sufficient size to influence the evolution of the disk. This physics is the subject of this chapter.

Recently, Lyra and Klahr (2011) examined the interplay of BVA and MHD. They found that as soon as magnetic fields are coupled to the gas, the MRI takes over and thus supercedes vortices which were previously amplified by BVA. This implies that the BVA is a phenomenon restricted to the MRI deadzone.

All the above mentioned (lower resolution) studies had to apply entropy gradients 2-4 times stronger than expected in protoplanetary disks (see Andrews et al., 2009, and chapter 2) to successfully drive BVA. This chapter, using results from high resolution runs, shall now display that the likely entropy gradients in protoplanetary disks are in fact sufficient for BVA.

Lately, Paardekooper et al. (2010) investigated the effect of radial vortex migration. They discovered that vortices migrate quickly radially inward once a vortex has grown to its full size, which is limited by the scale-height. While this effect will be of major importance in understanding the life-cycle of a vortex, it plays only a minor role for the typically very weak/still growing vortices studied in this thesis. We shall return to vortex migration once we study the BVA in global simulations.

In this chapter we carry out local, fully compressible shearing sheet simulations at various resolutions. We show that as we go to higher resolutions, one can excite the nonlinear instability and achieve Reynolds stresses with the low entropy gradients deduced for observed accretion disks. We conduct an extensive parameter study for entropy gradients β, thermal cooling $\tau_{\rm cool}$ and diffusion times $\tau_{\rm diff}$, and resolution respectively. Section 3.2 gives a brief overview of the physical background of the instability. In section 3.3 we present the numerical setup of our simulations. In section 3.3 we examine the amplification and decay-times of values such as enstrophy $\omega_z^2 \equiv (\boldsymbol{\nabla} \times \boldsymbol{u})_z^2$ and α-stresses. Here,

$$\alpha = \frac{\langle \rho u_x u_y \rangle_{xy}}{q p_0} \tag{3.1}$$

with ρ being the gas density, $\boldsymbol{u}$ the gas velocity and p_0 the initial mean pressure and $q = 1.5$ is the shear parameter for a Keplerian disk. The mean is taken over the x and y domain. We also analyze the saturation values, e.g. how quantities like the entropy gradient, cooling processes in the disk or the size of the simulated domain influence the strength of angular momentum transport. Finally we summarize our results and give a conclusion in section 3.5.

3.2 Physical Background

Vorticity is conserved in barotropic simulations, but in flows with density and pressure treated as independent quantities, vorticity is produced via the so called baroclinic term

$$\boldsymbol{\nabla} \times \left(-\frac{1}{\rho} \boldsymbol{\nabla} p \right) = \frac{1}{\rho^2} \boldsymbol{\nabla} \rho \times \boldsymbol{\nabla} p \propto \beta_s \partial_y \rho.^4 \tag{3.2}$$

Here ρ is the gas density, p the gas pressure, and β_s is the global radial entropy gradient. The ground state of a disk is geostrophic, i.e. all centrifugal forces and gravity are in balance with the strictly radial pressure gradient. If an entropy perturbation is introduced without perturbing the pressure, then this entropy perturbation will efficiently create vorticity in the presence of the global entropy and pressure gradients. This effect is basically radial buoyancy because of superadiabatic radial stratification[5]. Indeed the radial Brunt-Väisälä frequency (Tassoul, 2000)

$$N^2 = -\frac{1}{\gamma \rho} \frac{\partial p}{\partial r} \frac{\partial}{\partial r} \ln \left(\frac{p}{\rho^\gamma} \right) \tag{3.3}$$

is imaginary, which would lead to radial convection. However, shear stabilizes non-axisymmetric modes and for the dynamic stability of the axisymmetric system the Solberg-Høiland criterium (Tassoul, 2000; Rüdiger et al., 2002)

$$\begin{aligned} \frac{1}{r^3} \frac{\partial j^2}{\partial r} - \frac{1}{c_p \rho} \boldsymbol{\nabla} p \boldsymbol{\nabla} s > 0 \\ \frac{\partial p}{\partial z} \left(\frac{\partial j^2}{\partial r} \frac{\partial s}{\partial z} - \frac{\partial j^2}{\partial z} \frac{\partial s}{\partial r} \right) < 0, \end{aligned} \tag{3.4}$$

where j is the specific angular momentum, has to be considered. If one rewrites equation 3.4 in the local approximation (see e.g. Balbus and Hawley,

[4] As our flows are strongly subsonic we consider them incompressible. Otherwise the equation has to be rewritten for potential vorticity

[5] Please note that similar situations can be found in subadiabatic configurations. In fact, in any non-barotropic disk, an entropy perturbation will lead to a vorticity fluctuation. But without the global pressure and entropy gradient pointing in the same direction these perturbations will quickly decay (shear away) as they lack a mechanism for vortex amplification.

1998), the stabilizing action of the specific angular momentum shows up as the value of Oorts constant in the Coriolis term. If the vertical stratification in velocity is also considered, as it must be in real 3 dimensional accretion disks (Fromang et al., 2011), then the combined action of radial buoyancy and Coriolis forces lead to a thermal wind, i.e. a vertical shear in rotational velocity. This is precisely the initial state of the baroclinic instability in rotating stars and planetary atmospheres. Yet, instability in these systems is not obstructed by radial shear, whereas in a Keplerian disk radial scales would have to be on the order of H (Knobloch and Spruit, 1986) to be linearly unstable with respect to baroclinic instability.

Before we explain the motion of a gas parcel in a vortex, we want to explain the cooling and heating processes in an disk as they proved in be crucial to maintaining the baroclinic feedback (Petersen et al., 2007a,b). Dust particles absorb photons, which heats them up. To cool, they radiate in the infrared. This radiation can be reabsorbed by other particles. This happens on a typical length-scale. A convenient parametrization for the diffusion time in our vortex system is $\tau_{\rm diff} = a^2/D$ where a is the radius of the vortex and D the radiative diffusion constant. D can be determined using a flux limited diffusion approach as in Kley et al. (2009). There, $D = \lambda c 4 a_{\rm R} T^3 \left(\rho\kappa\right)^{-1}$ where λ is the flux limiter, c the speed of light, $a_{\rm R}$ the radiation constant, T and ρ the gas temperature and density respectively and κ the opacity. Since D is constant and the vortex grows, $\tau_{\rm diff}$ will increase over time. Thermal relaxation is the other process by which dust can deposit heat into the gas. When a dust particle is not at the local equilibrium temperature, it will exchange heat with the ambient medium on a time-scale $\tau_{\rm cool}$. This time-scale affects vortices of all sizes equally.

The baroclinic feedback is explained in detail by Petersen et al. (2007b). Here, we follow the description of the mechanism by Lesur and Papaloizou (2010). The left panel of figure 3.1 shows the vorticity profile of a baroclinic vortex. Just before position 1, a gas parcel is in thermal equilibrium. As it moves along a streamline to position 1 is becomes slightly warmer than the ambient gas. Due to buoyancy effects it rises (moves to larger radii) to position 2. This track happens adiabatically. As the gas parcel is advected to position 3 it equalizes with its surroundings so that it adopts the background temperature. This heat exchange requires thermal diffusion or relaxation on appropriate time-scales. Once the gas parcel has reached position 3 it is slightly colder than the ambient gas. It will sink towards warmer regions to position 4. From position 4 to 1 thermal equilibration happens again. However, this time the fluid element heats up to the ambient temperature.

Since there is no heat exchange from step 1 to 2 and 3 to 4, an azimuthal temperature, and thus also entropy, gradient is established around the vortex. In a baroclinic flow, entropy is a function of pressure and density: $s\left(p,\rho\right)$. Since

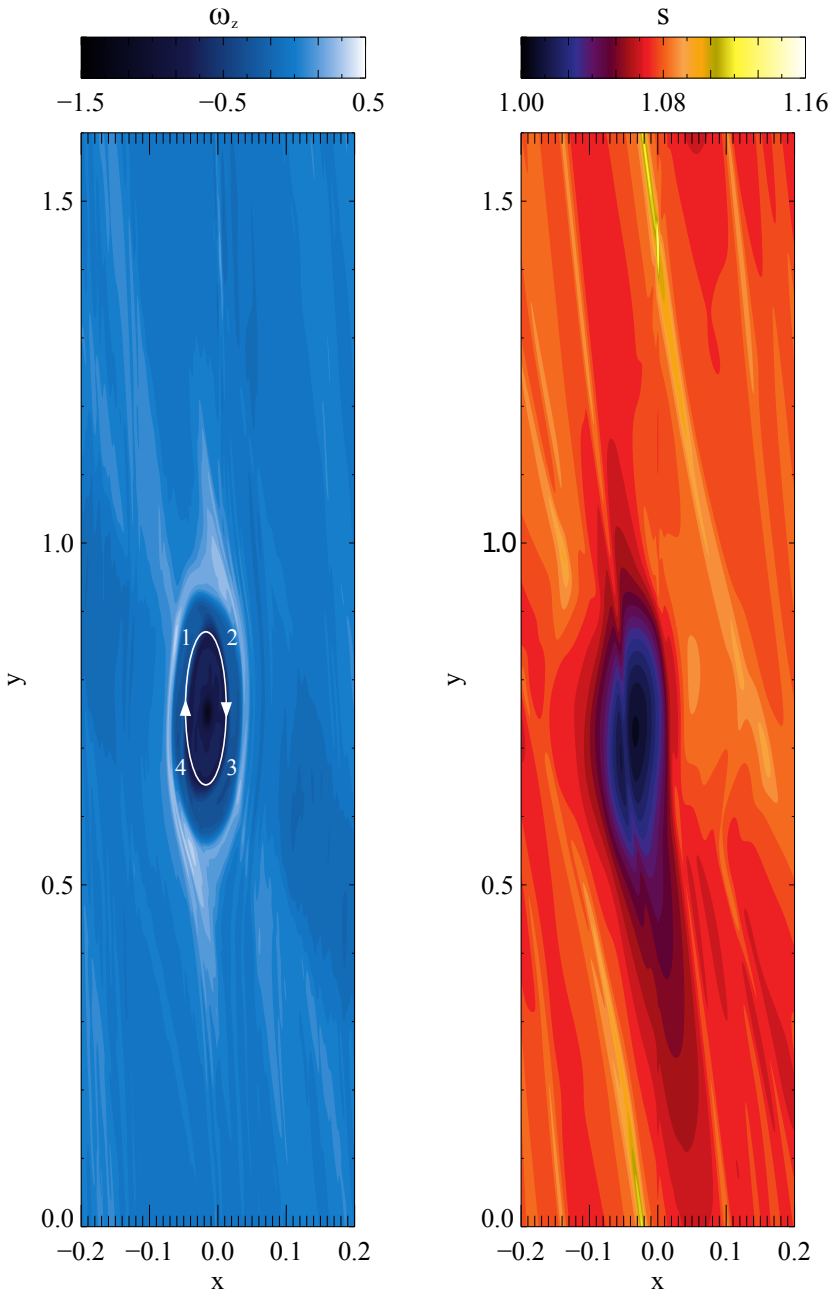

Figure 3.1 This plot shows (left) the vorticity profile ω_z and (right) deviation from the background entropy s for a baroclinic vortex with $\beta = 1.0$ after 700 local orbits (simulation C in table 3.1). The white ellipse shows the anti-cyclonic flow direction. Fluid parcels move along streamlines from 1 to 2 to 3 to 4 and back to 1. Within the vortex the entropy is lower than the background entropy (middle panel).

the pressure variations, especially from weak vortices, are negligible in comparison to the global radial pressure gradient and much smaller than the azimuthal entropy gradient, pressure can approximated as constant (Klahr and Bodenheimer, 2003; Klahr, 2004; Petersen et al., 2007a). This requires an azimuthal density gradient which enforces the baroclinic feedback.

If cooling is too fast (short time-scales) then the fluid parcel adapts the background temperature slope too quickly. The vortex becomes locally isothermal and no entropy transport is possible. Conversely, if cooling is too slow (long time-scales) then gas will not equilibriate fast enough. The vortex gas becomes adiabatic with constant entropy across the vortex. In both extreme cases, isothermal or adiabatic, the azimuthal entropy gradient across the vortex vanishes. As shown in equation (3.2), the vorticity source ceases to amplify the vortex, or at most stabilizes it against losses from numerical viscosity from radiating vorticity perturbations, e.g. Rossby waves. Therefore it is important that the thermal cooling and diffusion times are in the right regime.

We model both thermal relaxation and thermal diffusion separately because, dependent on the vortex size, either one or the other dominates. The process with the shorter time-scale sets the heat exchange between the vortex and ambient gas.

3.3 Numerical Setup

Our simulations were conducted with the PENCIL CODE[5], a finite difference code which uses 3^{rd}-order Runge-Kutta time derivatives according to Williamson (1980) and 6^{th}-order spacial derivatives. We use a 2 dimensional, local shearing sheet approach. This scheme is illustrated in figure 3.2. A sheet (in 3 dimensional simulations, a box) is cut out of the disk in the mid-plane and co-rotates with the co-rotational radius R_0. The spherical coordinate system has to be transformed into a cartesian coordinate system via the ansatz $r = R_0 + x$ and $y = \varphi R_0$. Then the equations are linearized and 2^{nd} order or higher terms are neglected. This restricts us to $x \ll R_0$ and $y \ll R_0$, which means that the extent of the sheet (box) is small compared to the radial location of the box. This is a 2D version of the model used in Lyra and Klahr (2011). To include the baroclinic term, they defined a global entropy gradient β_s. Note that in our approximation the gradients for entropy s and pressure p are the same. Therefore we do not distinguish them in our notation and call both β. However, in real disks both may easily differ.

[5]See http://www.nordita.org/software/pencil-code/

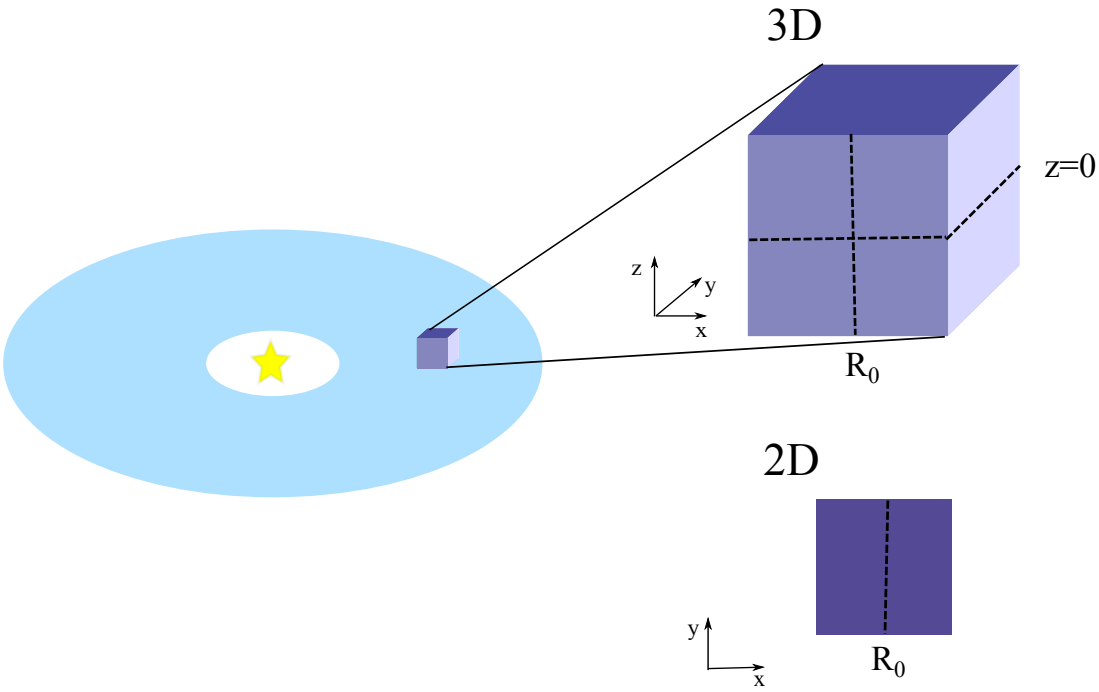

Figure 3.2 Schematic of the shearing sheet/box formalism. A sheet/box is taken out of the disk around the mid-plane at a certain radius R_0. The sheet/box is corotating with R_0.

The total pressure $p_{\rm tot} = \bar{p} + p$ consist of a local fluctuation p and a time-independent part that follows a large scale radial pressure gradient β

$$\bar{p} = p_0 (r/R_0)^{-\beta}, \tag{3.5}$$

where r is the cylindrical radius. The full set of linearized equations used in our simulations are as follows

$$\frac{\mathcal{D}\rho}{\mathcal{D}t} + (\boldsymbol{u}\cdot\boldsymbol{\nabla})\,\rho = -\rho\boldsymbol{\nabla}\cdot\boldsymbol{u} + f_D(\rho) \tag{3.6}$$

$$\begin{aligned}\frac{\mathcal{D}\boldsymbol{u}}{\mathcal{D}t} &+ (\boldsymbol{u}\cdot\boldsymbol{\nabla})\,\boldsymbol{u} = -\frac{1}{\rho}\boldsymbol{\nabla}p - 2\Omega_0\,(\hat{\boldsymbol{z}}\times\boldsymbol{u}) \\ &+ \frac{3}{2}\Omega_0 u_x\hat{\boldsymbol{y}} + \frac{\beta p_0}{R_0}\left(\frac{1}{\rho} - \frac{1}{\rho_0}\right)\hat{\boldsymbol{x}} + f_\nu(\boldsymbol{u},\rho)\end{aligned} \tag{3.7}$$

$$\begin{aligned}\frac{\mathcal{D}s}{\mathcal{D}t} &+ (\boldsymbol{u}\cdot\boldsymbol{\nabla})\,s = \frac{1}{\rho T}\Bigg\{\boldsymbol{\nabla}\cdot(D\boldsymbol{\nabla}T) - \rho c_v\frac{(T-T_0)}{\tau_{\rm cool}} \\ &+ \frac{\beta p_0}{R_0}\frac{u_x}{(\gamma-1)}\Bigg\} + f_K(s).\end{aligned} \tag{3.8}$$

Here, ρ is the gas density, $\boldsymbol{u}$ is the deviation of the gas velocity from the Keplerian value, T the temperature, c_v the specific heat at constant volume, $\tau_{\rm cool}$ is

Table 3.1. Simulation setups and results

run	β_P	$\tau_{\rm cool}$ $(2\pi\Omega_0{}^{-1})$	$\tau_{\rm diff}$ $(2\pi\Omega_0{}^{-1})$	ω_z^2 $(\Omega_0{}^2)$	α	$u_{\rm rms}$ $(c_{\rm s})$	$\rho_{\rm rms}$	x-res (gridcells H^{-1})	x-domain (H)
A0	2.0	10	10	0.055	1.22×10^{-2}	0.32	0.12	72	4
A	2.0	10	10	0.056	1.05×10^{-2}	0.33	0.22	144	4
A2	2.0	10	10	2.15×10^{-2}	3.09×10^{-3}	0.19	0.19	144	8
B	2.0	10	10	0.060	1.21×10^{-2}	0.33	0.22	288	4
C0	1.0	10	10	6.31×10^{-5}	4.16×10^{-5}	0.001	0.002	72	4
C	1.0	10	10	0.051	8.67×10^{-3}	0.31	0.22	144	4
C2	1.0	10	10	4.63×10^{-3}	8.2×10^{4}	0.08	0.06	144	8
D	1.0	10	10	0.059	9.63×10^{-3}	0.31	0.21	288	4
E	1.0	30	10	0.022	4.33×10^{-3}	0.23	0.15	144	4
F	1.0	30	30	0.022	3.72×10^{-3}	0.23	0.15	144	4
G	1.0	100	10	0.017	2.61×10^{-3}	0.14	0.08	144	4
H	1.0	100	30	0.013	2.22×10^{-3}	0.15	0.08	144	4
I	1.0	100	100	0.010	1.36×10^{-3}	0.14	0.08	144	4
J0	0.5	10	10	1.61×10^{-14}	4.22×10^{-5}	0.001	0.002	72	4
J	0.5	10	10	5.25×10^{-3}	6.38×10^{-4}	0.35	0.04	144	4
J2	0.5	10	10	1.77×10^{-3}	8.91×10^{-5}	0.03	0.03	144	8
K	0.5	10	10	4.30×10^{-3}	4.30×10^{-4}	0.57	0.05	288	4
L	0.5	30	10	0.021	3.89×10^{-3}	0.23	0.15	144	4
M	0.5	30	30	0.021	3.01×10^{-3}	0.23	0.15	144	4
N	0.5	100	10	6.00×10^{-3}	1.38×10^{-3}	0.14	0.10	144	4
O	0.5	100	30	6.00×10^{-3}	1.38×10^{-3}	0.14	0.10	144	4
P	0.5	100	100	8.63×10^{-3}	1.18×10^{-3}	0.15	0.10	144	4

the thermal diffusion time scale, and K the heat conductivity. The symbol

$$\frac{\mathcal{D}}{\mathcal{D}t} \equiv \frac{\partial}{\partial t} + u_y^{(0)} \frac{\partial}{\partial y} \tag{3.9}$$

represents the Keplerian derivative where $u_y^{(0)} = -3/2\Omega_0 x$.

For a more thorough derivation of these equations and the linearization of the global pressure gradient we refer to Lyra and Klahr (2011) and the appendix therein.

In order to keep the numerical scheme stable we add sixth-order hyperdiffusion $f_D(\rho)$, hyperviscosity $f_\nu(\boldsymbol{u}, \rho)$, and hyperconductivity $f_K(s)$ (Lyra et al., 2008, 2009; Oishi and Mac Low, 2009).

The radiation processes in the disk are implemented through the first (thermal diffusion as an approximation for flux limited diffusion of radiation energy density) and second (thermal relaxation to mimic heat exchange with the surface of the disk and thermal equilibration through the irradiation from the central object) terms on the right hand side of the entropy equation. As mentioned in the last section we keep the diffusion coefficient D, which is defined as in (Kley et al., 2009), constant in time and space and define its value via $\tau_{\rm diff} = H^2/D$. So if the vortex has a radius of H, the pressure scale-height of the disk, the diffusion time $\tau_{\rm diff}$ has the value quoted in table 3.1.

To clarify that it is indeed the global entropy gradient that produces the vorticity we take the curl of the Navier-Stokes equation (3.7) and assume an equilibrium state, $u_x = 0$, $\partial_y = 0$, and $\boldsymbol{\nabla} P = 0$ so that

$$\frac{\mathcal{D}\omega_z}{\mathcal{D}t} = \frac{\beta p_0}{\rho^2 R_0}\partial_y \rho. \tag{3.10}$$

Here we see that the negative azimuthal density gradient across the vortex is the source for vorticity production proportional to the global entropy gradient.

With the PENCIL CODE we do not see a numerical instability which appear in Zeuss[7] like finite volume codes without explicit viscosity. During tests we conducted we saw that the dissipation that we have to apply to stabilize our code suppresses such a numerical instability and thus does not play a role in our simulations.

Initially we apply a finite perturbation to the density so that

$$\rho\,(x, y) = \rho_0 + \rho' \tag{3.11}$$

with ρ_0 the constant background density and ρ' the actual perturbation of the form

$$\rho' = \rho_0 C e^{-(x/2\sigma)^2} \times \sum_{i=-k_x}^{k_x} \sum_{j=0}^{k_y} \sin\left\{2\pi\left\{i\frac{x}{L_x} + j\frac{y}{L_y} + \phi_{ijk}\right\}\right\}. \tag{3.12}$$

where C describes the strength of the perturbation, L_x and L_z are the length of the physical domain in x and y direction respectively, and ϕ_{ij} is an arbitrary phase between 0 and 1. We perturb the density in a way that $\rho_{\rm rms} = 5\%$ for $\beta = 1.0, 2.0$ (runs A-I) and $\rho_{\rm rms} = 10\%$ for $\beta = 0.5$ (runs J-P) and $k_x = k_y = 10$. The initial state is non-vortical. This is the initial condition used by Lyra & Klahr (2011), the same amplitude C for simulations with $\beta = 2.0$.

Note that with this initial perturbation we do not perturb the pressure but the entropy. Thus it is only the term in Eq. (3.10) that drives the developement of non-laminar flows.

All our simulations are done in dimensionless code-units. We have $R_0 = \Omega_0 = 1$, $\gamma = 1.4$, and $c_s = 0.1$, which means that $H \equiv c_s/\Omega = 0.1$. All time-quantities are given in terms of $2\pi\Omega_0^{-1}$ the local orbital period at the co-rotational radius R_0.

The standard physical domains of our setup are $\pm 2\,H$ in radial and $[0 - 16]\,H$ in azimuthal direction. Later, we also perform simulations with twice the standard physical domain. The resolution varies between 288 and 1152 gridcells for each dimension. Note that the resolution in radial direction is four times as high as in azimuthal direction.

[7] http://www.astro.princeton.edu/ jstone/zeus.html

The individual setups are given in table 3.1. The thermal cooling times and thermal diffusion times are derived from standard disk models as in chapter 2 and in Bell et al. (1997).

3.4 Results

3.4.1 Convergence of Saturation Values

We explored different resolutions in our simulations, 288^2, 576^2 and 1152^2. The unusual non power of 2 resolution comes from our computational platform with 6 core processors. Typically we used up to 24 CPUs totaling 144 cores for our largest grids. We required about 1200 core hours per run for our largest resolutions. The used grid leads to an effective resolution of 72 (288^2), 144 (576^2) and 288 (1152^2) grid-points per scale-height H in radial direction and 18 (288^2), 36 (576^2) and 72 (1152^2) grid-points per H in azimuthal direction. The radial resolution is 4 times higher than the azimuthal resolution. It is always necessary to compromise between resolution and computational time. Lower resolution simulations are computationally less expensive but might not resolve the necessary scales.

We show the time developement of α-stresses (see equation (3.1)) in figure 3.3. The green line shows the resolution of 288^2, black of 576^2 and red 1152^2 for $\beta = 2.0$ (top), $\beta = 1.0$ (middle) and $\beta = 0.5$ (lower panel). In all simulations $\tau_{\rm diff} = \tau_{\rm cool} = 10$ local orbits.

We see that for $\beta = 1.0$ and $\beta = 0.5$ and a resolution of 288^2 the perturbation decays rapidly. Higher resolution is required to increase the Reynolds-number of the system and have less dissipation on the smaller scales and thus excite the instability again. We impose a stronger initial perturbation for $\beta = 0.5$ than for the higher β. The perturbation in entropy results in a perturbation in vorticity. This perturbation grows proportional to β. For small β we have to apply a stronger perturbation to get the same effect on the vorticity. However, we expect that if we go to even higher resolution it is possible to keep the initial density perturbation at $\rho_{\rm rms} = 5\%$ (Petersen et al. 2007).

If we compare the saturation values of runs with different resolution but the same β, we see that, they differ by only 10 % from one another (see table 3.1).

It is important to note that the instability is excited and we measure reasonable α-values of up to 4×10^{-3} in the converged runs for entropy gradients as low as $\beta = 0.5$. In fact, in section 3.4.5 we show that α depends weakly on β as $\alpha \propto \beta^{1/2}$. Figure 3.3 shows that the saturation values of α do not depend

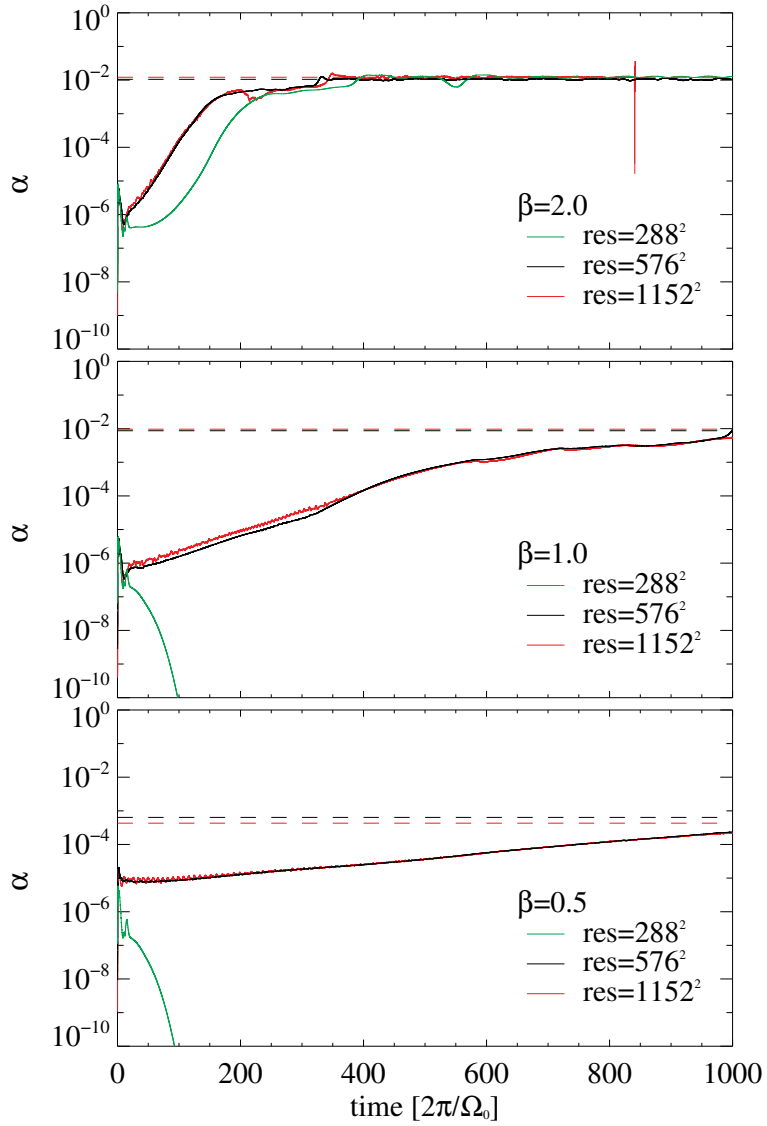

Figure 3.3 Time evolution of α-stresses for the three different resolutions of 288^2 (green), 576^2 (black) and 1152^2 (red) with an entropy gradient of $\beta = 2.0$ (top panel), $\beta = 1.0$ (middle panel) and $\beta = 0.5$ (bottom panel). We have $\tau_{\mathrm{diff}} = \tau_{\mathrm{cool}} = 10 \cdot 2\pi/\Omega_0$. For all resolutions vortex amplification and therefore angular momentum transport can be seen for strong entropy gradients ($\beta = 2.0$). For lower entropy gradients higher resolution is needed to see the development of vortices. The dashed lines show the saturations values ($\beta = 2.0$ and $\beta = 1.0$) and value at the end of the simulation ($\beta = 0.5$) respectively.

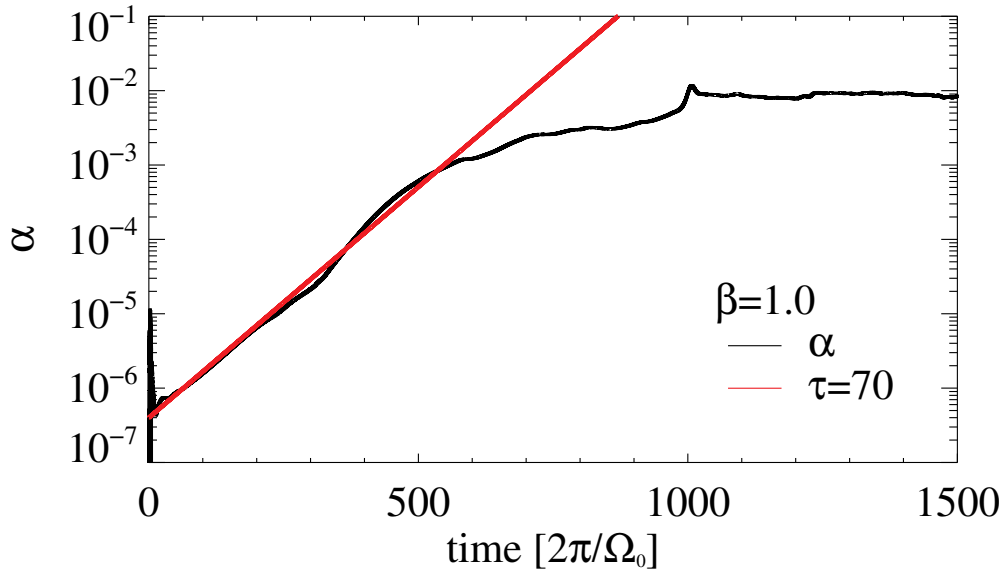

Figure 3.4 Time evolution of α for $\beta = 1.0$ and a resolution of 576^2 (run C). The red slope marks exponential amplification with a amplification-time $\tau = 70\,2\pi/\Omega_0$. For larger entropy gradients (smaller entropy gradients) we find faster (slower) amplification-times.

strongly on β, but as we will see in the next section that the amplification rates do.

3.4.2 Amplification- and Decay Rates

We want to analyze the amplification timescales of the vortices. Here, amplification means how fast a vortex grows due to the baroclinic feedback. Thus it is independent of the initial condition. The initial strong kick needed to get the vortex going decays rather quickly as can be seen in e.g. figure 3.3. There, the α-values start out in the order of 10^{-5} then drop to around 10^{-8} as the initial perturbation decays. As soon as the baroclinic feedback sets in, the values rise again. The timespan that follows is the one in which we measure the amplification time.

Analyzing the amplification-rates of the instability, we find that the initial amplification-rate of the α-stress ($\Gamma(\alpha)$) can be fitted as exponential amplification $\alpha = \alpha_0 \exp(t/\tau)$ with $\tau \approx 70\beta^{-2}$, as seen in figure 3.4 for run C. The proportionality to β^{-2} is not what one would naively expect from a linear convective or buoyancy driven turbulence.

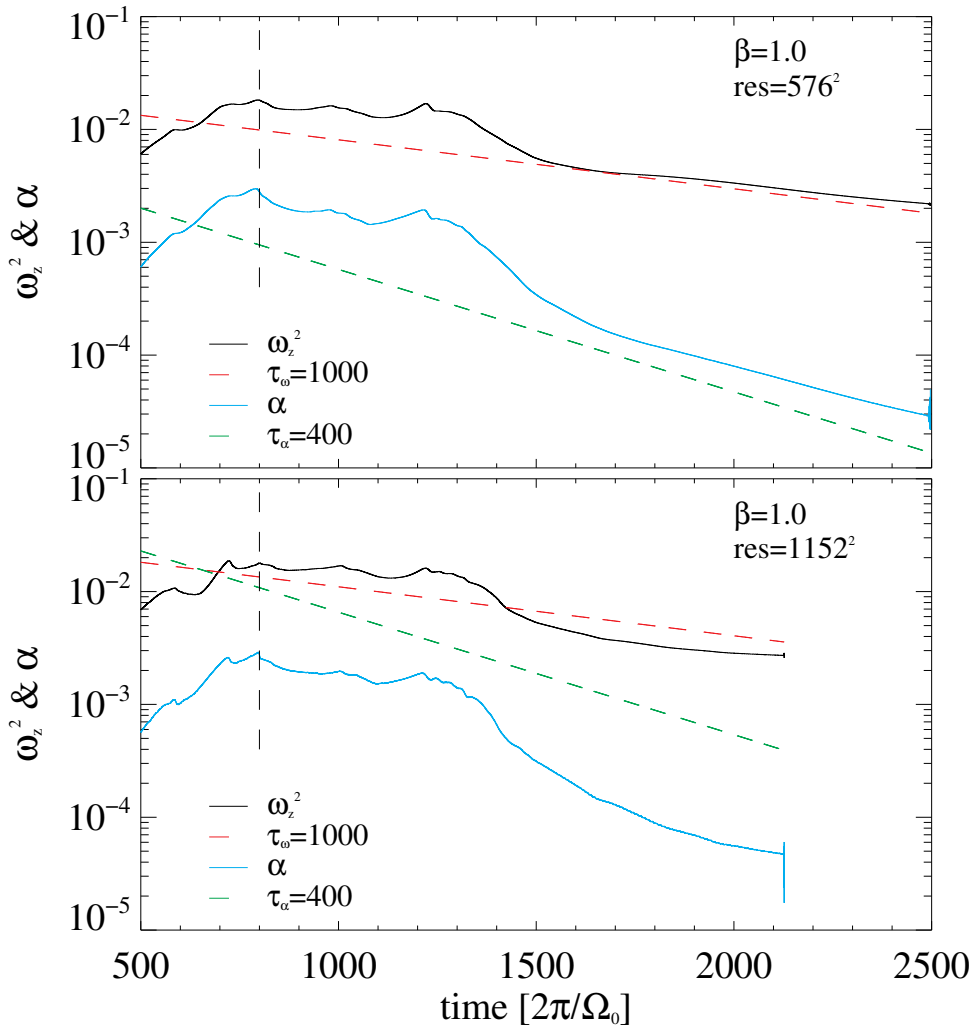

Figure 3.5 In this run with $\beta = 1.0$ a resolution of 576^2 (run C, upper panel) and 1152^2 (run D, lower panel). We turn off the entropy gradient after 800 local orbits (indicated by the black dashed line) to see how the instability decays. Enstrophy is shown with the black line and the α-stresses with the blue line. Our fits are given through the red and green dashed lines respectively. We fit a decay time of $\tau_{\omega_z^2} = 1000$ for the enstrophy and $\tau_\alpha = 400$ for α.

For linear buoyancy driven turbulence one would expect an amplification rate proportional to the Brunt-Väisälä frequency N

$$N^2 = -\frac{1}{\gamma\rho}\frac{\partial p}{\partial r}\frac{\partial}{\partial r}\ln\left(\frac{p}{\rho^\gamma}\right), \tag{3.13}$$

which in our parameters is

$$N^2 = -\beta_p \beta_s \frac{1}{\gamma} \left(\frac{H}{R}\right)^2 \Omega^2 \propto -\beta^2. \tag{3.14}$$

Here we explicitly wrote β_p and β_s to make clear that the Brunt-Väisälä frequency depends on the product of entropy and pressure gradient which can be different in global simulations.

All quantities in equation (3.14) are positive. Thus the Brunt-Väisälä frequency is imaginary and therefore a linear buoyancy driven turbulence would have a amplification-rate $\Gamma \propto iN \propto \beta$. However, we found that $\Gamma \propto \beta^2$ provides a better fit. This reflects the non-linearity of the baroclinic disk instability. In linear convective instability a displaced parcel of gas feels a buoyancy force and thus accelerates propotionally to β. But in the disk baroclinic instability a vortex has to form with an azimuthal entropy gradient proportional to β (and $\tau_{\rm cool}$) before it feels a baroclinic torque proportional to β. Therefore the amplification is proportional to β^2.

The amplification behavior in figure 3.3 already displays convergence for 576 grid cells resolution, e.g. $144/H$ in the radial direction.

If we compare our amplification timescales for the lowest entropy gradients with the migration times obtained by Paardekooper et al. (2010) we see that they are of the same order of magnitude. This means that the vortex could have drifted into the central star before reaching strong α-values. However, Paardekooper et al. (2010) also say that their timescales refer to fully grown vortices of size H. Smaller vortices drift significantly more slowly. This gives our vortices time to grow large enough to generate significant angular momentum transport before drifting into the star.

To study the numerical dissipation effects further we investigate how the vortices decay when baroclinic driving is switched off (figure 3.5). To do this we first evolve runs C and D with $\beta = 1.0$ and the two resolutions of 576^2 and 1152^2 for 800 orbits and then turn off the entropy gradient by setting $\beta = 0.0$. We see vortices shrink and all relevant quantities like enstrophy, ω_z^2 or α-stresses decaying exponentially. Godon and Livio (1999) saw the same exponential decay of vorticity when they analyzed the longevity of anti-cyclonic vortices in protoplanetary disks. Their dissipation was proportional to the effective viscosity applied in their numerical experiment. Here we find the same decay-rate for both resolutions, highlighting that the decay of vortices is no longer through numerical effects, but due to the radiation of waves as in Korotaev (1997).

3.4.3 Saturation Values

In section 3.4.1 we established that even shallow entropy gradients lead to vortices, but we still have to show that sufficient angular momentum transport can be reached with these shallow gradients that are expected in protoplanetary accretion disks. The saturation values of enstrophy ω_z^2 and $u_{\rm rms}$ are of interest as well. In the next sections we discuss the measured saturation values and analyze how the different controlling parameters influence amplification-phase and final values.

Influence of the Entropy Gradient

In figure 3.6 we compare runs A, C and J (at a resolution of 576^2 and with $\tau_{\rm diff} = \tau_{\rm cool} = 10$), which differ only through β. There is an initial exponential amplification-phase of α, $E_{\rm kin}$ and ω_z^2 that is shorter for higher β, followed by a saturated state. We also see that for lower β the saturation values are lower. We want to stress that we did not reach saturation for simulations J and K (at a resolution of 576^2 and 1152^2 and $\tau_{\rm diff} = \tau_{\rm cool} = 10$). Even after 3000 local orbits vortex amplification was still ongoing. Here the $\tau_{\rm diff} = 10$ is much shorter than the amplification-rate we estimated in the previous section ($\tau \approx 300$). As we will see in the next section, the amplification-phase is shortest when those time-scales are comparable because $\tau_{\rm diff}$ also defines how fast pressure perturbations are damped. Although we expect the final saturation values of simulations J and K to be higher than those reached, it is possible that they will still stay below the saturation values obtained in simulations with $\beta = 2.0$.

The vorticity can be seen as a measure of the strength of the vortex. The higher the absolute value of the vorticity the stronger the vortex. Baroclinic vortices are anti-cyclonic vortices and therefore the vorticity has negative values. So the minimum value of vorticity, ($\omega_{z,\rm min}$) shows how strong a vortex is. To explain the behavior of $\omega_{z,\rm min}$ (3rd panel in Fig. 3.6), cooling processes have to be taken into account. During the early phases, thermal transport is dominated by diffusion (Petersen et al., 2007b). As mentioned before this time-scale is shorter for smaller vortices. Therefore heat-exchange between the vortex gas and the ambient gas is more efficient than in later stages. Once the vortex has grown to its final size, thermal relaxation takes over. However heat-exchange in the center of the vortex is less efficient than in the earlier stages. The baroclinic feedback, e.g. the azimuthal entropy gradient across the vortex, is less efficient, the vortex grows weaker, and $\mid \omega_{z,\rm min} \mid$ falls again, creating a flat (as far as the vorticity profile is concerned) yet extended vortex.

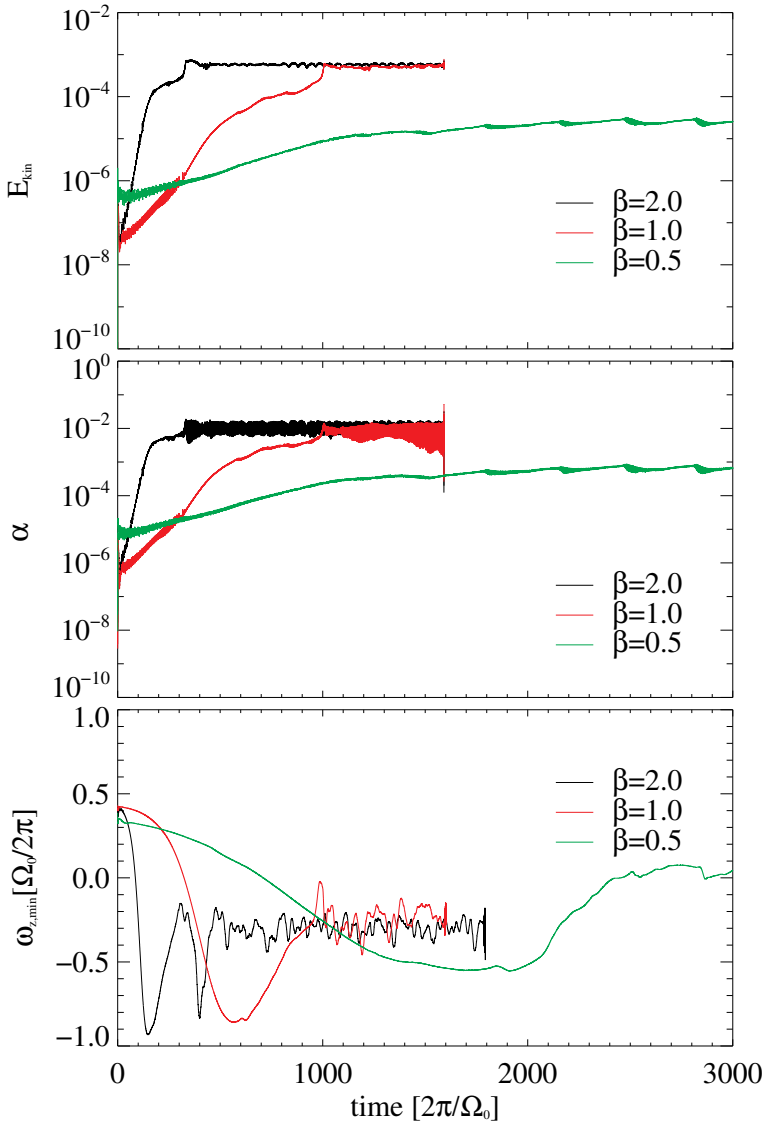

Figure 3.6 Time evolution of kinetic energy E_{kin} (top), α-value (middle) and minimum vorticity $\omega_{z,\min}$ (bottom) for a resolution of 576^2 and $\tau_{\text{diff}} = \tau_{\text{cool}} = 10$, but different entropy gradients: $\beta = 2.0$ (green), $\beta = 1.0$ (black) and $\beta = 0.5$ (red) (runs A, C, J). Saturation is first reached for high β after 300 orbits, then for $\beta = 1.0$. For $\beta = 0.5$, no saturation is reached even after 3000 orbits. The decrease in $\mid \omega_{z,\min} \mid$ after saturation can be explained through the heat transport across the vortex. Since the vortex has reached its final, largest size, heat transport takes longer due to the larger size of the vortex.

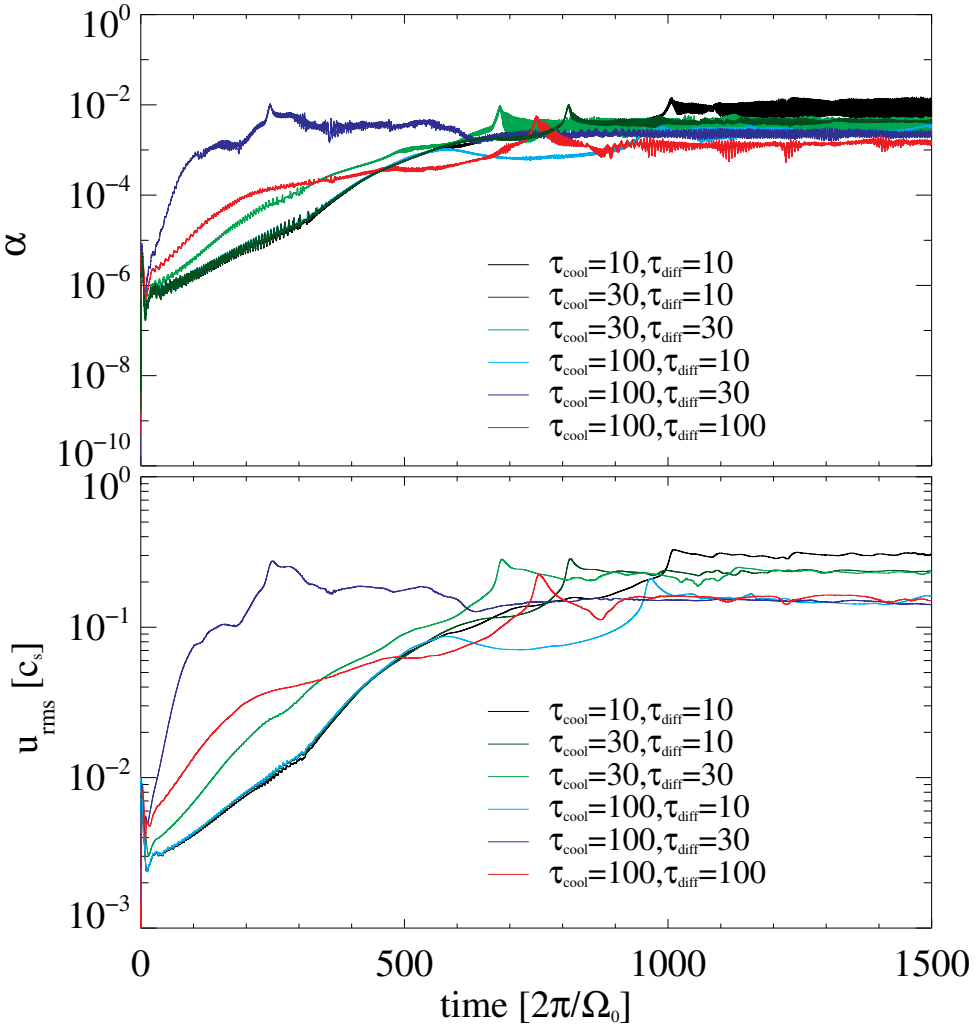

Figure 3.7 Comparison of different $\tau_{\rm diff}$ (right numbers) and $\tau_{\rm cool}$ (left numbers) for same $\beta = 1.0$ (Runs C-I). The top panel shows the α-value and the bottom one $u_{\rm rms}$. One can see that the early amplification-phase is determined by the diffusion time since the heating across the vortex is more important then vertical heat transport. We find faster amplification for higher $\tau_{\rm diff}$. Once the vortex grows larger heat transport gets more difficult and the thermal relaxation dominates. Therefore the saturation values are determined through $\tau_{\rm cool}$. Saturation values are higher for smaller $\tau_{\rm cool}$.

Influence of Thermal Diffusion and Cooling Times

We examine simulations with $\beta = 1$ and different combinations of $\tau_{\rm diff}$ and $\tau_{\rm cool}$ to see how thermal diffusion and relaxation influence the saturation values and the amplification-phases. As long as $\tau_{{\rm diff}(a)} = a^2/K < \tau_{\rm cool}$, $\tau_{{\rm diff}(a)}$ will

dominate the heat exchange from the inside of the vortex to the ambient disk. As the vortex grows, $\tau_{\mathrm{diff}(a)}$ will increase and eventually only contributing to the heat exchange at the outskirts of the vortex. τ_{cool} will then dominate the interior of the vortex.

For the simulations where we set $\tau_{\mathrm{diff}} = \tau_{\mathrm{cool}}$, τ_{cool} will take over when the vortex grows past the size $a = H$. This is fulfilled by the time the vortex has grown to its final size which is limited by H.

This is consistent with what we see in figure 3.7. During the early amplification-phase, simulations with equal τ_{diff} behave exactly the same. Eventually τ_{cool} takes over so that the saturation values are determined by τ_{cool}. For longer τ_{cool}, saturation values are lower than for shorter τ_{cool}.

Influence of the Physical Domain

A problem with local shearing sheet simulations is that eventually vortices grow to the box-size. We cannot say whether they have reached their final size or just do not have any more room to grow. Another problem that arises with the periodic boundary conditions is that the vortices potentially interact with themselves and thus forcing (shaking) them to shed more waves and therefore increase the α-values. To deal with that, we re-did simulations A, C and J with a doubled physical domain (simulations A2, C2, J2 in Table 3.1). The resolution is the same. Instead of $x = [-0.2, 0.2]$ and $y = [0.0, 1.6]$ we switch to $x = [-0.4, 0.4]$ and $y = [0.0, 3.2]$. We did not adjust the initial perturbation in any way. Therefore the initial state is perturbed at smaller wave numbers than in the smaller domain. If we go to even larger boxes the initial condition has to be adjusted so the the effective perturbation in the density is of the same strength as in the smaller physical domain.

If we compare the time development of runs with a different physical domain (see figures 3.8 and 3.9), we see that vortices in fact do not merge as fast in the large domain because there now is more space between them in radial direction, and they pass each other other less frequently due to the extended azimuthal domain. Eventually they will merge as Godon and Livio (1999) saw, but the larger the box, the longer it takes. The precise mechanism of vortex merging is beyond the scope of this work. It has been studied extensively in the field of fluid dynamics (see e.g. Cerretelli and Williamson, 2003). The details of merging are not important for our study, only that it exists.

An unphysical process that can occur in local periodic simulations is that when the vortex approaches the box scale it interacts with itself: the outer edges of the one side of the vortex almost touches the other side of the same vortex. We do not see this for the runs with the larger physical domain. Since the vortices in the larger domain do not interact with themselves, the satura-

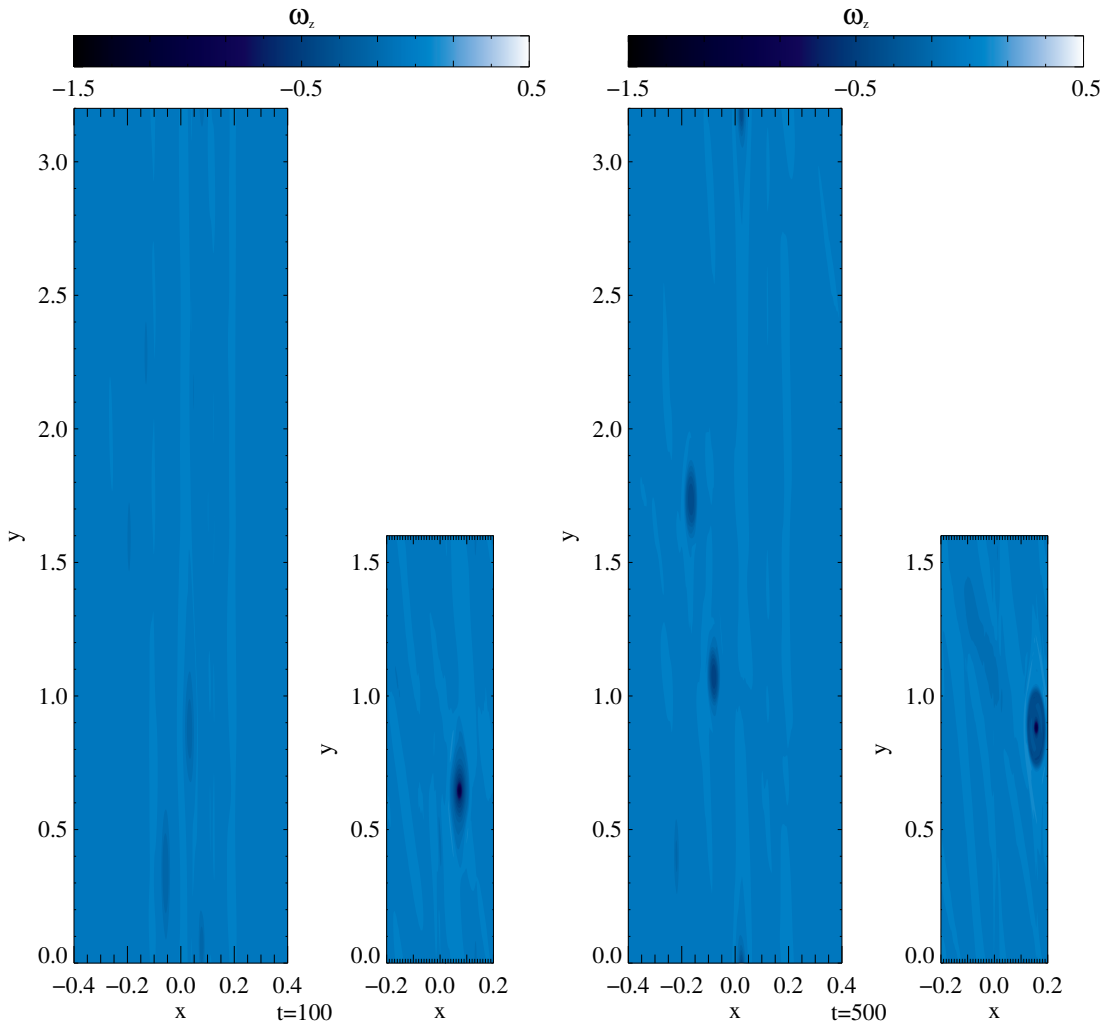

Figure 3.8 Snapshots of the z-component of the vorticity, ω_z, after 100 and 500 local orbits for the two different physical domains with $\beta = 0.5$. Initially both runs have vortices of equal size. Since there is less space between vortices, they can merge sooner in runs with the small physical domain. The vortices in the large physical domain take longer to grow.

tion values are lower. However, they are still in the same order of magnitude (see table 3.1).

In figures 3.8 and 3.9 we show snapshots of the vorticity for $\beta = 0.5$ (simulations J and J2). Initially there are several vortices. The larger ones sweep up the smaller vortices and thus grow further. At 1500 local orbits there is only one vortex left for the small physical domain, whereas in the larger physical domain there are still three vortices.

If we look at the α-value and enstrophy for these two simulations (see figure 3.10), we see that the value seems to decay in the larger box at the end of

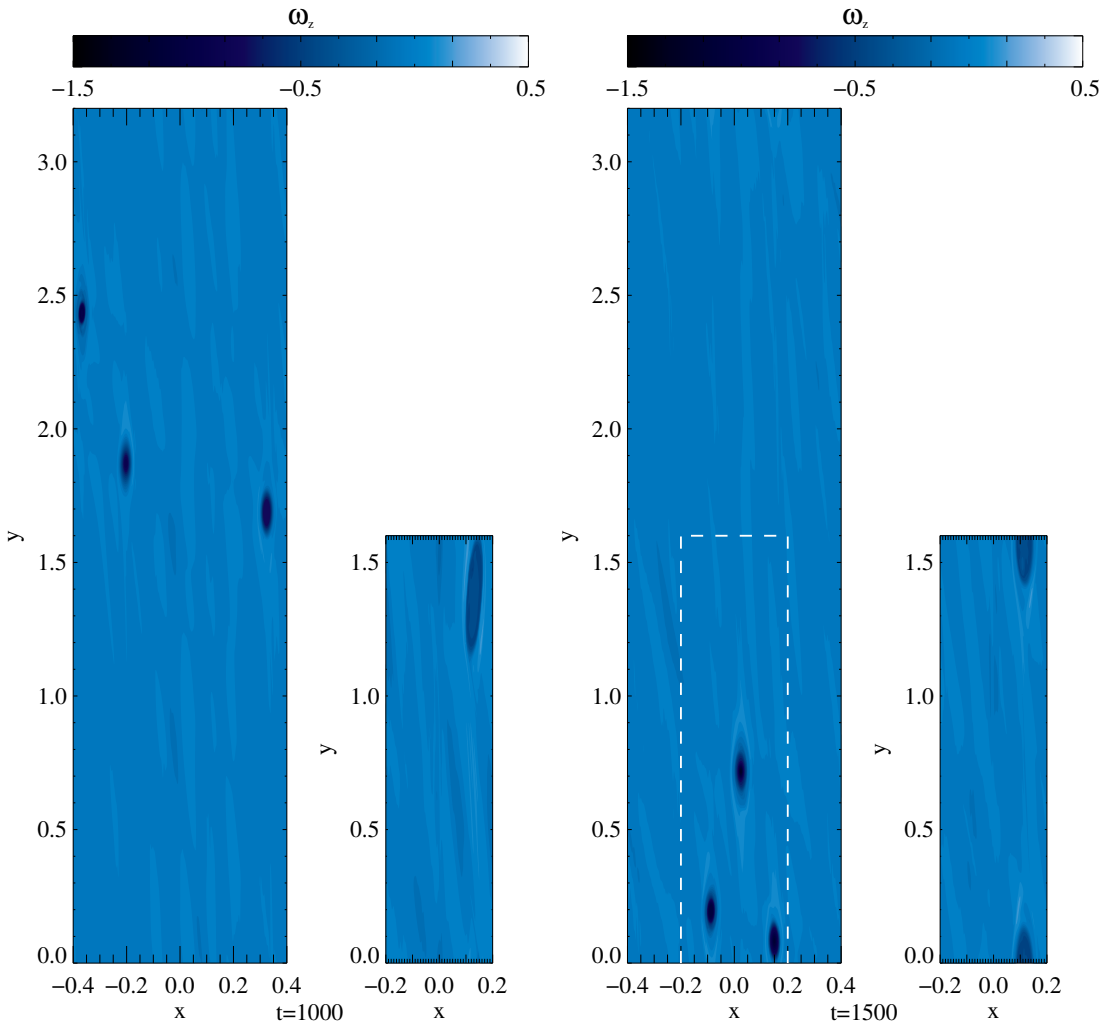

Figure 3.9 Snapshots of the z-component of the vorticity, ω_z, after 1000 and 1500 local orbits for the two different physical domains with $\beta = 0.5$. Initially both runs have vortices of equal size. Since there is less space between vortices, they can merge sooner in runs with the small physical domain. The vortices in the large physical domain take longer to grow.

the run. However this does not mean that the vortices die out. Instead it reflects fluctuations in the vortex interaction, modulating α, as also can be seen in the small domain case at high frequency. We calculate the values as a mean over the entire box but the angular momentum transport is a very localized process as can be seen in figure 3.11 (this time for $\beta = 1.0$ after 1000 orbits). Here we show the product $u_x u_y$ at each location in the box. Most areas of the box have an $u_x u_y$-value close to zero. However, one can clearly see bands excited by the vortex with positive $u_x u_y$-values. It is these bands that lead to angular momentum transport (Klahr and Bodenheimer, 2003). If we had an ideal vortex with a smooth surface we would expect that $u_x u_y$ sums up to zero

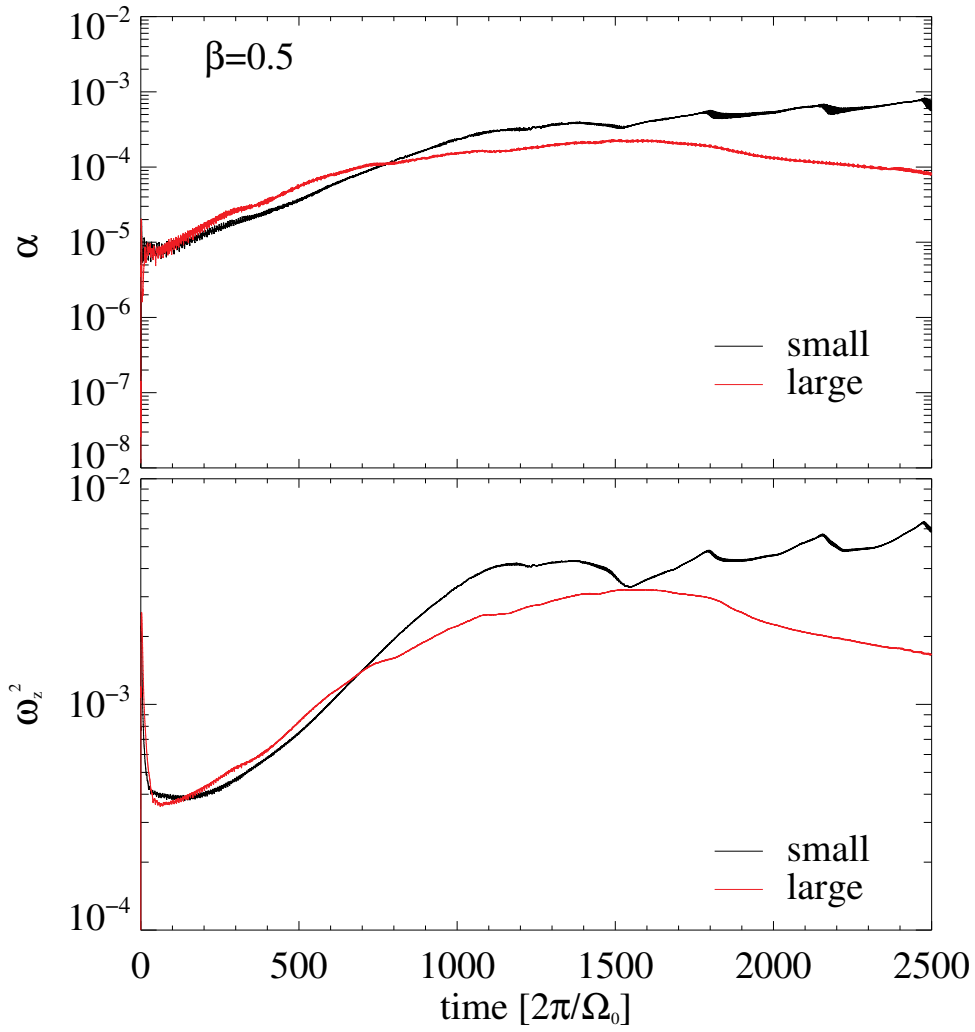

Figure 3.10 Time development of α and ω_z^2 with $\beta = 0.5$ for small (black) and large (red) physical domain (runs J and J2). Saturation values are lower in the large box than in the smaller box.

within the vortex. However the vortex has a more complex structure as can be seen in the lower right plot of figure 3.11. This leads to an negative net α-value across the vortex.

To properly compare the values of α for both physical domains, a box average has to be taken. If the average is taken over an equal physical size centered around a vortex is taken, as indicated by the white dashed lines in figure 3.9, then the α values agree again. The α values are generated only in the vicinity of vortices.

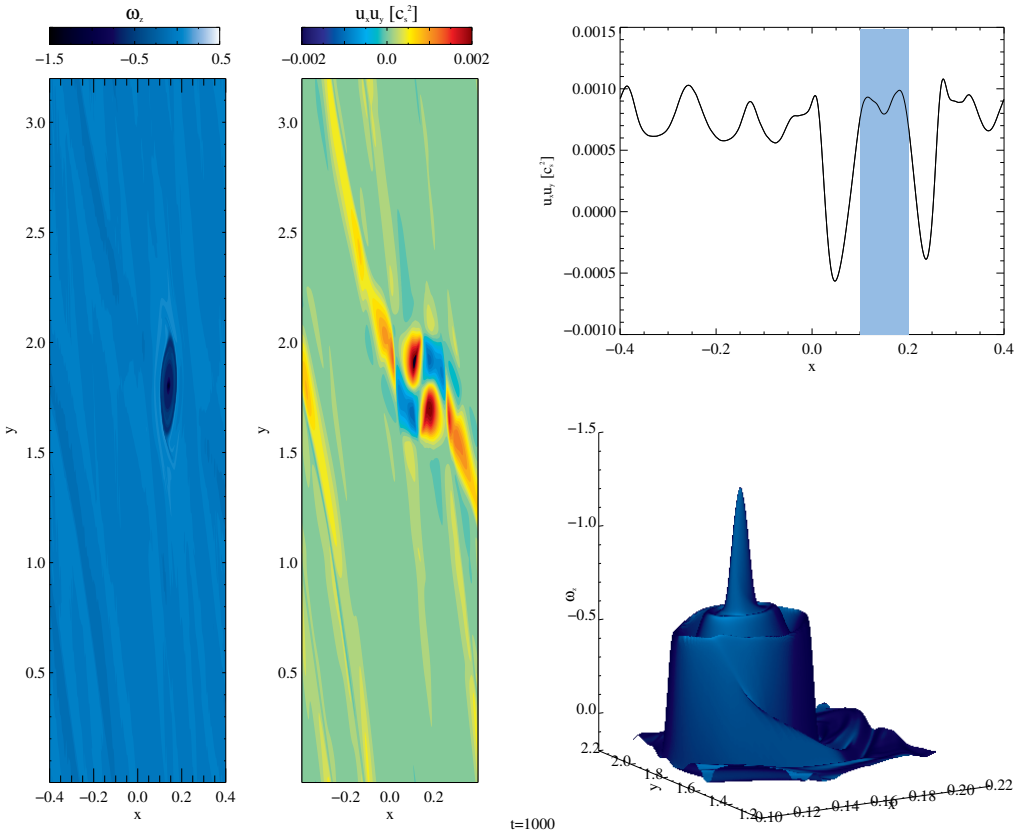

Figure 3.11 Vorticity profile (left) and α-stress (middle) for $\beta = 1.0$ and the large physical domain (run C2). Yellow and red areas denote positive α-vaues whereas blue areas show negative α-stresses. In green areas $\alpha = 0$. One can see the waves excited by the vortex. Those waves are responsible for the angular momentum transport. It is a localized process. Since the vortex and the vorticity-waves fill out a smaller area of the box in the large box (large green areas where there is no angular momentum transport) and our calculation of the saturation values averages over the entire area of the box, the saturation values seem to be lower. The plot in the right upper panel shows an azimuthal average over the $u_x u_y$. Inside an ideal vortex, α-stresses would sum up to zero. However, as indicated in the lower right plot, the vortex has a complex structure which leads to deviations from the idealized shape.

3.4.4 Correlations

A feature of baroclinic instability is that the saturation values of u_{rms}, ω_z^2, ρ_{rms} correlate with each other. Figure 3.12 shows the dependencies of these on α for all our simulations. The colors represent the different entropy gradients: $\beta = 2.0$ (black), $\beta = 1.0$ (red) and $\beta = 0.5$ (green). The different combinations of diffusion and cooling times are represented through the different symbols.

We find that the following relations are good fits to our simulation results

$$u_{\rm rms} = 3\sqrt{\alpha}c_s \quad (3.15)$$
$$\rho_{\rm rms} = 2\sqrt{\alpha}\rho_0 \quad (3.16)$$
$$\omega_z^2 = 5\alpha\Omega_0^2. \quad (3.17)$$

We can derive the typical length-scale of angular momentum transport L, of the system if equation (3.15) is inserted into the general α formalisms (Shakura and Sunyaev, 1973) $\nu = \alpha c_s H = u_{\rm rms} L$ so that

$$L = \frac{\sqrt{\alpha}H}{3}, \quad (3.18)$$

indicating smaller structures than the vortices in our simulations and also smaller than the vorticity in standard α-models where $\omega \propto \sqrt{\alpha}$ with a different coefficient (Cuzzi et al., 1994).

We do not perform a more exact analysis of these dependencies (varying initial conditions) before we do 3 dimensional vertically stratified simulations.

3.4.5 Dependence on β

In section 3.4.2 we have shown that amplification of vortices for low entropy gradients is computationally demanding in terms of evolution time. Thus it is difficult to extract saturation values for entropy gradients even shallower than $\beta = 0.5$ with the computational resources at hand.

In figure 3.13 we plot the α-stresses as a function of the entropy gradient. Note that we choose a different color-coding than in figure 3.12. Here symbols represent the thermal cooling times whereas colors represent thermal diffusion times. The dashed black lines illustrates slopes $\propto \beta^{1/2}$ which is a reasonable fit for the set of points with $\tau_{\rm cool} = 30, \tau_{\rm diff} = 10$ (black triangles) and $\tau_{\rm cool} = 100, \tau_{\rm diff} = 30$ (orange x). We cannot predict α-values for specific entropy gradients and thermal cooling and relaxation times.

The key issue is less a strong correlation between α and β but rather the lack thereof. The strength of the α-stresses reflects the size and the amplitude of the largest vortex. Its size is defined by H only and not by any of the other τ and β parameters. As long as $\tau_{\rm diff}/\tau_{\rm cool}$ and β are sufficient to replenish vorticity at the loss-rate, the α-stresses should be independent of $\tau_{\rm diff}/\tau_{\rm cool}$ and β. The loss time-scale via generation of waves and Reynolds stresses is rather long, see section 3.4.2 and figure 3.5. Thus as long as the amplification-rates are faster than decay-rates, one should always obtain roughly the same α values.

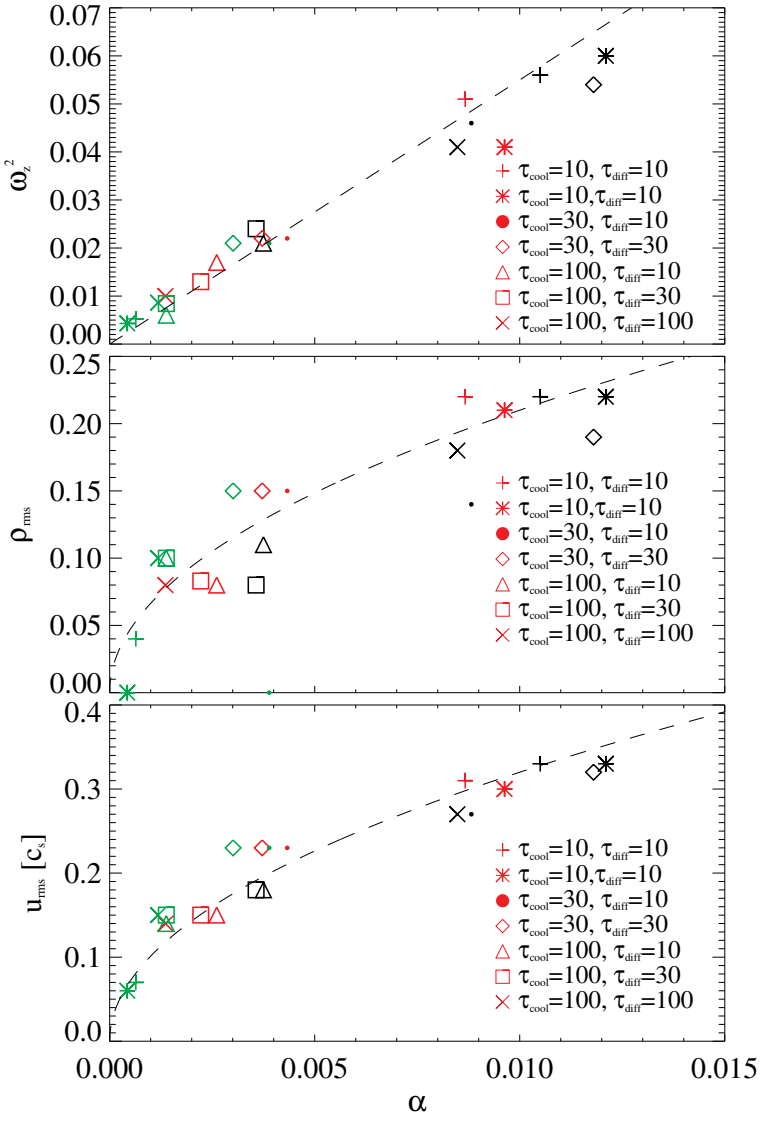

Figure 3.12 Saturation values of ω_z^2, $\rho_{\rm rms}$ and $u_{\rm rms}$ as a function of saturated (value at the end of the simulation for $\beta = 0.5$) α-value for all our runs with the small physical domain (runs A-P). The symbols show the different combinations of $\tau_{\rm cool}$ (left numbers) and $\tau_{\rm diff}$ (right numbers). Here red are runs with $\beta = 1.0$, black $\beta = 2.0$ and green $\beta = 0.5$. The black dashed lines shows our fit.

3.5 Summary and Conclusion

In this chapter we have conducted an extensive parameter analysis for the baroclinic vortex amplification. In particular, we analyzed the global entropy

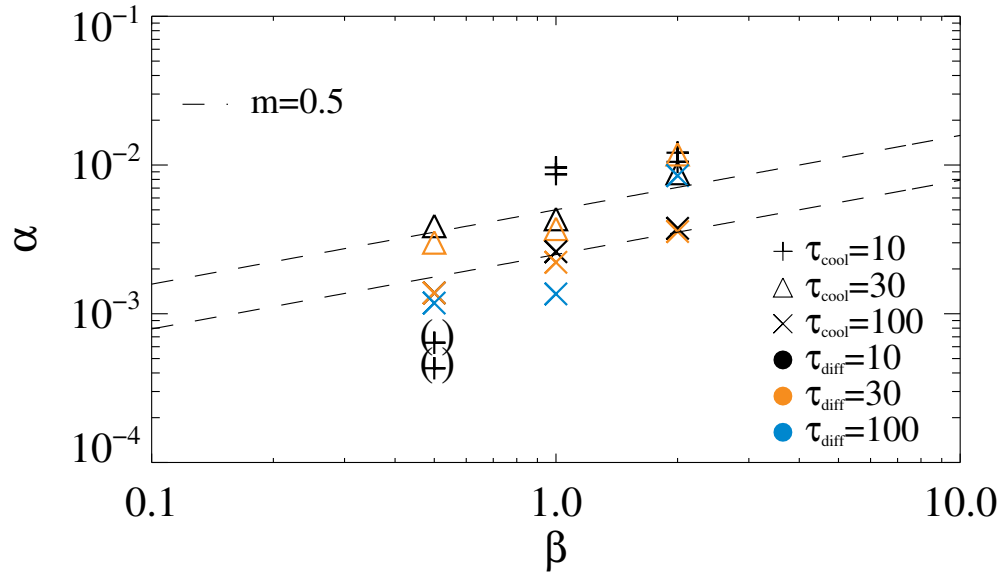

Figure 3.13 Saturation values of α for all our runs with the smaller box depending on β. Runs with parentheses around them were not saturated at the end of the simulations. Therefore we do not take them into account when we fit the $\alpha - \beta$-relation.The symbols show the different combinations of $\tau_{\rm cool}$ (left numbers) and $\tau_{\rm diff}$ (right numbers). Orange are runs with $\beta = 1.0$, black $\beta = 2.0$ and green $\beta = 0.5$. The dashed line has a slope $m = 1/2$.

gradient, thermal relaxation and cooling, as well as numerical parameters such as resolution, and box size influence the amplification-rates for vortices and saturation values of α.

The most important result of our study is that even for entropy gradients as low as $\beta = 0.5$ there is vortex growth. However, the amplification rate is of the order of several 100s of local orbits, which makes it difficult to extract reliable saturation values for the strength of the angular momentum transport.

Recently, Paardekooper et al. (2010) studied the migration behavior of vortices in global accretion disks. They found significant radial drift for fully grown vortices with drift times shorter than the vortex amplification times we measured in this chapter. Nevertheless, this is not a contradiction, because as also shown in Paardekooper et al. (2010), drift rates strongly depend on vortex size. Thus the typical life cycle of a growing vortex would be starting as a small but growing vortex without relevant radial drift, which starts drifting as soon as it reaches its saturated state. Therefore radial drift need not affect the study of of vortex amplification discussed here. Nevertheless, future work will have to investigate radial drift of growing vortices in global simulations.

Note here that Paardekooper et al. (2010) studied the migration in barotropic disks, in which no vortex amplification occurs.

The amplification-phase of the vortices can be measured in terms of the strength of the overall velocity fluctuation, which seem to grow exponential on a certain time-scale $\tau \propto \beta^{-2}$. Therefore amplification is faster for steeper entropy gradients, e.g. $\tau = 16$ for $\beta = 2.0$ and $\tau = 70$ for $\beta = 1.0$. With these short amplification-times we do reach saturation. Whereas the $\beta = 0.5$ simulation was still growing at the final time of 3000 orbital periods, when we stopped the simulation.

Other parameters that influence the evolution of α-stresses are the thermal cooling and relaxation times. The diffusion times define the amplification phase of the vortices because diffusion dominates small scales, i.e. small vortices. We see faster amplification for longer diffusion times. Cooling time on the other hand determines the saturation values. Here, longer time-scales produce lower saturation values.

We find α-values up to 10^{-2} for $\beta = 2.0$ and 10^{-3} for $\beta = 1.0$ and $\beta = 0.5$. These values are not so different from the values found with MRI in active layers (Flock et al., 2011), and stronger than the 10^{-4} found in dead zones (Dzyurkevich et al., 2010), which shows that entropy gradients can be an important mechanism for transporting angular momentum in a dead-zone. Realistic entropy gradients in protoplanetary disks are around $\beta = 0.5$ and $\beta = 1.0$ which can be derived out of the data obtained by Andrews et al. (2009) as discussed in Klahr (2012 submitted to ApJ). Although we could not reach saturation in all our simulations for these entropy gradients, we do see reasonable α-stresses of the order of 10^{-3} to 10^{-2}. We expect the final values to be in this range which provides sufficient angular momentum transport in a disk to achieve observed mass accretion rates. Also, the saturation value of α only depends weakly on β like $\alpha \propto \beta^{1/2}$

Since local simulations are always limited by the box size we also conduct simulations in larger boxes. We do not see a difference in the initial amplification-phase. At later stages the amplification last longer for larger boxes and also is slower. Since part of the vortex evolution happens through merging of smaller vortices, growth takes longer in larger boxes simply because the radial distance between vortices is bigger and thus mergers are less frequent.

The saturation values of velocity fluctuations reached for the larger box sizes are slightly lower than for the smaller box sizes. This is due to two reasons. One is that we see some artificial enhancement in vortex strength in the smaller box. Once the vortex has reached box-size it can no longer grow. It is forced to interact with itself thus emitting more waves. This does not happen in larger boxes.

The other reason is that the number of vortices per radial distance is independent of box size because their typical maximum size is in the order of a pressure scale-height. In the azimuthal direction, the number of vortices is limited to 1 per radius, because otherwise merging will occur on short timescales. Therefore the overall density of vortices per simulation volume (area) is lower in simulations with a larger azimuthal extent. Here we want to note that our larger boxes with $H/r = 0.1$ and $L_y = 32\,H$ are only a factor of about two shy of the equivalent 2π global simulation.

Overall, we conclude that the baroclinic vortex amplification works reasonably well for entropy gradients as low as $\beta = 0.5$. This β corresponds to a Richardson-number of $Ri = -1.5 \times 10^{-3}$. This makes BVA a feasible mechanism for angular momentum transport in the dead-zone.

An exploration of lower entropy values will have to be postponed due to the long evolution time required. In the future we will study stratified 3D boxes and the interaction of dust with the vortices.

Chapter 4

Particle Trapping and Streaming Instability

4.1 Introduction

Planetesimal growth is one of the key issues of planet formation. The standard model of collisional sticking poses several difficulties. Whether small dust grains stick to one another or fragment depends on their size and their relative velocities. In general, theory predicts that collisional velocities rise as particles grow. Fragmentation occurs at velocities of only a few ms^{-1}, which limits particles sizes (Wurm and Blum, 2000; Brauer et al., 2008; Birnstiel et al., 2010). Güttler et al. (2010) and Zsom et al. (2010) introduced another boundary, the so called bouncing barrier where particles hit one another and bounce without mass transfer. At even smaller size scales, Okuzumi et al. (2011a,b) found the charging barrier, where small particles are prevented from approaching one another due to the electric charges built up through collisions with free electrons.

To form large planetesimals these difficulties need to be circumvented. One proposed method is gravitational instability (Goldreich and Ward, 1973; Johansen et al., 2006a). When enough particles are close enough together, their mutual attraction can trigger gravitational collapse, instantaneously forming large planetesimals that then sweep up small particles. Different methods to capture dust have been studied by various groups, such as zonal flows by Johansen et al. (2011), rings around stars (Klahr and Lin, 2001, 2005), convective cells (Klahr and Henning, 1997) or vortices either numerically (Barge and Sommeria, 1995; Johansen et al., 2004; Klahr and Bodenheimer, 2003) or analytically (Chavanis, 2000; Chang and Oishi, 2010).

It has become clear that dust can concentrate in anti-cyclonic vortices. However the studies do not choose a particular formation mechanism for these

vortices. In our studies, vortices are produced by baroclinic effects (Klahr and Bodenheimer, 2003; Petersen et al., 2007a,b; Lyra and Klahr, 2011).

In this chapter we want to find out how efficiently dust can be captured by vortices created by the baroclinic instability. We do this via 2 dimensional, local simulations. Back-reaction of the particles onto the gas is included for some simulations because we expect to reach high particle concentration in the vortices.

The chapter is structured as follows. We first explain the underlying physics of dust-motion in a gas disc, specifically in a vortex including dust-gas interactions. Then we describe the changes in the numerical setup compared to the pure gas simulations from the previous chapter in section 4.3. The results of our simulations are given in section 4.4. Here we especially look at the reached dust-to-gas ratios depending in initial dust-to-gas ratio. Finally we summarize and conclude in section 4.5.

4.2 Physical Background

To understand how particles move in a vortex we first have to understand how they move in a protoplanetary disk and how they interact with gas. In general the gas and dust feel the same forces except the pressure force $f_p = -\rho_{\mathrm{g}}^{-1}\nabla p$ [8]. This term only affects the gas. with the global pressure gradient leading to a sub-Keplerian orbital gas velocity $\boldsymbol{u}$. The corresponding term $f_{p,\mathrm{s}} = -\rho_{\mathrm{s}}^{-1}\nabla p$, where ρ_{s} is the material density of the solid material, can be neglected because $\rho_{\mathrm{s}} \gg \rho_{\mathrm{g}}$. Since the particles do not feel this global pressure, they orbit at Keplerian velocities. The resulting velocity difference between gas and particles, acts as a headwind. Large particles are less affected by this headwind than small particles which are dragged along with the gas.

The time on which the dust particles adjust to the gas velocity is the friction time $\tau_s = \rho_{\mathrm{s}} s(\rho_{\mathrm{g}} c_s)^{-1}$ which depends on particle size s, particle material density ρ_{s}, gas density ρ_{g} and local sound speed c_s. This particle gas coupling is usually expressed on terms of the dimensionless Stokes-number $St \equiv \Omega\tau_s$. Particles of different size, but with the same St will behave the same as far as aerodynamics is concerned.

Since our simulations are only 2 dimensional we do not consider vertical settling of particles.

A simplified version of the equations of motion for gas and dust is

[8] we now added the index g to the gas density to avoid confusion with the dust density ρ_{d}, and dust material density ρ_{s}

$$\dot{\boldsymbol{u}} = \text{forces} - \frac{1}{\rho_\text{g}}\boldsymbol{\nabla} p - \frac{\rho_\text{d}}{\rho_\text{g}\tau_s}(\boldsymbol{u} - \boldsymbol{v}) \tag{4.1}$$

$$\dot{\boldsymbol{v}} = \text{forces} - \frac{1}{\rho_\text{s}}\boldsymbol{\nabla} p - \frac{1}{\tau_s}(\boldsymbol{v} - \boldsymbol{u}) \tag{4.2}$$

where $\boldsymbol{v}$ is the particle velocity and "forces" collects the terms that are the same for both dust and gas, such as the gravitational force from the central star and the Coriolis force. The second term of the equations describe the pressure force, and the third term in the equations is the friction force between gas and dust particles. If now we assume a steady state and that the back-reaction from the dust in the gas is neglected and equation (4.2) is subtracted from equation (4.1) we get

$$\boldsymbol{v} = \boldsymbol{u} + \tau_s \frac{1}{\rho_\text{g}}\boldsymbol{\nabla} p. \tag{4.3}$$

This shows that particles tend to move up pressure gradient.

Baroclinic vortices are high pressure regions, so they should concentrate particles. The vortex itself is geostrophicly stable which means that pressure forces and Coriolis forces balance each other

$$\Omega \times \boldsymbol{u} = -\frac{1}{\rho_\text{g}}\boldsymbol{\nabla} p. \tag{4.4}$$

It is also the Coriolis force that cause particles to move on epicycles around the vortex. Yet the particles do not feel the pressure support, which means that they are faster than the gas. However, small dust couples well to the gas, and therefore adopts the gas velocity. Since these particles now are too slow for force balance they migrate towards the center of the vortex. The large particles on the other hand do not couple well to the gas, but they feel a head wind and thus lose angular momentum and also spiral towards the center to compensate the angular momentum loss. In principle the accumulation towards the center of a vortex works the same way as radial particle drift in an accretion disk. Barge and Sommeria (1995) also analyzed all forces acting inside a vortex and found that all particles captured by an anti-cyclonic vortex experience an inward driving force. In cyclonic vortices these forces act outwards.

If the dust density becomes comparable to the gas density the drag forces that particles have onto the gas can no longer be neglected. This back-reaction can alter the motion of the gas and also lead to even higher dust concentrations through the streaming instability (Youdin and Goodman, 2005). The last term of equation (4.1) represents the back-reaction and the local dust-to-gas ration is expressed as

$$\varepsilon = \frac{\rho_\text{d}}{\rho_\text{g}} \tag{4.5}$$

4.3 Numerical setup

We perform 2 dimensional shearing sheet simulations with the PENCIL CODE. The linearized Euler-equations for the gas are solved on a cartesian grid. For the exact form of the gas equations, see equations 3.6 through 3.8 in chapter 3. When back-reaction on the gas is included we add the last term of equation (4.1) to equation (3.7). The dust grains are modeled with a particle approach. For each individual particle we solve the equation of motion including gas drag. We do not allow for self-gravity so far. In principle, for an individual particle it does not matter if there are other particles in the simulation or not. However, in the simulations where we allow for back-reactionof the particles on the gas, there is an indirect influence of one particle on the other particles due to the altered gas velocity.

In chapter 3.3 we set our disk co-rotating with Keplerian velocity at the co-rotational radius R_0. But for simulations involving both dust and gas we need to include a velocity offset due to the pressure gradient. The pressure gradient is balanced by the Coriolis force

$$2\Omega u_y = \frac{1}{\rho_g}\frac{\partial P}{\partial r} = c_s\Omega\frac{H}{r}\frac{\partial \ln P}{\partial \ln r}. \tag{4.6}$$

The deviation by which the gas velocity is lower than the Keplerian velocity $u_K = \Omega r$ is (Nakagawa et al., 1986)

$$\eta = 0.5\left(\frac{H}{r}\right)^2\frac{\partial \ln p}{\partial \ln r} \tag{4.7}$$

which leads to a sub-Keplerian gas velocity of

$$u_y = 0.5\left(\frac{H}{r}\right)^2\frac{\partial \ln p}{\partial \ln r}\Omega r = \eta u_K. \tag{4.8}$$

This velocity deviation η is added to the simulations artificially. For our 2D simulations we choose $\eta = -0.01$ which corresponds to a pressure gradient of $\beta = 2.0$ and a disk aspect ratio of $h = 0.1$. The particle velocities in terms of η are now (Weidenschilling, 1977a)

$$v_x = \frac{2\eta u_K}{St + St^{-1}} \tag{4.9}$$

$$v_y = \frac{\eta u_K}{St^2}. \tag{4.10}$$

Our physical domain spans 4 disk scale-heights, $\pm 2H$, around the co-rotational radius in radial-direction (x-axis) and $16H$ in azimuthal-direction

Table 4.1. Simulation setup and ε_{max}

run	St	$\Sigma_{d,0}/\Sigma_{g,0}$	feed-back	ε_{max}
NF1	0.01	1 : 100	no	5.35
NF2	0.05	1 : 100	no	416.67
NF3	1.0	1 : 100	no	416.67
NF4	20.0	1 : 100	no	1.67
F1	0.01	1 : 100	yes	1,07
F2	0.05	1 : 100	yes	3.86
F3	1.0	1 : 100	yes	77.33
F4	20.0	1 : 100	yes	0.73
DG1	0.05	1 : 1 000	yes	1.15
DG2	0.05	1 : 10 000	yes	0.70
DG3	1.0	1 : 1 000	yes	11.53
DG4	1.0	1 : 10 000	yes	4.17

(y-axis). The grid itself consists of 288^2 gridcells. We choose $\beta = 2$ for the entropy gradient and pressure gradients. This is a relatively strong gradient. Gradients we expect in protoplanetary accretion disks are closer to $\beta = 0.5$. However, in chapter 3, we saw that the general behavior of the vortices is the same for weak and strong entropy gradients. The development of the vortices is merely faster with stronger gradients. For a first estimation this strong gradient is reasonable.

We first evolve the disk for 200 local orbits without particles. This way we make sure that a fully grown, long lived vortex has developed before we put in particles. Physically, this corresponds to a vortex developing in the outer parts of the disk and then migrating inwards through regions with particles.

After these 200 orbits, we distribute 400 000 particles randomly in the disk. This corresponds to 4-5 particles per gridcell initially. That way we avoid numerical effects that can arise if there are not enough particles in the computational domain, e.g. the effect a single particle has can be extremely overestimated if not enough particles are considered. Whenever we refer to times in this chapter, we mean time elapsed since particles were put into the simulation.

Each of the 400 000 particles represents one super-particle, a collection of several particles, all of the same size, and a given mass according to the initial dust-to-gas ratio.

Generally we have an initial dust-to-gas ratio ε_0 of 1:100 which means that the disk consists out of 1% solid material and 99% gas. Please note that in

2 dimensions the PENCIL CODE assumes surface densities instead of volume densities. Therefore the dust-to-gas-ratios we talk about in this chapter refer to $\varepsilon = \Sigma_d/\Sigma_g$ rather than to $\varepsilon = \rho_d/\rho_g$. To simulate different particle sizes we use different Stokes-numbers of $St = 0.01$, $St = 0.05$, $St = 1$ and $St = 20$. At 5 AU this corresponds to particles between 3mm and 6m for $\Sigma_g = 300\,\mathrm{g\,cm^{-2}}$ and $\rho_s = 2\,\mathrm{g\,cm^{-3}}$. The parameters for all our simulations can be seen in table 4.1. A separate simulation is carried out for each St.

4.4 Results

4.4.1 No Particle Feedback

First we do not include back-reaction from the particles, effectively setting $\rho_d = 0$ in equation (4.1). That means that gas drags particles along, but even high dust densities do not affect the gas velocity in any way. We see two different scenarios. For $St = 0.05$ and $St = 1.0$ particles, all particles are collected within the vortex while for $St = 0.01$ and $St = 20.0$ there is no high concentration inside of vortex.

This can be explained through the gas coupling. Particles with $St = 0.01$ are perfectly coupled to the gas. This means they "glue" to one fluid element. Since it is not always the same fluid element within the vortex, the dust particles can leave the vortex again. The $St = 20$ particles are the other extreme: they are hardly coupled to the gas, and therefore are not affected by the vortical motion of the gas.

Only the intermediately coupled particles can be swept up entirely by the vortex as they drift through it. They are not so well coupled to the gas that they can leave the vortex again, and other forces acting on the particles, like the Coriolis force lead to a concentration in the center of the vortex.

Figure 4.1 shows the maximum dust-to-gas ratio for these simulations. It is clear from the constant lines that all of the available solid material in the $St = 0.05$ and $St = 1.0$ particle simulations accumulates in the vortex. This corresponds to a particle concentration $c = \Sigma_d/\Sigma_{d,0} \approx 45\,000$ and $\varepsilon \approx 540$. Even for $St = 0.01$ particles the dust-to-gas ratio increases to $\varepsilon \approx 1$.

The maximum particle concentration is reached sooner for $St = 1$ particles than for $St = 0.05$ particles. This can be attributed to the radial drift velocity. $St = 1$ particles have the highest radial drift velocities (Weidenschilling, 1977a). Therefore they drift into the vortex faster than all other particles they are then kept trapped.

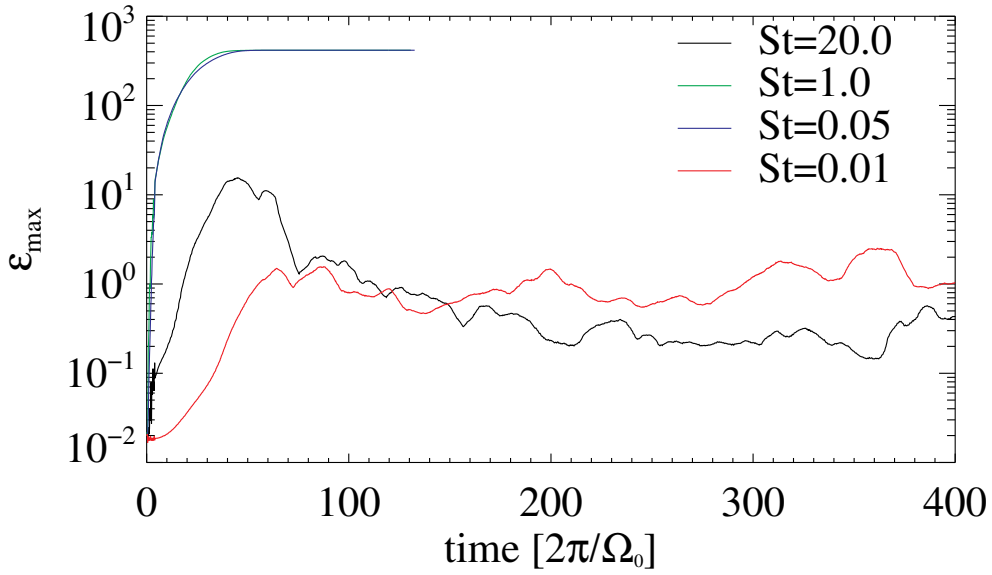

Figure 4.1 Maximum dust-to-gas ratio, ε_{max}, for simulations without particles feedback. The different lines represent the different particle sizes: solid (black) line: $St = 20$, dashed-dotted (green) line: $St = 1$, dashed (blue) line: $St = 0.05$, and dotted (red) line: $St = 0.01$. All particles of intermediate size ($St = 1.0$ and $St = 0.05$) are accumulating in the vortex. Perfectly coupled particles ($St = 0.01$) only partly accumulate inside the vortex, because they also couple to the gas outside of the vortex. Large particles ($St = 20$) hardly couple to the gas at all. Therefore these particles are not affected by the vortical gas-motion.

4.4.2 Including Particle Feedback

In the last section we showed that there are enormous particle overdensities within the vortex. This means that we cannot neglect the effect that dust has on gas. Because of this we now include dust back-reaction on the gas, using the full equation (4.1).

For the $St = 20.0$ particles there is no change to the simulations without particle feedback (compare the left and right side of the to panel in figure 4.2). All other tested particles still accumulate in the vortex, yet differently:

Particles with higher Stokes number ($St = 1.0$) concentrate more locally (in a smaller area) than smaller particles (bottom panel of figure 4.2 and figure 4.3). For those particles, the pressure gradient across the vortex combined with the Coriolis forces inside the vortex, both of which act to concentrate particles in the center, outweigh the drag force of the gas which acts to separate dust over

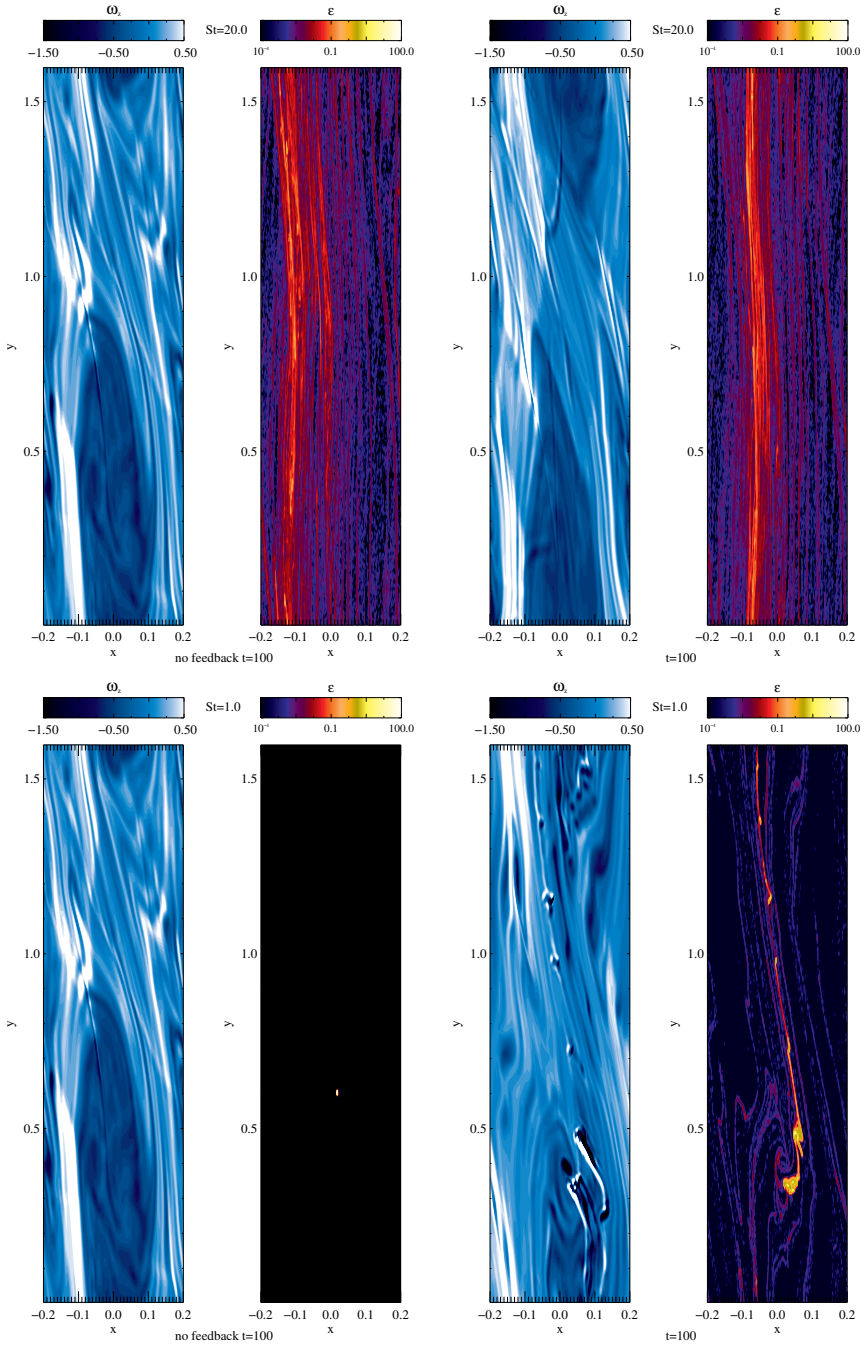

Figure 4.2 Vorticity ω_z and dust-to-gas ratio without particle feedback (left) and including back-reaction (right) for $St = 20.0$ (top) and $St = 1.0$ (bottom) particles.

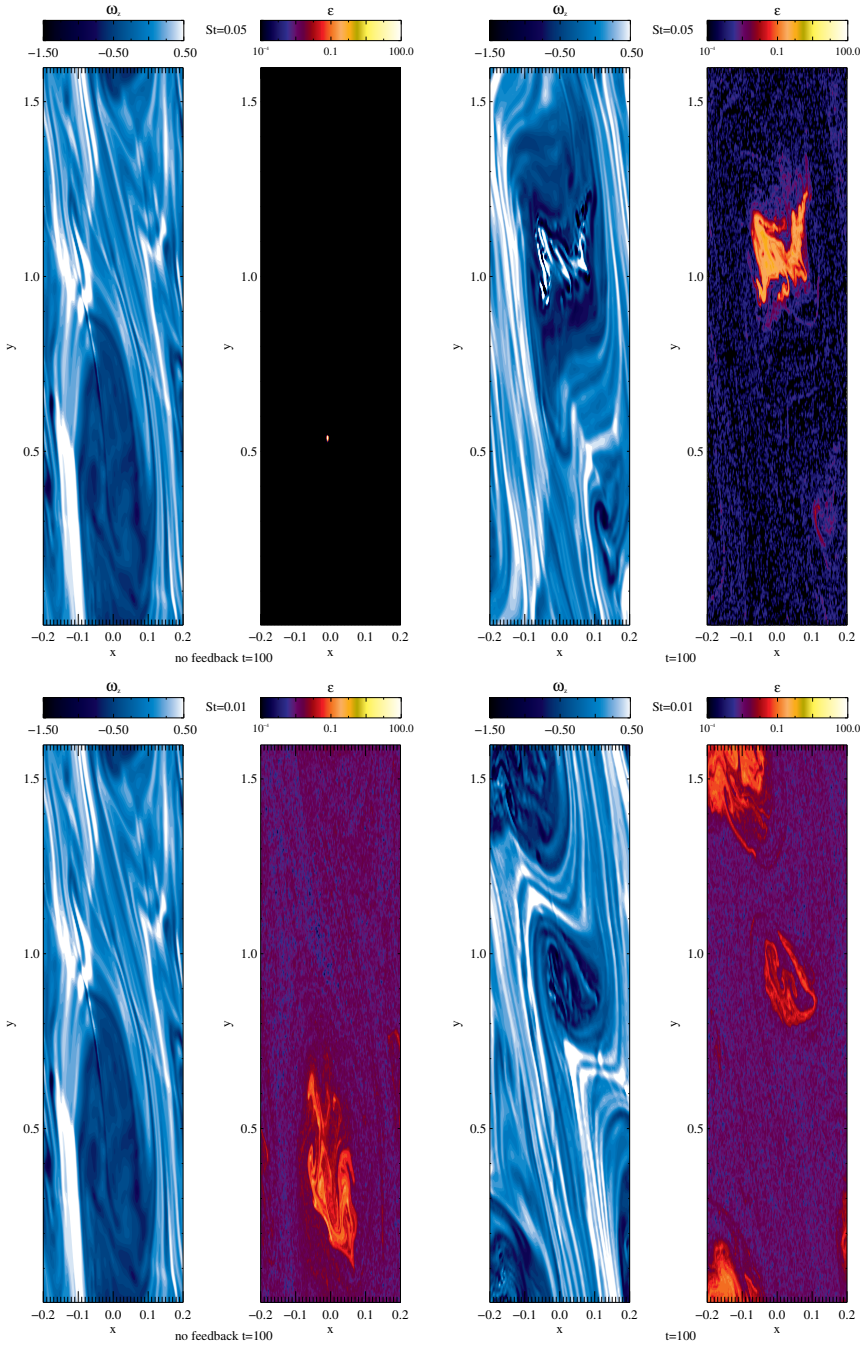

Figure 4.3 Vorticity ω_z and dust-to-gas ratio without particle feedback (left) and including back-reaction (right) for $St = 0.05$ (top) and $St = 0.01$ (bottom) particles.

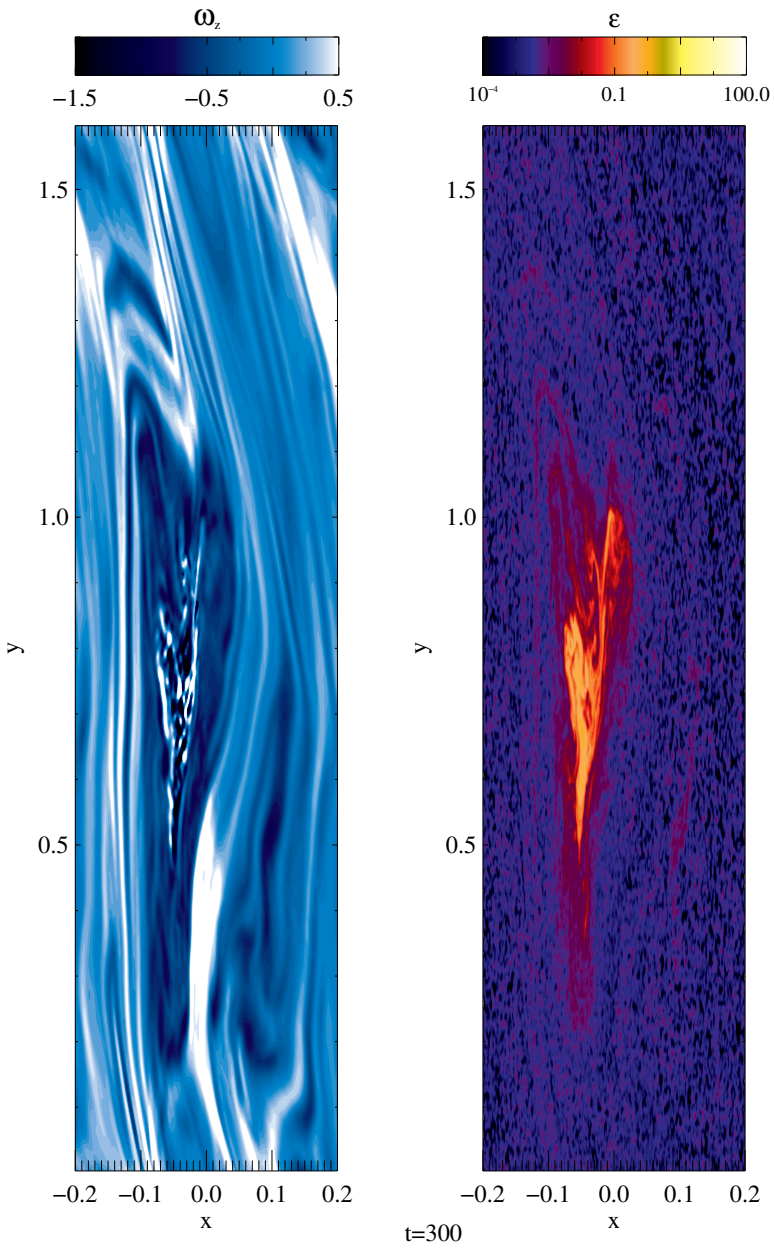

Figure 4.4 Vorticity of the gas flow (left panel) and dust-to-gas ratio (right panel) for a simulation with $St = 0.01$ particles and back-reaction onto the gas. The elliptical vortical gas flow is distinguishable in the vorticity plot. There are strong accumulations of particles within the vortex. Although many particles spread out over the entire vortex, most particles concentrate in the center of the vortex. The positive vorticity values in the vortex (light areas in the left plot) show the effect the particles have on the gas. Where the gas encounters obstacles, namely high particle concentrations, steep vorticity gradients are developed.

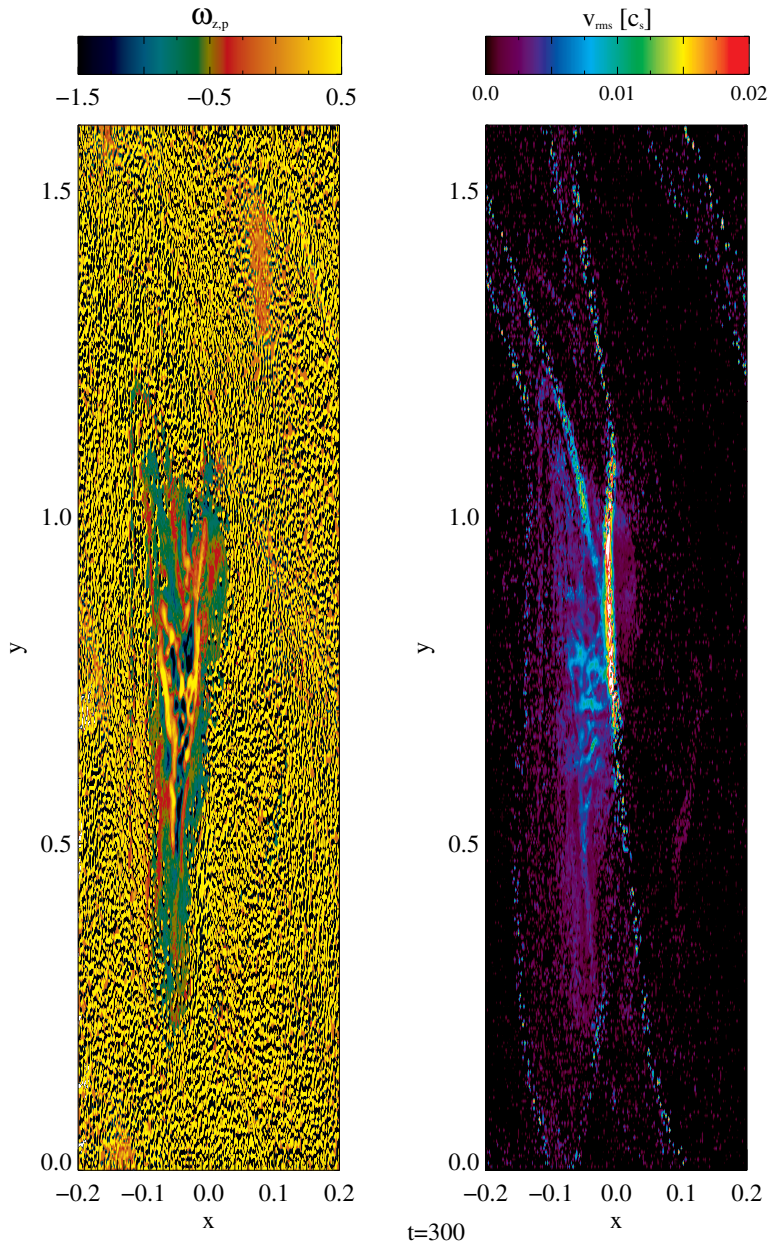

Figure 4.5 Vorticity of the dust particles (left panel) and particle rms velocity (right panel) for the same snapshot as in figure 4.4. The particle vorticity agrees well with that of the gas, which confirms that the particles follow gas. Note that the particle velocity peaks coincide with the particle concentration peaks.

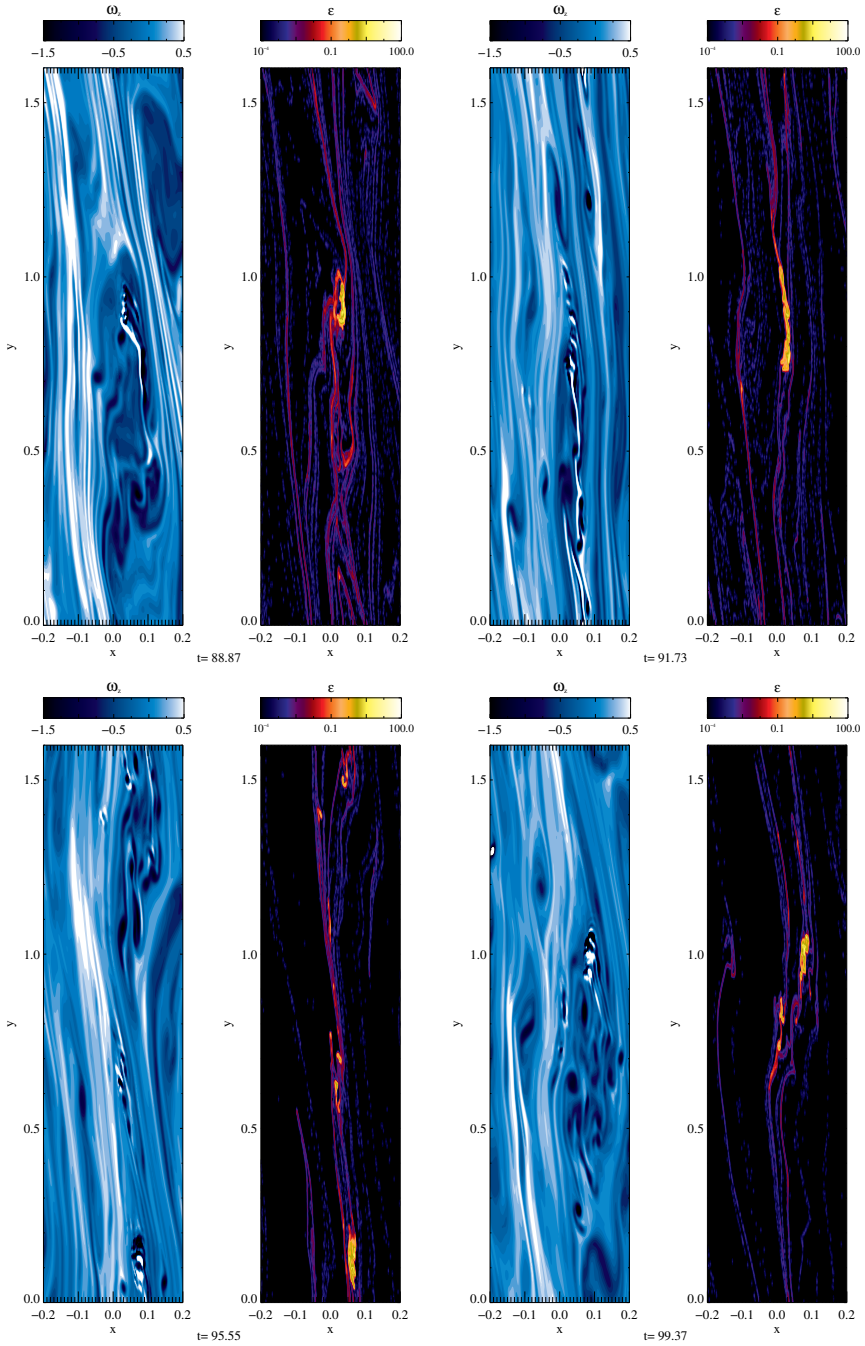

Figure 4.6 Vorticity (1st and 3rd column) and dust-to-gas ration (2nd and 4th column) for $St = 1.0$ particles for different points in time. At the first snapshot, the vortex is still clearly distinguishable. In the second snapshot, it has been disrupted strongly by the particle accumulation. As this particle accumulation spreads out, it can slowly regain its shape (3rd snapshot) and form a large, yet still perturbed, vortex again (4th snapshot).

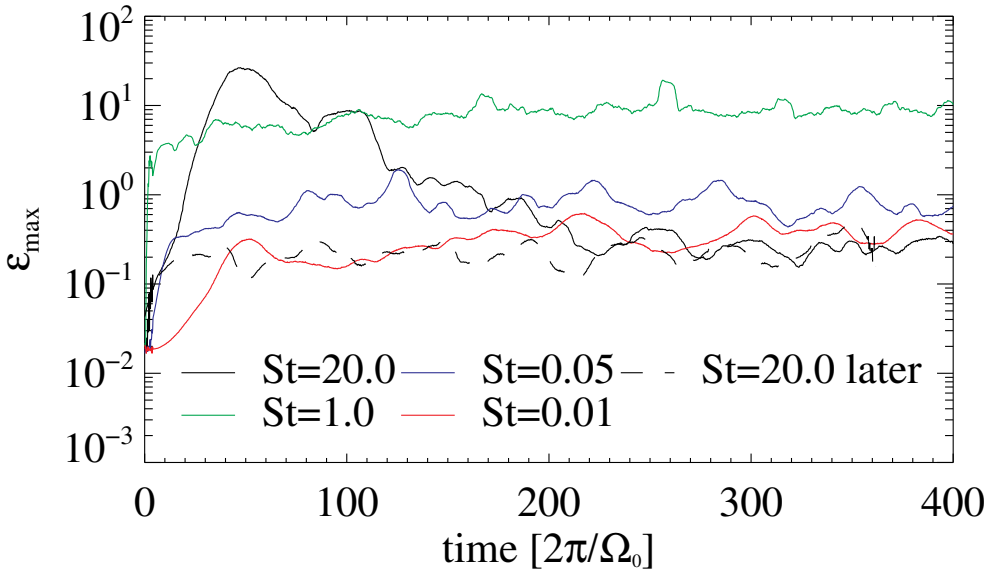

Figure 4.7 Maximum dust-to-gas ratio, ε_{max}, for simulations with particle feedback. The different lines represent the different particle sizes: solid (black) line: $St = 20$, dashed-dotted (green) line: $St = 1$, dashed (blue) line: $St = 0.05$, and dotted (red) line: $St = 0.01$. Particles of $St = 1.0$ reach the highest dust enhancements and concentrate in a very local area in the vortex, while smaller particles spread out over the entire vortex.Therefore the overdensities reached are lower. The high dust-to-gas ratio for large particles ($St = 20.0$) is attributed to initial conditions. The black dashed line shows the same simulation for $St = 20.0$, but the location of the particles was kept constant until the particle velocity has adopted an equilibrium velocity.

the vortex. Smaller particles spread out over the vortex because their coupling to the gas is stronger.

An effect visible in the behavior of small particles is the streaming instability (Youdin and Goodman, 2005; Youdin and Johansen, 2007). Once particles concentrate, their locally increased dust-to-gas ratio leads to a slower radial drift (Nakagawa et al., 1986). This leads to further enhancement of solids since faster particles from slightly larger radii bump into the accumulation, like a traffic jam. This leads to streaming dust structures.

Figures 4.4 and 4.5 show the vertical gas vorticity ω_z, dust-to-gas ratio $\varepsilon = \Sigma_d/\Sigma_d$, the vertical vorticity component of the particles $\omega_{z,p}$ and the rms velocity of the particles v_{rms} for a simulation with $St = 0.01$ particles after 300 local orbits (run F1). It is clear that the particles accumulate inside of the vortex and follow the vortical motion. Where the concentration is highest they

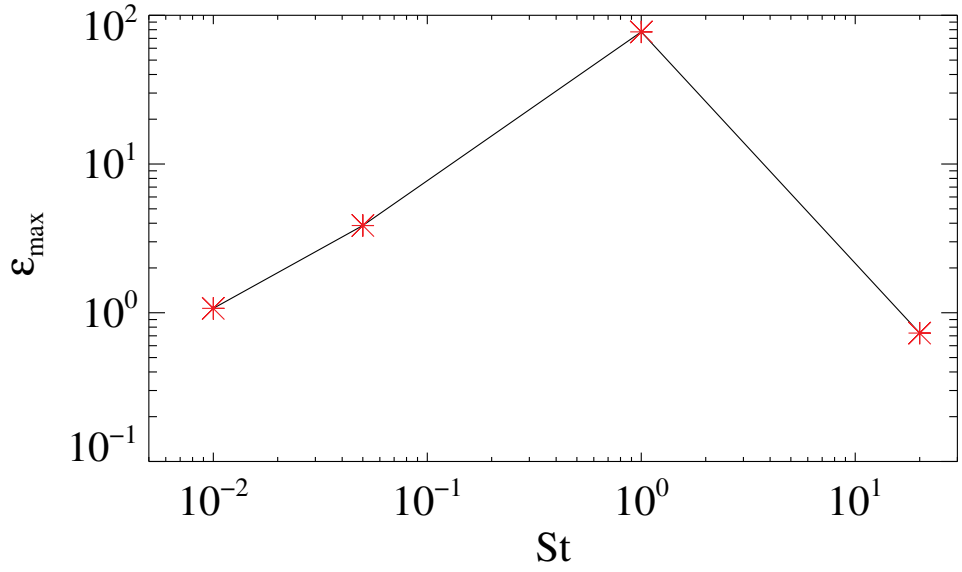

Figure 4.8 Highest dust-to-gas-ratios obtained during the simulations. $St = 1$ particles reach the highest ε whereas smaller and larger particles reach lower ε.

create steep gradients in both the gas's vorticity and their own. Due to the back-reaction of the dust on the gas, the initially elliptical gas streamlines are bent into more complicated motions.

Similar effects are known as Karman vortex street. If a flow meets a cylinder or other obstacle, in our case the particle accumulation, then the flow will interact with the obstacle surface resulting in turbulent vortices once it has passed the obstacle (Davidson, 2004).

In case of the $St = 1.0$ particles where the local particle concentration, and therefore the back-reaction, are strongest, the vortex structure is disrupted, and begins to fall apart. Because of this, the particle trapping mechanisms lose strength: pressure gradients across the vortex become shallower, Coriolis force in the vortex grows weaker, and the particles begin to escape the vortex. Because the local particles concentrations decreases the large vorticity gradients flatten out again. This eventually leads to a re-establishment of the vortex and the process repeats itself (see series of snapshots in figure 4.6).

For large particles there is no longterm concentration within the vortex. The initial large accumulation (see figure 4.7) can be traced back to the initial particle velocity, which is zero. When the gas profile is imprinted onto the particles, there is a large velocity difference between particles and gas. Therefore drag-force on the particles is larger than one would normally expect. After several

Table 4.2. Fraction of dust mass with specific ε

St	fraction of M_d with $\varepsilon \geq 0.01$(%)	fraction of M_d with $\varepsilon \geq 1.0$(%)
0.01	70.40	0.00
0.05	95.24	2.13
1.0	98.73	83.74
20.0	79.82	8.09

orbits the particle velocity adopts an equilibrium velocity and the drag-force has the expected influence. We tested this assumption with a test run where we initially updated the particle velocity but not the location. After several orbits, when the particle velocity had reached equilibrium, we started to update the particle location. In this run we did not see the initial high accumulation (see black dashed line in figure 4.7).

Figure 4.7 shows the maximum dust-to-gas ratio of our different simulations with different St. We clearly see that $St = 1.0$ particles (green line) have the highest concentration. As the particle size decreases, the concentration also decreases. It is important to note that $St = 20.0$ particles do not accumulate inside the vortex. Figure 4.8 shows the maximum dust-to-gas ratio obtained during the simulations. The highest dust-to gas ratio is reached for $St = 1.0$ particles. Larger and lower St reach lower dust-to-gas ratios. As explained, the initial high particle concentration if the $St = 20.0$ particles can be attributed to the initial condition. Therefore, we use the run with the altered initial condition, for this analysis.

The values we discussed so far were maximum values. They do not tell us if all of the dust is concentrated that highly or if only a small fraction of the dust is concentrated and the remaining amount of dust is spread equally over the simulation domain. Clustering has to be considered to figure out what fraction of the dust takes part in the high overdensities. In figure 4.9 we show what fraction of the entire dust content M_d has a specific dust-to-gas ratio. The dashed lines indicate the initial dust-to-gas ratio $\varepsilon_0 = 0.01$ and $\varepsilon = 1.0$. For e.g. $St = 1.0$ particles 83.74% have accumulated in regions with $\varepsilon \geq 1.0$ where as for $St = 0.05$ particles only 2.13% of the entire dust mass is concentrated in areas with $\varepsilon \geq 1.0$. The remaining dust is spread our thinner. All values can be see in table 4.2. A dust-to-gas ratio of $\varepsilon = 1.0$ is significant, because that is when dust back-reaction on the gas becomes important. This means that for $St = 1.0$ back-reaction is a requirement if we want to model particle behavior realistically. However, for the other St it seems that back-reaction, and

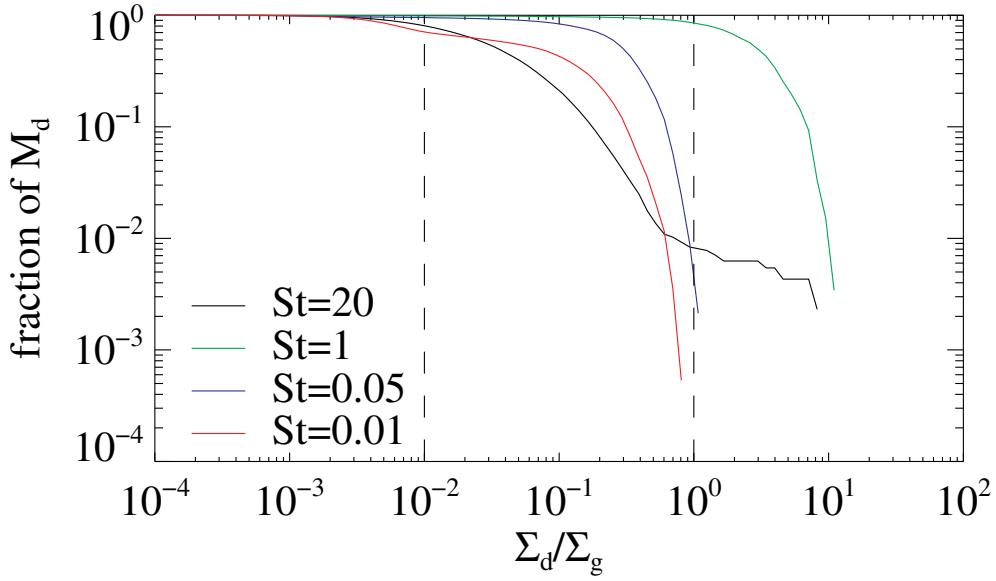

Figure 4.9 Fraction of the entire dust mass in a specific dust-to-gas ratio or higher. $\varepsilon \geq 1.0$ are reached for all particle sizes. For $St = 1.0$ particles more than 80% of all particles have concentrated in areas with larger ε than 1.0

with that the streaming instability, contributes little to the overall dynamical behavior of particles. Yet, we already saw that there is a significant difference between the simulations with and without particle feedback for $St = 0.05$ particles (see figures 4.1 and 4.7). Without feedback all particles were accumulated in the vortex whereas the maximum dust-to-gas ratio with feedback was around $2 - 8$, two orders of magnitude lower. Also for $St = 0.01$ particles that only reach $\varepsilon_{max} \approx 1.0$ we already saw that there an effect onto the gas (see figures 4.4 and 4.5).

We conclude that as soon as only a fraction of particles approaches $\varepsilon \approx 1.0$, even if it is only a few %, back-reaction from the particles onto the gas needs to be included to accurately model their behavior.

Mass Collected in the Vortices

The goal of collecting particles in a vortex was to achieve particle accumulations that will eventually lead to gravitational collapse. To give an estimate of how heavy the planetesimals could be if gravitational collapse would be allowed, we calculate the mass of solid material trapped within the vortex. Therefore, we first have to calculate the mass of each of the super-particles to maintain $\varepsilon_0 = 0.01$. We assume two scenarios. One where the vortex is located

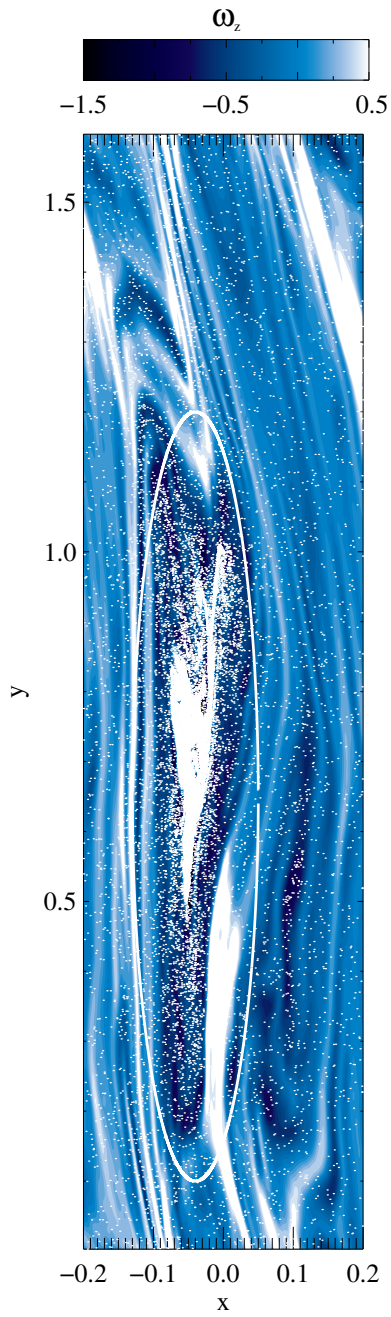

Figure 4.10 Vorticity of the gas flow. Each white dot represents one individual superparticle of $St = 0.01$. They accumulate within the vortex marked by the white ellipse.Depending on disk model there is between 8.56×10^{26}g and 3.11×10^{28}g of solid material caught within the vortex.

Table 4.3. Mass in computational domain

case	$\Sigma_0\,(r_0)$ (gcm^{-2})	$\rho_\mathrm{g}(r_0)$ (gcm^{-3})	r (AU)	$\Sigma_0\,(r)$ (gcm^{-2})	M_g (g)	M_s (g)	M_p (g)
1	150	7.67×10^{-12}	5.2	150	5.84×10^{29}	5.84×10^{27}	1.46×10^{22}
2	150	1.76×10^{-10}	1.0	661	9.51×10^{28}	9.51×10^{26}	2.38×10^{21}
3	800	4.09×10^{-11}	5.2	800	3.11×10^{30}	3.11×10^{28}	7.78×10^{22}
4	800	9.39×10^{-10}	1.0	3528	5.08×10^{29}	5.08×10^{27}	1.27×10^{22}

at 1 AU and one where it is located at 5.2 AU. To derive the mass of each individual super-particle, we first have do estimate the total gas mass within the simulation domain. According to Weidenschilling (1977b) the disks surface-density profile follows the law:

$$\Sigma_\mathrm{g}\,(r) = \Sigma_0 \left(\frac{r}{r_0}\right)^{-\beta_\Sigma}, \tag{4.11}$$

where Σ_0 is the surface density at a certain radius r_0, fixed to 5.2AU in our calculations, and β_Σ is the slope with which Σ_g declines. Through analyzing observed disk profiles Andrews et al. (2009) found $\beta_\Sigma = 0.9$. If we consider $\Sigma_0 = 150\,\mathrm{g\,cm^{-2}}$ at $r_0 = 5.2$ AU which agrees with the Minimum Mass Solar Nebula (Weidenschilling, 1977b), we get a mass of each superparticle of $M_\mathrm{p} = 7.78 \times 10^{22}$ g at 5.2 AU, and a mass of $M_\mathrm{p} = 2.38 \times 10^{21}$ g at 1 AU. Since the MMSN only gives a lower mass threshold to form our Solar System, it is generally considered not massive enough we also consider a heavy disk with $\Sigma_0 = 800\,\mathrm{g\,cm^{-2}}$ at r_0. See Table 4.3 for values of the entire amount of gas M_g and solids M_s in the computational domain for the different cases. We also calculate the corresponding gas density according to

$$\rho_\mathrm{g} = \frac{\Sigma_\mathrm{g}}{\sqrt{2\pi}H} \tag{4.12}$$

To calculate the actual mass of solid material within a vortex, we visually define an ellipse around the vortex and then count the super-particles within the vortex, as is shown in Figure 4.10. Although the vortex itself is not a well defined ellipse anymore but rather has irregular shape, an ellipse still is a good approximation since most of the particles are concentrated in the central region.

Depending on disk-model and St, the mass within the vortex M_v varies from $0.09\,M_\mathrm{Earth}$ for $St = 0.01$ at 1 AU for the MMSN model up to $8.16\,M_\mathrm{Earth}$ for $St = 1.0$ particles at 5.2 AU and $\Sigma_0 = 800\,\mathrm{g\,cm^{-2}}$. All masses for the different cases can be seen in table 4.4. The calculation was done after 300 local orbits.

Table 4.4. Mass inside of the vortex

case	$M_\mathrm{v}\,(St = 0.01)$ (g)	$M_\mathrm{v}\,(St = 0.05)$ (g)	$M_\mathrm{v}\,(St = 1)$ (g)
1	5.25×10^{27}	5.76×10^{27}	5.82×10^{27}
2	8.56×10^{26}	9.38×10^{26}	9.49×10^{26}
3	2.80×10^{28}	3.07×10^{28}	3.11×10^{28}
4	4.57×10^{27}	5.01×10^{27}	5.07×10^{27}

The amount of particles that are caught within the vortex for $St = 1.0$ fluctuates rapidly. When the concentration is very high it disturbs the vortex, causing he concentration to drop. The particle accumulation for $St = 0.05$ and $St = 0.01$ is relatively constant over time.

We did not conduct this analysis for $St = 20$ particles because they were not accumulating in the vortex.

Possible Gravitational Collapse of Particles

While all simulations accumulate a substantial amount of particles, this does not mean that the entire amount of particles would collapse into a planetesimal if self-gravity was turned on. Gravitational particle collapse, like any other self gravitating process, requires a critical density. The trapped small particles are spread out over the entire vortex and therefore might not pass this critical density.

A good estimate for whether a clump of matter is held together by its own gravity against tides and thus can undergo collapse, is to compare its density with the Roche density ρ_R. It can be derived by equating the the gravitational force on the surface of a clump

$$a_{g,\mathrm{c}} = \frac{GM_\mathrm{c}}{R_\mathrm{c}^2}, \tag{4.13}$$

where M_c and R_c are the clumps mass and radius respectively, with the tidal acceleration a_t on the clumps surface. The tidal acceleration is the difference between the gravitational pull of the central star at the clumps surface and its center of mass. To first order we get

$$a_t \approx \mp 2R_\mathrm{c}\frac{GM_\star}{r^3}, \tag{4.14}$$

where $M_\star$ is the mass of the central object and r is the distance between star and particle clump. If we now equate these two accelerations, exchange the

Table 4.5. Dust density compared to Roche density

run	ε_{max}	ρ_R/ρ_g case1 (5.2 AU)	ρ_R/ρ_g case2 (1 AU)	ρ_R/ρ_g case3 (5.2 AU)	ρ_R/ρ_g case4 (1 AU)
F1	1.01	262	1607	49	301
F2	3.86	262	1607	49	301
F3	77.33	262	1607	**49**	301
DG1	1.15	262	1607	49	301
DG2	0.70	262	1607	49	301
DG3	11.53	262	1607	49	301
DG4	4.17	262	1607	49	301

masses by their respective densities and solve for the clump density we get

$$\rho_{crit} > \rho_R = 2\frac{M_\star}{\frac{4\pi}{3}r^3}. \tag{4.15}$$

If the density of the the particle clump is higher than this critical density it will be held together by its own gravity. If this is not the case then the particle clump will be torn apart by tidal forces.

If we take the mass of the Sun for the mass of the central object then we get $\rho_R(1\,\mathrm{AU}) = 2.83 \times 10^{-7}\,\mathrm{g\,cm^{-3}}$ and $\rho_R(5.2\,\mathrm{AU}) = 2.01 \times 10^{-9}\,\mathrm{g\,cm^{-3}}$. The highest particle densities we reached for $St = 1.0$ particles were $\rho_d \approx 80\rho_g$. To surpass the critical density, ρ_d has to be larger than ρ_R, or $\varepsilon_{max} \geq \rho_R/\rho_g$ (see table 4.5). Considering the density profiles from the last section, this means in only one case, ρ_d reaches ρ_R (indicated in bold in table 4.5). All other cases are 1 to 2 orders of magnitude below ρ_R. Yet, these are 2D simulations. If all three dimensions are considered, then sedimentation of dust grains will further enhance particle densities, then triggering gravitational collapse.

4.4.3 Different Dust-to-Gas ratio

In the previous sections we always considered only one species of dust particles, e.g. the entire amount of solid material consiting of $St = 1$ particles. In reality there is a mix of different dust species of various sizes. To explore this, we also considered lower dust-to-gas ratios like $1:1\,000$ and $1:10\,000$. The number of super-particles we put into the domain stays the same, while each super-particle represents less mass than in cases with higher dust-to-gas ratio.

Figure 4.11 shows the particle accumulation and resulting dust-to-gas ratios for $St = 0.05$ (simulations F2, DG1, DG2) and $St = 1$ (simulations F3,

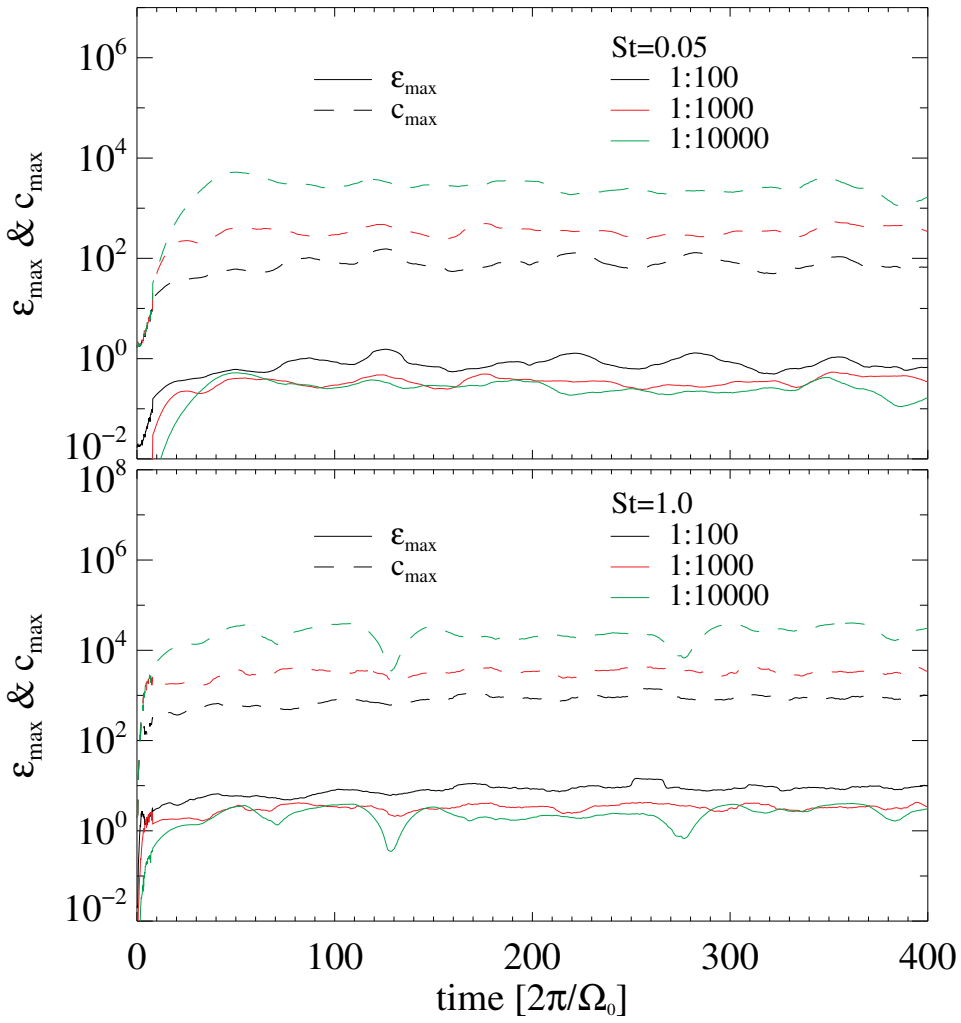

Figure 4.11 Particle concentration (solid lines) and maximum dust-to-gas ratios for $St = 0.05$ (top) and $St = 1.0$ (bottom) particles. The color represent the different initial dust-to-gas ratios: 1 : 100 (black), 1 : 1 000 (red), and 1 : 10 000 (green). More individual super-particles are captured in the vortices for a low initial ε, because their back-reaction is less efficient. Since each of these super-particles is less massive than with higher ε, the overall dust-to-gas ratio for low initial ε is lower than that of larger initial ε.

DG3, DG4). Here the dashed lines show the obtained particle concentration $c = \Sigma_d/\Sigma_{d,0}$ and the solid line the obtained dust-to-gas ratios. The colors represent the original dust-to-gas ratios: $\varepsilon_0 = 1 : 100$, (black); $\varepsilon_0 = 1 : 1\,000$ (red); and $\varepsilon_0 = 1 : 10\,000$ (green).

In cases with low ratios more super-particles concentrate in one location. Since each of these super-particles has less mass than in simulations with

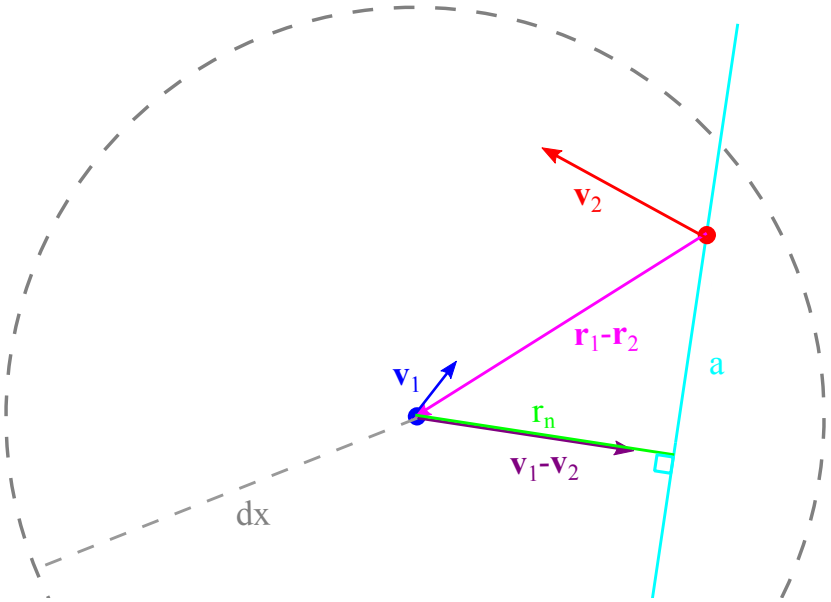

Figure 4.12 Sketch for determining whether two particles collide with one another or not. Particles 1 and 2 are represented by the blue and red dot respectively. Their velocities v_1 and v_2 are indicated through the blue and red arrows. Their relative position and velocity are given through $r_1 - r_2$ in pink and $v_1 - v_2$ in purple. The light blue line represents a plane perpendicular to the relative velocity vector. This plane is the impact plane. The green line shows the shortest distance between particle 1 and the impact plane. dx is the maximum distance two particles are allowed to have to be considered for a collision. The actual impact parameter a is always smaller than dx Particles are considered to collide if their distance to each other is shorter than the impact parameter and if they approach each other.

higher dust-to-gas ratio, the back-reaction is less effective. The gas is not affected as much by the dust particles as in previous simulations. Thus the vortices, although still disrupted slightly by the back-reaction, are no longer torn apart. The particles are trapped more tightly and cannot leave the vortex.

Yet when we correct for the initial dust-to-gas ratio (solid lines in Figure 4.11) it becomes apparent that there is actually less mass captured in the vortex.

4.4.4 Collisional Velocities

In our simulations collisions are not modeled directly. In fact, because we have point particles whose size is set by our numerical accuracy, "real" collisions, where the trajectories of two particles cross each other at the same time, occur rarely, if at all. So when we talk about collisional velocities we rather mean relative velocities adapted to the gas friction. In the following we will discuss

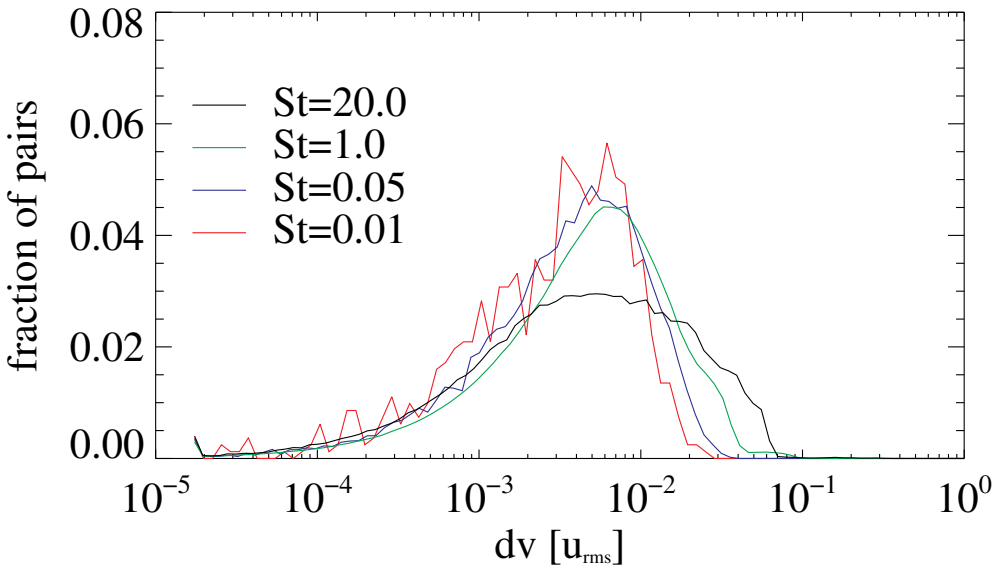

Figure 4.13 Number of collision per velocity bin (number of bins 100) normalized to total number of collisions. In total 10^5 were considered. The maximum impact parameter is $dx = 1$ gridcell.

how we determine a collision between two particles and how we calculate their collisional velocities.

Figure 4.12 shows a sketch of our algorithm. First we determine whether particle 1 and particle 2 are close enough to hit each other. This is done via comparing their distance $\mid \boldsymbol{r}_1 - \boldsymbol{r}_2 \mid$ to the maximum impact parameter dx which we set to the length of one radial gridcell. If this is the case we calculate the relative velocity of the two particles. The next step is to determine a plane of impact where $\boldsymbol{v}_1 - \boldsymbol{v}_2 = \Delta \boldsymbol{v}_{12}$ is a normal vector and one of the particles (particle 2 in our sketch) is located on the plane. This is indicated by the light blue line in the figure. We now go into the rest frame of one of the particles (particle 2 our sketch) and say that the other particle (particle 1) is moving with the relative velocity $\boldsymbol{v}_1 - \boldsymbol{v}_2$ towards the impact plane. The normal distance r_n to the impact plane is the length a particle has to travel to collision and is determined via

$$r_\mathrm{n} = -\frac{(\boldsymbol{v}_1 - \boldsymbol{v}_2) \cdot (\boldsymbol{r}_1 - \boldsymbol{r}_2)}{\mid \boldsymbol{v}_1 - \boldsymbol{v}_2 \mid}. \tag{4.16}$$

As a last step we check if the two particles approach each other which is the case if r_n is positive. This last step is different from most studies of particle collisions like Carballido et al. (2010) for example. They consider all particle pairs within a certain impact parameter independent on whether they approach each other or not.

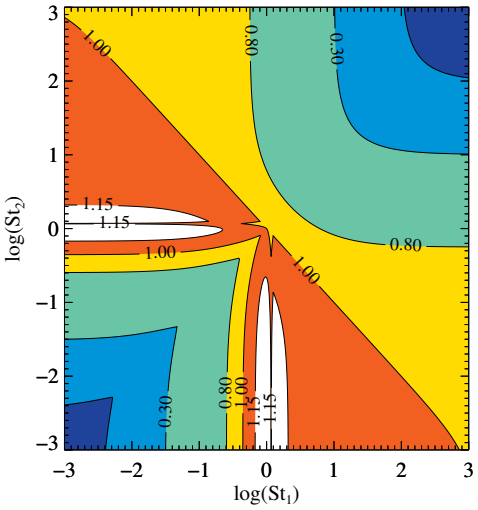

Figure 4.14 Parameter space of collisional velocities of particles with different St according to Ormel and Cuzzi (2007). The velocities derive are based on Kolmogorov turbulence which might not apply to baroclinic turbulence.

Another factor that is not often considered when talking about collisional velocities is that particles will slow down due to their friction with the gas. So instead of merely taking the relative velocity of the two particles as collision velocity, we correct for the velocity that a particle with velocity $\mid \Delta v_{12} \mid = \mid v_1 - v_2 \mid$ looses while traveling the distance $r_{\rm n}$ due to gas friction. This correction is

$$corr = \frac{r_{\rm n}}{\mid v_{12} \mid \tau_s}, \tag{4.17}$$

and the final collisional velocity is

$$v_{\rm coll} = \mid \Delta v_{12} \mid \left(1 - \frac{r_{\rm n}}{\mid \Delta v_{12} \mid \tau_s}\right). \tag{4.18}$$

We calculate the collisional velocities for 100 000 particles which is 25% of all particles and gives a representative sample. The pairs are sorted into 100 logarithmically spaced velocity bins, so that resololution is finer at low velocities. A histogram is shown in figure 4.13. The velocities show the expected trend. $St = 1.0$ particles have the highest collisional velocities whereas smaller particles peak at lower velocities.

Ormel and Cuzzi (2007) derived analytical collision velocities based on turbulence with a Kolmogorv spectrum, and where the strength of the turbulence is determined via the Shakura-Sunyaev α. The assumed relation between α and $u_{\rm rms}$ is $u_{\rm rms} = \sqrt{\alpha} c_s$. The parameter space of collisional velocities is shown in figure 4.14 for collisions of particles of various sizes. Since our simulation

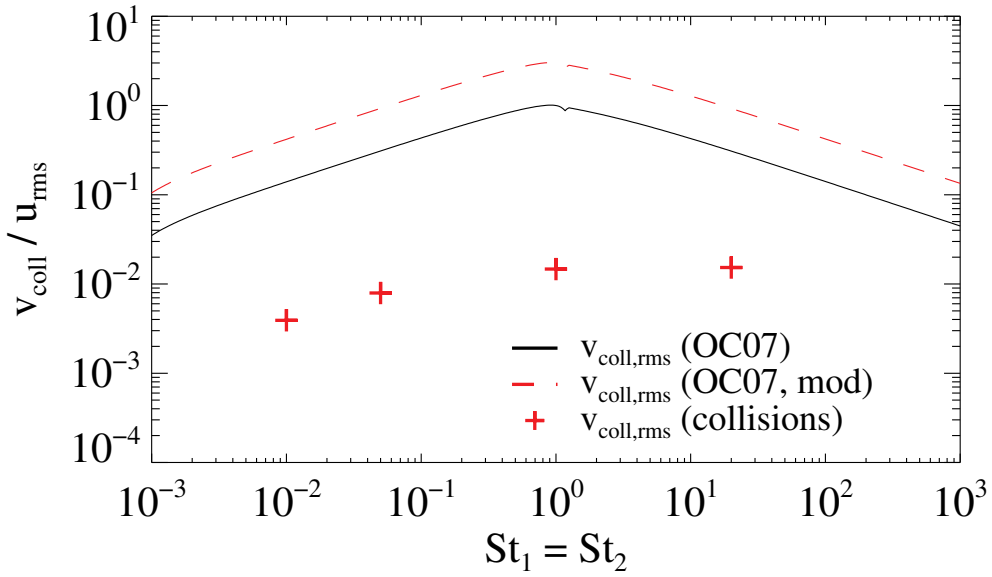

Figure 4.15 The solid line shows the analytically derived collision velocities by Ormel and Cuzzi (2007). The turbulence in this approach follows a Kolmogorov spectrum and the strength is based on $\alpha = 10^{-3}$. The dashed red line assumes the relation $u_{\rm rms} = 3\sqrt{\alpha}c_s$, which we derived in chapter 3, instead of $u_{\rm rms} = \sqrt{\alpha}c_s$ as in Ormel and Cuzzi (2007). The red crosses mark the rms collision velocities we calculate out of our simulations. Although they follow the general trend, they are at least one order of magnitude below the analytically derived velocities.

only consider one particle species at a time we can only compare velocities for collisions of equal size.

Figure 4.15 now only shows collisional velocities for equal sized particles. The solid line shows the results by Ormel and Cuzzi (2007). The red dashed line is a modified version of their model. Instead of the relation $u_{\rm rms} = \sqrt{\alpha}c_s$ we use $u_{\rm rms} = 3\sqrt{\alpha}c_s$ which we deducted in chapter 3. The red crosses show the rms velocities we get from our simulations. The are more than one order of magnitude below the analytical prediction. The reason for this discrepancy might be that the Ormel and Cuzzi (2007) model is based on Kolmogorov turbulence, which might not apply for turbulent flow.

4.5 Summary and Conclusion

In this chapter we have analyzed how particles and vortices created via the baroclinic instability affect each other. In particular, we investigated whether particles of different size can be trapped inside and thus concentrated in vortices and whether the vortices remain a long lived phenomenon under the influence of particles.

We have conducted two sets of simulations for a set of Stokes-numbers ($St = 20.0, St = 1.0, St = 0.05$ and $St = 0.01$). One where there is only gas drag on the particles and one where particles also exert drag on gas. This becomes important if the initial dust-to-gas ratio is enhanced from 0.01 to about 1.0.

We see that without back-reaction, $St = 0.05$, and $St = 1.0$ particles are swept up entirely by the vortices and concentrate all in one single gridcell, whereas smaller and larger particles can escape of the vortex again.

If we include particle feedback, then we get a different picture, except for $St = 20.0$ particles. Those large particles are hardly affected by the vortex structure and no mentionable particle concentration is reached. Therefore the gas and with that the vortex is not affected by the large particles.

For all the other particle sizes we see a high concentration of particles inside the vortex. $St = 1.0$ particles concentrate very locally in the center of the vortex, which leads to steep vorticity gradients that disrupt the vortex. This weakens the localizing effect the vortices have on the particles. With decreasing particle density the vortex can be re-established and the cycle repeats. The dust-to-gas ratio can be locally increased up to $\varepsilon \approx 80$. More than 80% of the dust is concentrated to more than $\varepsilon = 1.0$.

Smaller particles are not concentrated locally that strongly inside of the vortex. Instead they are spread out over the entire vortex and take part in the streaming instability (Youdin and Goodman, 2005; Youdin and Johansen, 2007). This instability only shows up when particle feedback is important, i.e. when $\varepsilon > 1.0$. However we see a significant change especially for $St = 0.05$ particles even when only 2.13% of the entire mass has reached $\varepsilon > 1.0$. The maximum dust-to-gas ratio reached are $\varepsilon \approx 3.0$ for $St = 0.05$ and $\varepsilon \approx 1.0$ $St = 0.01$.

Although the particle concentrations achieved are very different for the different particle sizes, the overall mass of particles accumulated in a vortex is roughly the same. Around 90% of the entire dust content is swept up by the vortex.

Since not all particles will be of the same size as assumed in the first simulations we also conducted simulations with lower initial dust-to-gas ratios. We see that although the initial dust-to-gas ratio ε_0 is a factor 10 or 100 lower, the

locally reached dust-to-gas ratio is still of the same order of magnitude. The particle concentration is much stronger.

The collisional velocities of the particles show the expected trend, with highest velocities for $St = 1.0$ particles and lower velocities for larger and smaller particles. Compared to analytical models based on Kolmogorov turbulence, the collisional velocities we measure are one order of magnitude lower.

We conclude that baroclinic vortices are a feasible mechanism for accumulating particles. The concentrations achieved are, depending on particle size, a factor 100 to 10 000 higher than the initial value. Even if there is only very little dust present these high overdensities can be reached. Streaming instability additionally enhances the dust concentration. Yet, depending on disk model, the achieved dust densities remain 1 to 2 orders of magnitude lower than the Roche density. Still, to make reliable predictions on whether these effects really occur in protoplanetary accretion disks 3 dimensional studies have to be conducted. Then, sedimentation can produce even larger particle densities, which may finally be large enough to trigger gravitational collapse.

Chapter 5

3D Simulations

5.1 Introduction

In chapters 3 and 4 we only conducted 2 dimensional simulations. To better cover the physics in a protoplanetary accretion disk we now move to 3 dimensions. 3D unstratified studies for the baroclinic instability without particles have already been conducted by Lyra and Klahr (2011) and Lesur and Papaloizou (2010). Naturally, we should extend these studies in form of 3 dimensional vertically stratified simulations. However, the conversion from an unstratified to stratified model require some changes in the PENCIL CODE, like including vertical pressure stratification and vertical shear. Therefore we restrict ourselves to the unstratified model for the gas.

We will only briefly address the points of the stability of vortices, strength of angular momentum transport and amplification rate of the vortices. Our results will then be compared to the models of Lesur and Papaloizou (2010) and Lyra and Klahr (2011).

The main focus of this chapter will be on particle concentration, for which we do include vertical stratification. The fact that we use stratification for the particles but not for the gas can be justified posteriori because the observed particle scale-height is much smaller than the theoretical gas scale-height ($H_\mathrm{d} \ll H_\mathrm{g}$), so the vertical gas gravity has hardly any effect on the dust particles. As we will see, stratification dramatically changes the result of our 2 dimensional models, since particles undergo vertical motion and are subject to vertical stirring. Another important factor is how the particles affect the vortex structure, which we already saw in our 2D simulations, most strongly for $St = 1.0$. Here, three different outcomes are possible:

1. The vortex column is stable and particles accumulate inside the column.

2. The entire vortex column is destroyed by the particles. Particles settle to the mid-plane with no mentionable difference to non-turbulent runs. No baroclinic vortex can be established anymore, because it will be disrupted by the particles.

3. The particles destroy the vortex column in a small area around the mid-plane, but do not affect the the upper and lower parts of the vortex. The question is then how the remaining vortex will affect the particles in the mid-plane, and if the remaining vortex is strong enough to re-establish itself in the mid-plane.

Of course the results strongly depend on the particle size.

First we will introduce the new physics that are needed for 3 dimensional estimates. The numerical setup will be discussed afterwards. In section 5.4 we will analyze simulations without particles. We add particles in section 5.5, and discuss our results.

5.2 Physical Background

Besides the possibility of vertical gas motion, there are no new physical effects that occur. We already know from Lesur and Papaloizou (2010) and Lyra and Klahr (2011) that the elliptical instability occurs in 3 dimensional vortices. We will discuss this in the results section of this chapter.

For the particles however, there are additional accelerations acting on the particles in vertical direction: vertical gravity $g_z = -\Omega^2 z$ and vertical drag-acceleration $a_{s,z} = \tau_s^{-1}(u_z - v_z)$. Combined these cause the particles to settle to the mid-plane. Since small particles couple more tightly to the gas than large particles, they will take longer to settle. Whereas larger particles are damped less by the gas due to the smaller coupling and therefore settle much faster.

We birefly discuss the reduced equation of motion for particles, where we have assumed that $u_z \approx 0.0$ for different particle size regimes. For small particles we can assume that particles settle with a constant velocity so that $\partial_t v_z \approx 0$. This leads to

$$\partial_t z = -\tau_s \Omega^2 z \tag{5.1}$$

and

$$z = z_0 e^{-t\tau_s\Omega^2}. \tag{5.2}$$

Here particles will approach the mid-plane exponentially but never reach them. For particles with $St \gg 1.0$ the term $\tau_s^{-1} v_z$ is negligible and the equation of motion reduces to

$$\partial_t v_z = -\Omega^2 z \tag{5.3}$$

where

$$z = \cos(\Omega t) \tag{5.4}$$

is one solution. Very heavy particles will oscillate around the mid-plane, never settling permanently. In a real protoplanetary disk there are additional effects acting on the particles that will change this pure mathematical picture.

The sedimentation time-scale t_s for small particles can be deduced from equation (5.2). After a time $t_s = (\Omega St)^{-1}$ a particle will have sedimented by a factor e of its original height. For our two particles sizes this corresponds to $t_s = 0.16$ orbital periods for $St = 1.0$ particles and $t_s = 3.18$ orbital periods for $St = 0.05$ particles.

It is possible for particles to grow through coagulation while they settle. Since this is not relevant for our studies, because the growth times are too long, and also was not included in our models we just want to refer to the literature, e.g. Dullemond and Dominik (2005).

The vertical settling is opposed by turbulent diffusive motions, which spreads particles vertically. A steady state advective-diffusion equation can be derived (Dubrulle et al., 1995; Fromang and Papaloizou, 2006), under the assumption of a vertically constant τ_s

$$\frac{\partial \rho_\mathrm{d}}{\partial t} = D \frac{\partial}{\partial z}\left[\rho_\mathrm{g} \frac{\partial}{\partial z}\left(\frac{\rho_\mathrm{d}}{\rho_\mathrm{g}}\right)\right] + \frac{\partial}{\partial z}\left(\Omega^2 \tau_s \rho_\mathrm{d} z\right), \tag{5.5}$$

where D is the diffusion constant. Integrating this, we arrive at a Gaussian particle distribution with particle scale-height

$$H_\mathrm{d} = \sqrt{\frac{D}{\Omega^2 \tau_s}}. \tag{5.6}$$

Furthermore, if we assume that $D \sim \nu$ and that this is the same viscosity as in the α-prescription we get

$$H_\mathrm{d} = H\sqrt{\frac{\alpha}{St}}, \tag{5.7}$$

which is equation is only valid when $\alpha < St$.

However the assumption that $D \sim \nu$ is not necessarily justified. There is no a priori reason why the vertical diffusive particle transport should happen with the same strength as the radial turbulent angular momentum transport. Yet, since both are a form of diffusive transport, we can take the same approach for the diffusion coefficient as for the α-prescription (Johansen et al., 2006b)

$$D = \frac{\delta c_s^2}{\Omega}, \tag{5.8}$$

Table 5.1. Simulation setup

run	St	$\rho_{\mathrm{d},0}/\rho_{\mathrm{g},0}$	feed-back	β
3DG	-	-	-	2.0
3DF05nt	0.05	1 : 100	yes	0.0
3DNF05	0.05	1 : 100	no	2.0
3DF05	0.05	1 : 100	yes	2.0
3DF05E-3	0.05	1 : 1 000	yes	2.0
3DF05E-4	0.05	1 : 10 000	yes	2.0
3DNF1	1.0	1 : 100	no	2.0
3DF1	1.0	1 : 100	yes	2.0
3DF1E-3	1.0	1 : 1 000	yes	2.0
3DF1E-4	1.0	1 : 10 000	yes	2.0

where δ is an equivalent to the α parameter. The ratio of D and ν is expressed via the dimensionless vertical Schmidt number

$$Sc_z = \frac{\nu}{D} = \frac{\alpha}{\delta}. \tag{5.9}$$

A proper deviation for the particle scale height then yields

$$H_{\mathrm{d}} = H\sqrt{\frac{\alpha}{St\,Sc_z}}. \tag{5.10}$$

Equation (5.7) is the special case for $Sc_z = 1.0$, i.e. so if radial turbulent angular momentum transport and vertical particle diffusion are of the same strength.

5.3 Numerical Setup

5.3.1 Gas Setup

Since we do not include vertical gravity for the gas simulations, there is little change in the numerical setup. The z-component of the velocity is now calculated and the initial perturbation in density is extended to include the excitation of vertical modes. It now looks like

$$\rho' = \rho_0 C e^{-(x/2\sigma)^2} \times \sum_{i=-k_x}^{k_x} \sum_{j=0}^{k_y} \sum_{k=-k_z}^{k_z} \sin\left\{2\pi\left\{i\frac{x}{L_x} + j\frac{y}{L_y} + k\frac{z}{L_z} = \phi_{ijk}\right\}\right\}. \tag{5.11}$$

However, we choose $k_z = 0$ which means that no vertical modes are excited, but radial and azimuthal modes are excited in all layers of the box. Additionally we add noise to the density.

The physical size of our box is the same in radial ($\pm 2\,H$) and azimuthal [$0\,H - 16\,H$] direction as in the the 2D runs in chapters 3 and 4. We extend to $\pm 1\,H$ in the vertical direction. This is a compromise between adequately large physical domain to see the elliptical instability, but not high enough resolution to resolve all modes that contribute to the streaming instability. The vertical resolution is the same as in radial direction. We restrict ourselves to an entropy gradient of $\beta = 2.0$, since we saw in chapter 3 that the main difference between $\beta = 2.0$ and lower entropy gradients was the evolution time. The size of the vortices and strength of relevant parameters such as α-stresses only depends weakly on β. For $\beta = 2.0$ a resolution of $256 \times 256 \times 128$ is still feasible. This gives us the advantage of fast evolution time combined with lower resolution. Of course as more time becomes available, comparison studies with higher resolution and lower β should be conducted.

5.3.2 Particle Setup

For the particles, we add the vertical equation of motion. We also include linear vertical gravity $g_z = -\Omega_0^2 z$.

As in the 2D simulations we first evolve the gas alone for 200 local orbits before we put in particles. In these simulations, the particles are randomly distributed in the $x - y$ plane as before, but follow a Gaussian profile in the vertical direction

$$\rho_{\mathrm{d}}(z) = C_d e^{-0.5\left(\frac{z}{\sigma_{\mathrm{d}}}\right)^2}, \tag{5.12}$$

where ρ_{d} is the dust density, C_d a normalization constant and σ_{d} gives the height of the initial distribution. We set $\sigma_{\mathrm{d}} = 0.01$, which gives a well settled profile. This choice speeds up the initial relaxation.

Like in the 2D flat simulations we want to have about 4-5 super-particles per gridcell initially to avoid numerical effects. Most of the particles will settle into the mid-plane anyways, so we do not consider all vertical gridcells. Therefore we only need to take into account ± 10 gridcells around the mid-plane, leading to a particle count of 7 000 000.

For our setup, we will see that $\alpha = 10^{-3}$. If we assume for now that the Schmidt number for our system is 1.0 then the particle scale height is $H_{\mathrm{d}}\,(St = 0.05) = 0.01$ and $H_{\mathrm{d}}\,(St = 1.0) = 0.003$, thus it is only resolved by 6 or 2 gridcells respectively. We will test this assumption later in this chapter. While a higher resolution would be better, it is beyond our curruent computational resources.

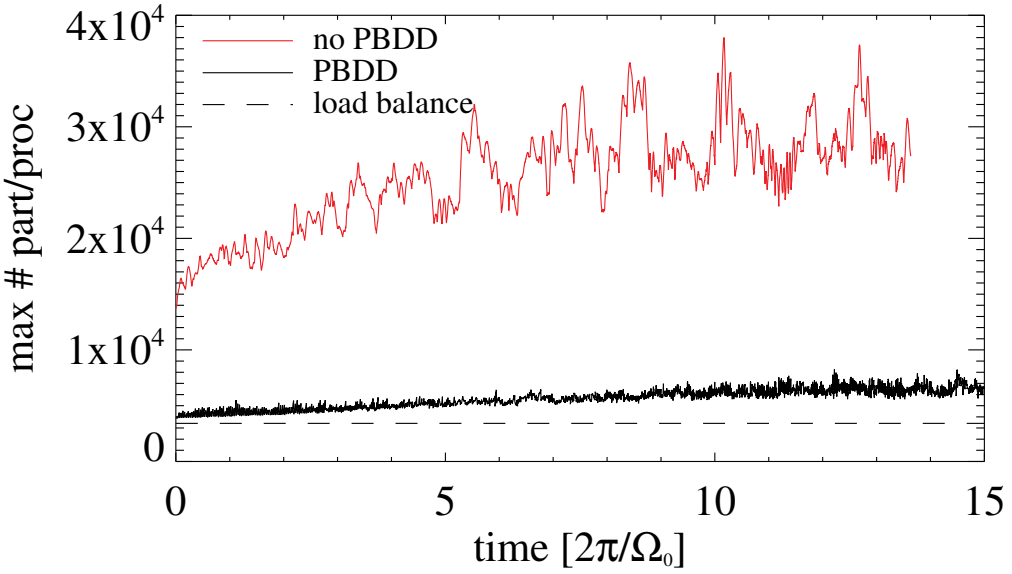

Figure 5.1 The maximum number of particles per processor at a certain time with *Particle Block Domain Decomposition* as described in Johansen et al. (2011) (PBDD, black solid line) and without PBDD (red solid line). The black dashed line indicates perfect load balance. There is still a deviation from perfect load balance even with the PBDD, which grows over time; but this algorithm is less time consuming than without the PBDD. The speed-up is roughly a factor of 6.

Particle feedback onto the gas is included for all simulations except for comparison simulations. The entropy gradient is set to $\beta = 2.0$. We restrict ourself to two particle sizes, $St = 1.0$ for intermediately coupled particles and $St = 0.05$ for strongly coupled particles. We set the initial dust-to-gas ratio to $\varepsilon_0 = 0.01$. Additionally, we perform runs with $\varepsilon_0 = 0.001$ and $\varepsilon_0 = 0.0001$. We also perform one simulation with $\beta = 0.0$ for $St = 0.05$. This run serves as a comparison run without turbulence. All setups are listed in table 5.1.

The standard parallel computing scheme provides bad load balancing for this kind of problem. Since most of the particles settle into the mid-plane, the processors responsible for the mid-plane have to do all the particle calculations, while processors responsible for the upper and lower parts of the disk will be idle as long as the particle calculation is conducted. For this reason Johansen et al. (2011) have developed a new scheme called *Particle Block Domain Decomposition* and implemented it into the PENCIL CODE. Here the processor structure is sub-devided into smaller boxes called bricks. These bricks contain particles. At every time-step the bricks are redistributed to other processors which now take over the particle calculation. All necessary informations, e.g.

gas velocities, are communicated to the receiving processor at every time-step. For a more detailed discussion of the algorithm see Johansen et al. (2011). As long as there is no extreme clumping, so that there are many particles in one brick, this will lead to a significant speed up compared to simulations without block decomposition (see figure 5.1).

5.4 Results: Gas Simulations

The evolution of the vortex in a 3D unstratified box is very similar to the 2 dimensional case. First, a number of small vortices emerge. These vortices are then amplified by the mechanism described in section 3.2 and also merge. See figure 5.2 for snapshots of the vorticity of our simulation.

At some point the vertical gas motion sets in and creates turbulent features in the vorticity structure (compare top and bottom panel of figure 5.3). After about 100 local orbits there is a steep increase in vertical gas velocity, yet it remains $3-2$ orders of magnitude lower than the radial and azimuthal velocity components (see figure 5.4). This is the same feature that Lyra and Klahr (2011) and also Lesur and Papaloizou (2009, 2010) identify as the elliptical instability. This parasitic instability affects 3D elliptical flows and tends to regulate them through a vortex stretching term. In principle 3D unstratified vortices are made up of many 2D vortices stacked on top of each other. If small vertical velocity perturbations appear then they can be amplified by the elliptical instability. Lesur and Papaloizou (2009) showed that the elliptical instability can lead to the disruption of 3 dimensional elliptical flows, but when they turned on baroclinic driving they saw that while the vortex does get slightly smaller, at some point a balance between the disruptive elliptical instability and driving baroclinc effects sets in. For a comprehensive review of this instability see Kerswell (2002). We come to the same conclusion as Lyra and Klahr (2011) and Lesur and Papaloizou (2010): the elliptical instability is present in the vortex core. However, due to the continuous vorticity production by the baroclinic vortex amplification the vortex is not destroyed.

The angular momentum transport we find in 3D is slightly lower than the values for $\beta = 2.0$ in 2 dimensional simulations but still in the same range (figure 5.5). Again this agrees with Lyra and Klahr (2011).

We want to stress here that this still can not be taken as face value for the angular momentum transport in a physical accretion disk. For that our studies would need to be stratified, and have higher resolution and physical parameters for the Brunt-Väisälä frequency and the cooling processes.

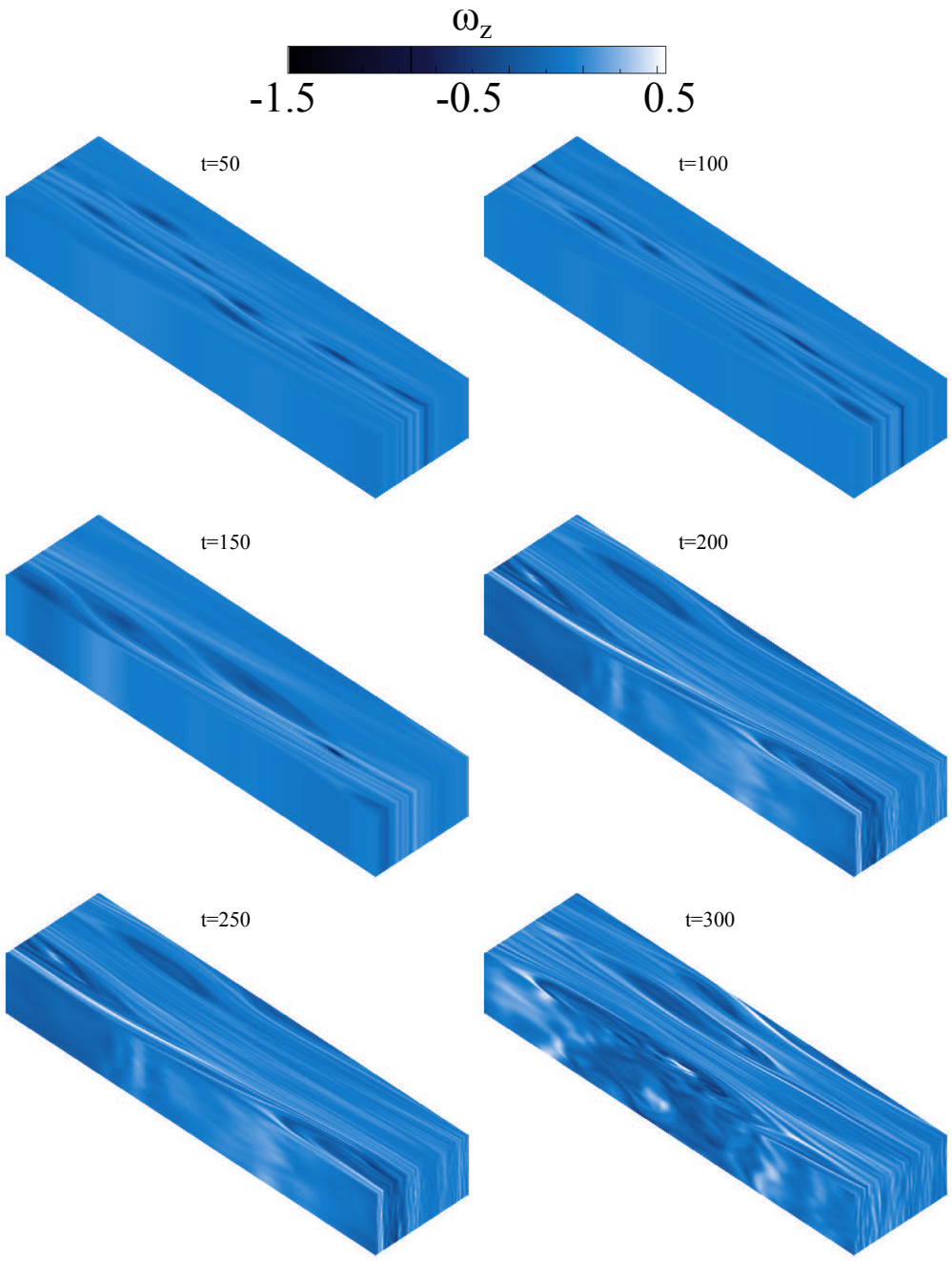

Figure 5.2 Vertical vorticity of unstratified gas in a 3 dimensional box at different times. The many initial small vortices merge over time and become amplified.

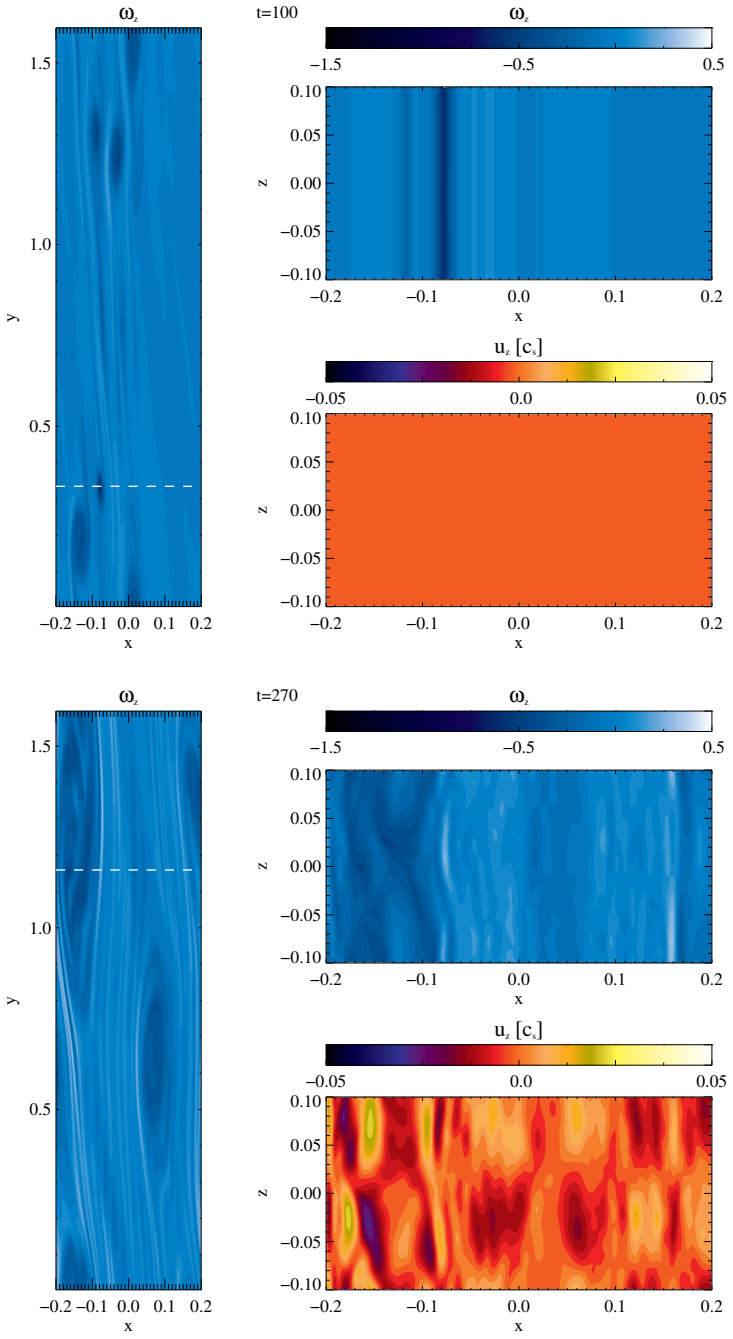

Figure 5.3 Shown are the vertical component of the vorticity (ω_z) in the mid-plane (left panel) and a vertical cut through the disk at the azimuthal location of maximum negative vorticity (indicated by the dashed line). Also shown is the vertical velocity component. There still is a smooth vortical structure after 100 local orbits (top panel). After 275 local orbits (bottom panel) there now is turbulent motion inside the vortex, which is also visible in the vertical velocity. This is an indication for the elliptical instability.

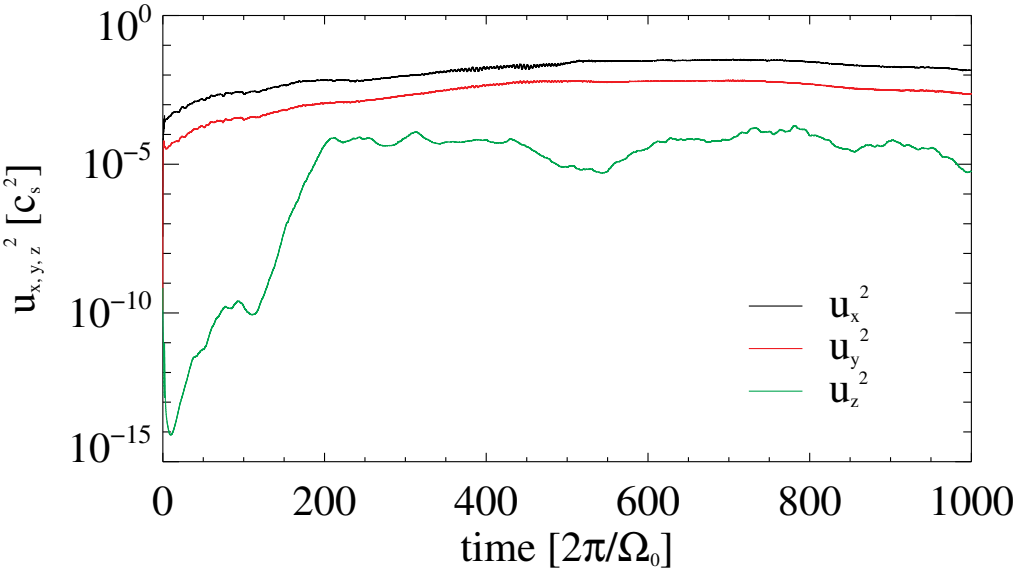

Figure 5.4 Gas velocity components averaged over the entire box. As the elliptical instability sets in, the vertical velocity component (green line) increases steeply, yet stays well below the azimuthal and radial components.

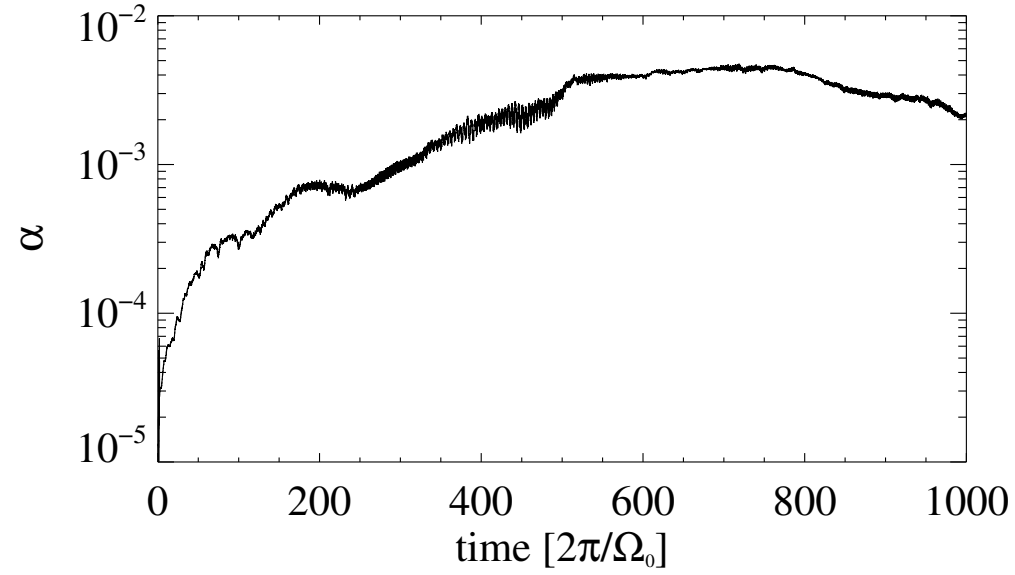

Figure 5.5 α-values averaged over the entire box. The strength of the angular momentum transport in 3D unstratified simulations agrees with our 2D results.

Table 5.2. Diffusion coefficient and Schmidt number

run	St	H_d	D	δ	α	Sc_z
3DF05nt	0.05	1.20×10^{-3}	7.21×10^{-8}	7.21×10^{-6}	1.00×10^{-4}	13.87
3DNF05	0.05	2.57×10^{-3}	3.31×10^{-7}	3.31×10^{-5}	1.12×10^{-3}	33.83
3DF05	0.05	2.23×10^{-3}	2.49×10^{-7}	2.49×10^{-5}	6.65×10^{-4}	26.7
3DNF1	1.0	9.92×10^{-4}	9.84×10^{-7}	9.84×10^{-5}	9.36×10^{-4}	9.51
3DF1	1.0	8.49×10^{-4}	7.20×10^{-7}	7.20×10^{-5}	2.64×10^{-4}	3.72

5.5 Results: Particles Simulations

5.5.1 Particle Scale Height and Diffusion Coefficient

In our first estimate of H_d we assumed $Sc_z = 1.0$, but in the last section we saw that the gas vertical velocity, which affects the particle vertical diffusion, is much smaller than its radial and azimuthal component (see figure 5.4). This indicates that the assumption $Sc_z = 1.0$ is clearly wrong. To test this we fit a Gaussian profile to our vertical particle density distribution. This is shown in figure 5.6 for $St = 0.05$ and $St = 1.0$ particles with feedback on the gas (simulations 3DF05 and 3DF1). The solid lines show the radial and azimuthal average of ρ_d for different orbital times. The dashed line shows the Gaussian fit and H_d, the fitted particle scale height.

We fit the scale-height for all individual time steps after 10 orbital periods and take the average. For $St = 1.0$ enough sedimentation times have passed. However, for $St = 0.05$ particles t_s is 3.2 orbital periods and only about 3 t_s have passed. Which means that sedimentation is not finished when we start our average. Another problem is that the gaussian only fits the peak values of our distribution but not the flanks. We tried different fitting routines such as the Moffat-fit (Moffat, 1969) which is often used to fit point-spread-functions but it did not improve our results.

Therefore the derived Sc_z have to be viewed with care. The derived scale-heights also for other simulations can be seen in table 5.2. Using equation (5.7) we can now derive the diffusion coefficient and with measured α-values[9] we can also calculate the Schmidt numbers of the individual systems.

[9]Since for simulation 3DF05nt no turbulent angular momentum transport happens we set $\alpha = 10^{-4}$ which according to Johansen et al. (2006b) corresponds to the $\alpha-$values due to the streaming instability.

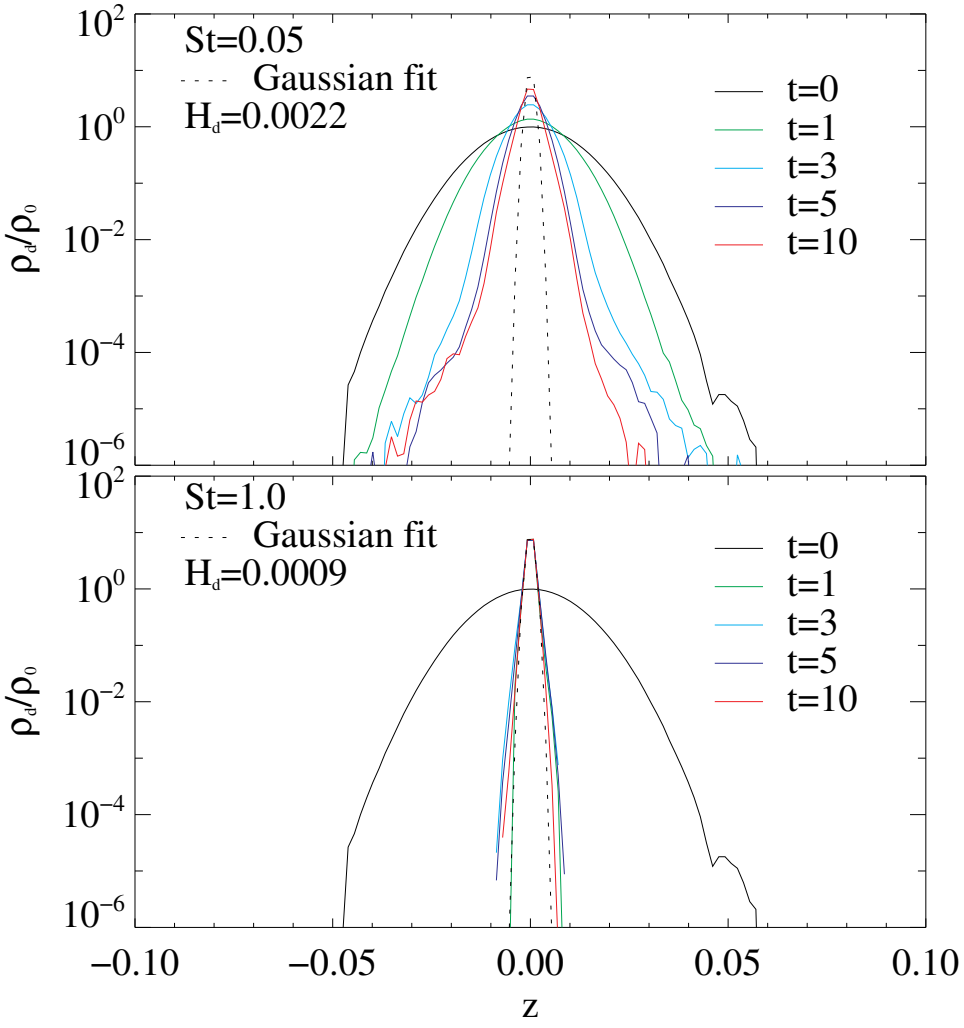

Figure 5.6 The solid lines show the initial azimuthally averaged vertical density profile and after 1, 3, 5 and 10 local orbits. The dotted line shows a Gaussian fit averaged over many orbits. Due to the low vertical resolution, only the central part of our density distribution is fitted well by a Gaussian profile. We lack a sufficient amount of data points on the flanks of the profile. Therefore our derived dust scale-height and with that diffusion constant and Schmidt numbers have to be viewed with care.

We see a range of Sc_z between 3 and more than 30. This clearly shows that the assumption $D \sim \nu$ is not applicable for baroclinic turbulence. For $St = 1.0$ particles, which have a smaller scale height than smaller particles, the Schmidt number is smaller. Johansen et al. (2006b) looked at turbulent diffusion in protoplanetary disks with vertical magnetic fields imposed. The Sc_z they find also differ from 1.0. Their average values are around 18.0, which is of the same order of magnitude as our values. With the data they obtained they were able to fit an empirical relation between α and Sc_z. The limited amount of data we have does not allow for a similar study.

5.5.2 Particle Accumulation

We first discuss the run without baroclinic driving. Here we did not put the particles into a developed gas simulation, but rather started with the initial perturbation as described in section 5.3.1. As expected the particles settle to the mid-plane, instantaneously triggering the streaming instability. Although we assumed an overall initial dust-to-gas ratio of $\varepsilon_0 = 0.01$, the initial dust-to-gas ratio in the mid-plane is already $\varepsilon = 1.0$ and increases even further as the sedimentation progresses. This early high concentration has two reasons. We initially assume $\varepsilon_0 = 0.01$ for the entire box so that the amount of dust in the simulations is $1/100$ of the entire gas mass. Because we use unstratified gas simulations we overestimate the amount of dust in the box. The amount of dust in a box is derived out of the gas density ρ_g which in a stratified case with a Gaussian gas density profile looks like

$$\rho_g = \frac{\Sigma_g}{\sqrt{2\pi}H}. \tag{5.13}$$

Yet, for our unstratified approach the gas density has the form

$$\rho_g = \frac{\Sigma_g}{H}. \tag{5.14}$$

Therefore the dust content is overestimated by a factor $\sqrt{2\pi}$ which rather corresponds to an an initial $\varepsilon_0 = 0.025$. As a result the dust-to-gas ratio in the mid-plane is already as high as $\varepsilon \approx 1.0$. This factor $\sqrt{2\pi}$ has to be taken into account when we compare our results to results of e.g Johansen et al. (2007) or Johansen et al. (2009). Our results for $\varepsilon_0 = 0.01$ correspond to their results with $\varepsilon_0 = 0.02$.

The maximum dust-to-gas ratio of the simulation with $St = 0.05$ particles and without baroclinic driving can be seen in 5.7 (red line). The other two lines in the plot show the maximum dust-to-gas ratios for the simulation with $\beta = 2.0$ and $St = 0.05$ (green line) and $St = 1.0$ particles (black line). We can already see that the maximum concentration for $St = 0.05$ is only a factor

of two higher than in the case without baroclinic driving. Although the dust-to-gas ratios are quite high, we expected much higher values when baroclinic feedback was included, compared to simulations without baroclinic driving.

Looking closer at the development of the dust density in these simulations, we see that, as expected, the particles settle to the mid-plane. During the first couple of orbits we see that the particles follow the vortex motion if any. There is a slight overdensity compared to the initial particle density in the vortex. But after only 3 orbits the particles start to perturb the vortices in the mid-plane via the streaming instability. Like in the 2D simulations, high particle densities create local perturbations of the velocity field visible as steep vorticity gradients. In the 2D simulations, the vorticity minima and maxima were between -1.0 and 1.0. Rarely and only for short times did lower/higher vorticity values occurr (see e.g. figure 4.4, where the high particle concentrations cause steep vorticity gradient in the center of the vortex). Here, with the vortex column at the mid-plane being completely disrupted, it is not as useful to talk about vorticity. See figures 5.10 and 5.8 for ω_z at the top of the box (left panel), in the mid-plane (middle panel) and the dust-to-gas ratio in the mid-plane for $St = 0.05$ particles.

The streaming instability is triggered in all our runs . Yet, we cannot be sure that we always resolve the fastest growing modes. The growth rates are a function of particle size and local dust-to-gas ratio. We can say that we reach an ε where the growth rate of the streaming instability is larger than the dynamical timescale, yet deeper investigations such as those performed by Youdin and Goodman (2005); Youdin and Johansen (2007) and Johansen and Youdin (2007) required higher resolution. It will be computationally expensive to properly simulate streaming at small scales while simultaneously generating large scale vortices. Since the aim of this thesis was to study the behavior of vortices we had to accept low resolution for the streaming instability.

Although the vortices in the mid-plane are heavily disrupted, the vortex column above and below the mid-plane is still present. Since there are no particles in the upper and lower areas of the box, there is no disruption. We expect these vortex columns to stay stable over a long time (see figure 5.10 left panel of figure 5.8). As we will discuss later in this chapter these vortex columns still have a minor influence on the particles.

The explanation for why we do not see a high increase of dust-to-gas ratio for simulations with baroclinic vortices compared to simulations without baroclinic driving lies in the disruption of vortices in the mid-plane. To test whether there is a strong dust concentration when vortices are stable, and also to account for the fact that not all particles will be of the same size we perform simulations with lower initial dust-to-gas ratios, $\varepsilon_0 = 10^{-3}$ and $\varepsilon_0 = 10^{-4}$. Again, when these values are compared to other works that use stratified gas simulations the have to be transferred to $\varepsilon_0 = 2.5 \times 10^{-3}$ and $\varepsilon_0 = 2.5 \times 10^{-4}$.

Table 5.3. Maximum dust-to-gas ratio at end of simulation

run	St	$\rho_{d,0}/\rho_{g,0}$	t_{end}	ε_{max}
3DF05nt	0.05	1 : 100	43.4	41.6
3DNF05	0.05	1 : 100	40.7	3540.0
3DF05	0.05	1 : 100	38.2	111.2
3DF05E-3	0.05	1 : 1 000	25.3	8.7
3DF05E-4	0.05	1 : 10 000	20.0	2.1
3DNF1	1.0	1 : 100	22.4	15630.0
3DF1	1.0	1 : 100	22.8	945.4
3DF1E-3	1.0	1 : 1 000	7.7	227.7
3DF1E-4	1.0	1 : 10 000	9.7	34.2

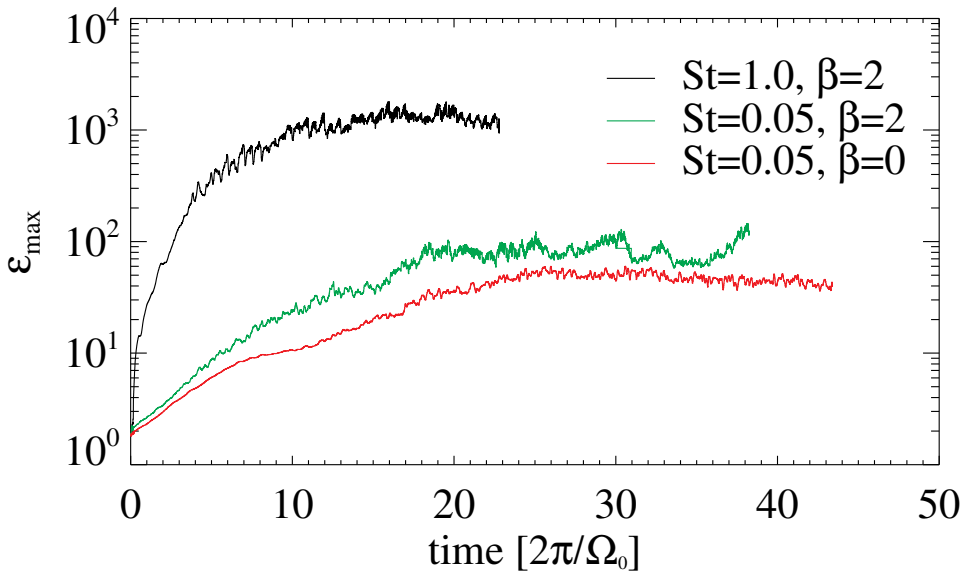

Figure 5.7 Maximum dust-to-gas ratio for simulations with $St = 1.0$ (black line) and $St = 0.05$ (green and red line) particles. $\beta = 0$ indicates that no baroclinic feedback was included in the simulation. Although the high particle concentration in the simulations with baroclinic effects destroys the vortices where particles are located the maximum dust-to-gas ratio is higher than without baroclinic effects.

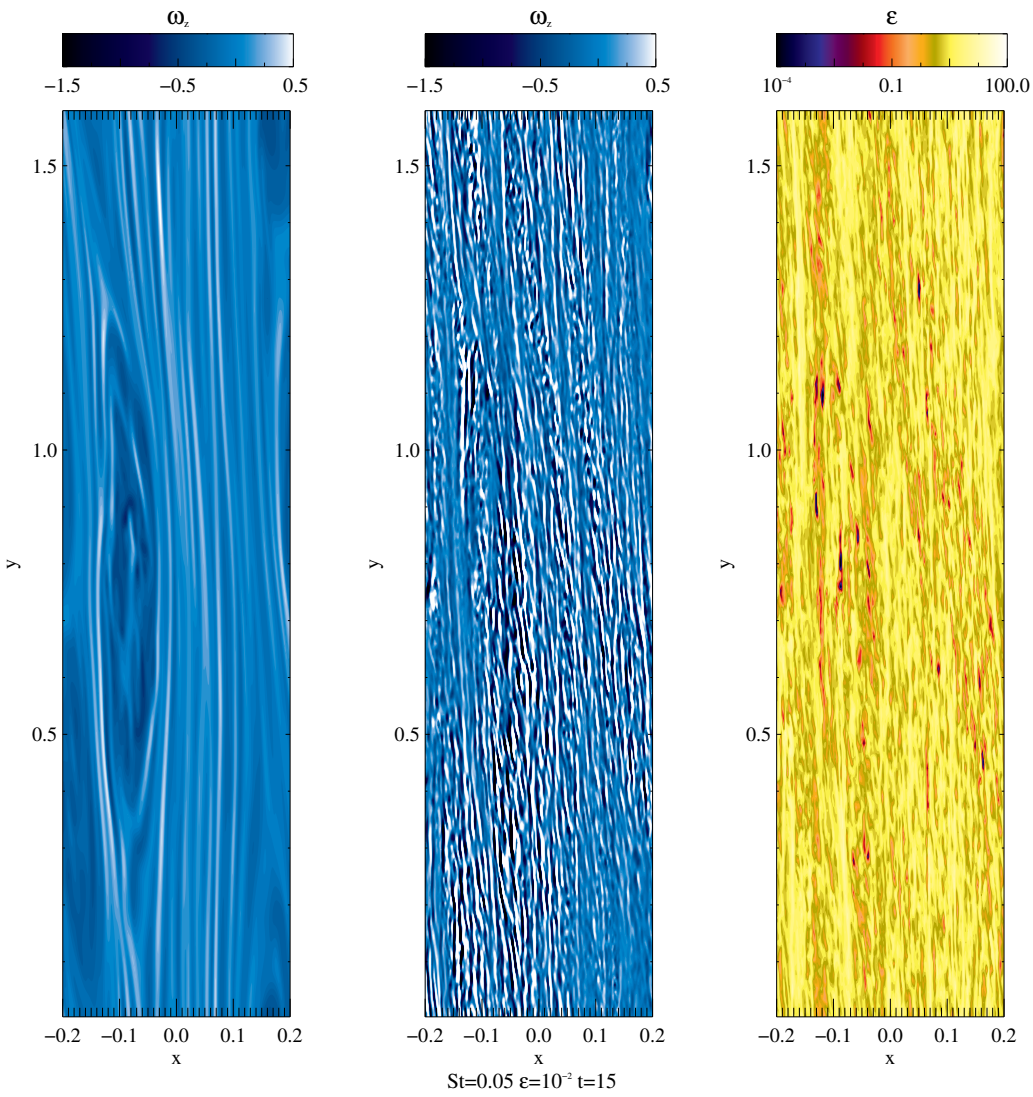

Figure 5.8 Vertical vorticity component ω_z at the top of the box (left) and in the mid-plane (middle) and dust-to-gas ratio ε (right) in the mid-plane for $St = 0.05$ particles and an $\varepsilon_0 = 10^{-2}$. There are no more large scale vortices in the mid-plane and the particles spread are out over the entire mid-plane. Since there was an initial particle accumulation inside the vortex before it was destroyed, there is a residual accumulation at the original vortex position. The maximum dust-to-gas-ratio in this snapshot is $\varepsilon = 31.7$.

Already for $\varepsilon_0 = 10^{-3}$ we see a different picture. The particles settle to the mid-plane, but the vortices there are no longer destroyed: the entire vortex column is a stable feature. Particles accumulate inside of the vortex, as we saw in the 2D simulations, and then migrate slowly with the vortices. Figures 5.8 and 5.9 show the different simulation outcomes for $St = 0.05$ particle with $\varepsilon_0 = 10^{-2}$ and $\varepsilon_0 = 10^{-4}$ after 15 local orbits. It is still too early to say something

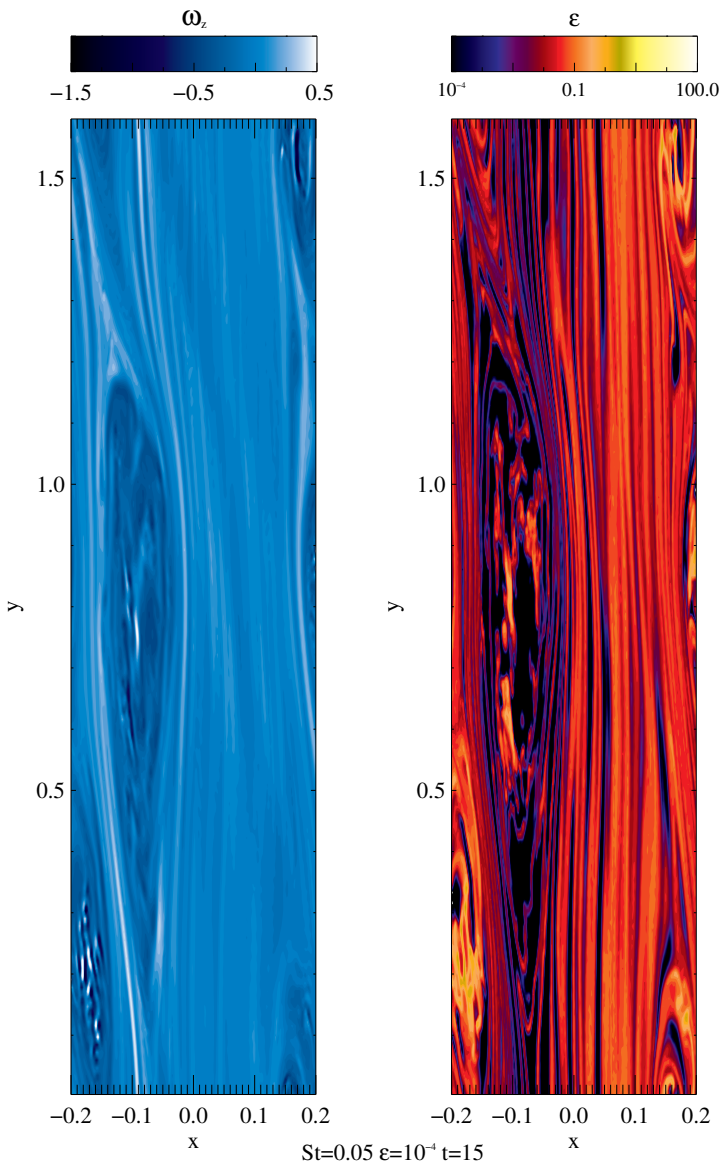

Figure 5.9 Vertical vorticity component ω_z and dust-to-gas ratio ε in the mid-plane for $St = 0.05$ particles and an $\varepsilon_0 = 10^{-4}$. In contrast to simulations with $\varepsilon_0 = 10^{-2}$ the vortices in the mid-plane are not destroyed and the particles accumulate inside of the two vortices. The maximum dust-to-gas-ratio reached in this snapshot is $\varepsilon = 2.2$ which is one order of magnitude lower than for $\varepsilon_0 = 10^{-2}$.

definitive about the final maximum dust-to-gas ratio of these simulations, but they appear to stay below the the ones reached with $\varepsilon_0 = 0.01$. table 5.3 figure 5.11 show the maximum values of ε. We see that in all simulations $\varepsilon > 1.0$ is reached and that streaming is triggered. The baroclinic vortices prove to be an efficient particle trap. When Johansen et al. (2009) studied particle clumping,

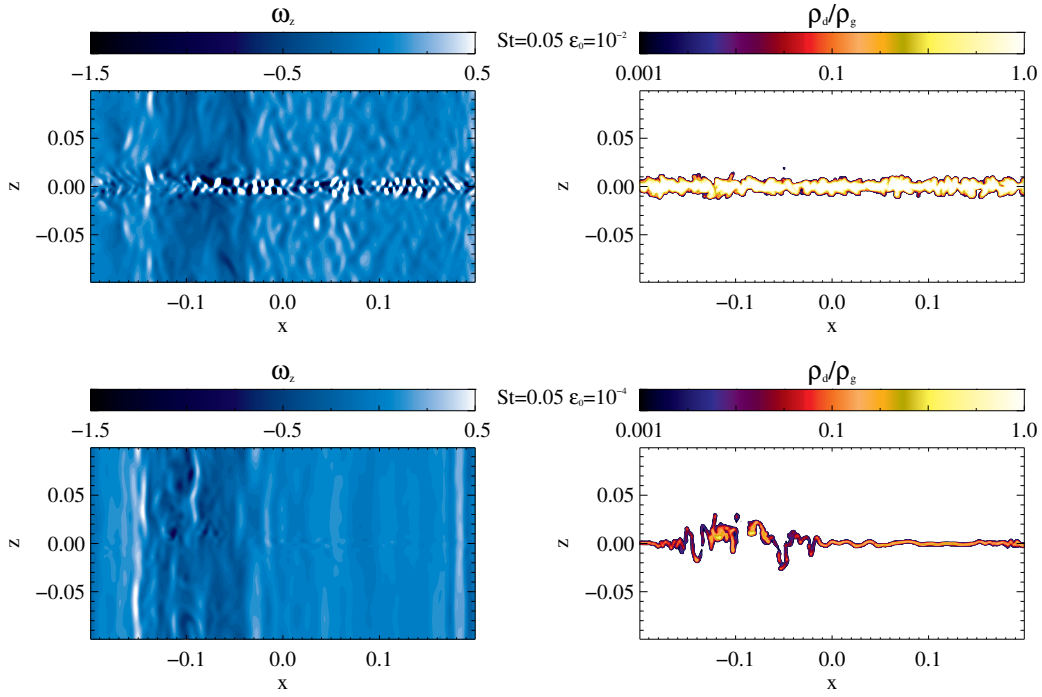

Figure 5.10 Vertical cut through the vortex after 15 local orbits for $St = 0.05$ particles and $\varepsilon_0 = 10^{-2}$ (top) and $\varepsilon_0 = 10^{-4}$ (bottom). Shown are the vertical component of vorticity ω_z (left) and the dust-to-gas ratio $\rho_\mathrm{d}/\rho_\mathrm{g}$ (right). For $\varepsilon_0 = 10^{-2}$ the vortex located around $x \sim -1H$ is strongly perturbed around the mid-plane. For lower ε_0 the vortex column remains stable.

they needed to increase their ε_0 to trigger streaming. Also the particle sizes they used to trigger streaming were larger than our smallest particles. With baroclinic vortices we can reach the same concentrations they reached with much smaller particle sizes, which according to Birnstiel et al. (2010, 2012), are the dominant particle species in protoplanetary disk. Also we find that an initial dust-to-gas ratio of 10^{-4} is sufficient to trigger the streaming instability.

Next we discuss the time evolution of our different simulations briefly. For this, we plot the particle surface density averaged over the azimuthal domain relative to its initial value as a function of time (bottom panel of figures 5.12 - 5.16) and also the vertical particle density relative to the gas density (top panel of figures 5.12 - 5.16) at a cut through the simulation domain at the location of the maximum particle density. Note that the colors on the plots are scaled in a way that features are distinguishable. The peak values are off the colorscale. We refer to table 5.3 for the maximum values of ε. In all simulations (except for the one without baroclinic driving) we see that there are bands of high particle concentrations that are slowly propagating radially inwards. The radial migration corresponds to the migration of the vortices. The wiggles in these bands show the epicyclic motion of the particles. This features are even visi-

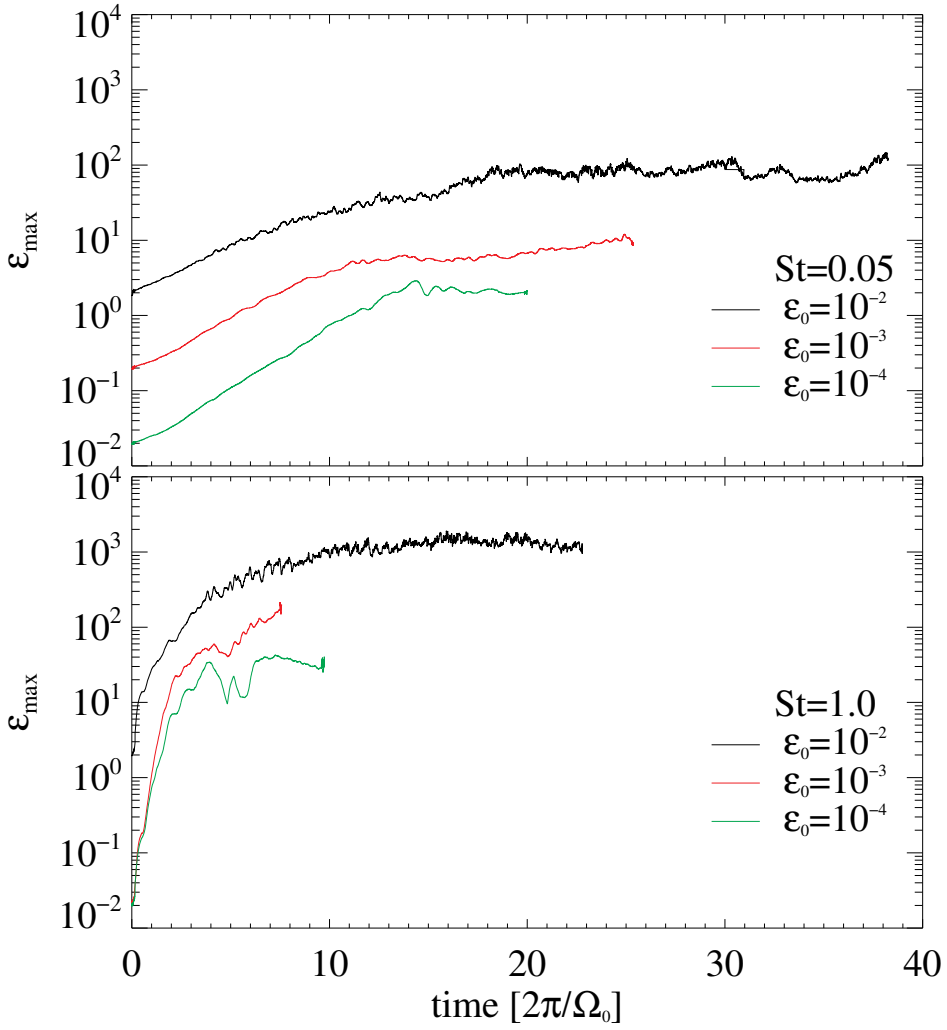

Figure 5.11 Maximum dust-to-gas ratio for simulations with $St = 0.05$ (to panel) and $St = 1.0$ (bottom panel) particles and different initial dust-to-gas ratios ε_0. While the concentration $c = \rho_d / \rho_{d,0}$ is the same for all ε_0 the achieved maximum dust-to-gas ratios for small ε_0 will remain below those of high ε_0.

ble in the simulations with $\varepsilon_0 = 0.01$, although we said that there is no more vortex in the mid-plane. It seems like the remaining vortex column still has an effect onto the particles.

As in the 2D simulations, the highest particle concentration are reached in simulations without feedback onto the gas (right column of figures 5.13 and 5.15). There is another interesting feature in the simulation without feedback for $St = 1.0$ particles. A band of high particle concentration radially drifts inwards much faster than the vortex migration (left column of figure 5.15). This dust concentration is not captured in a vortex and thus can move with the

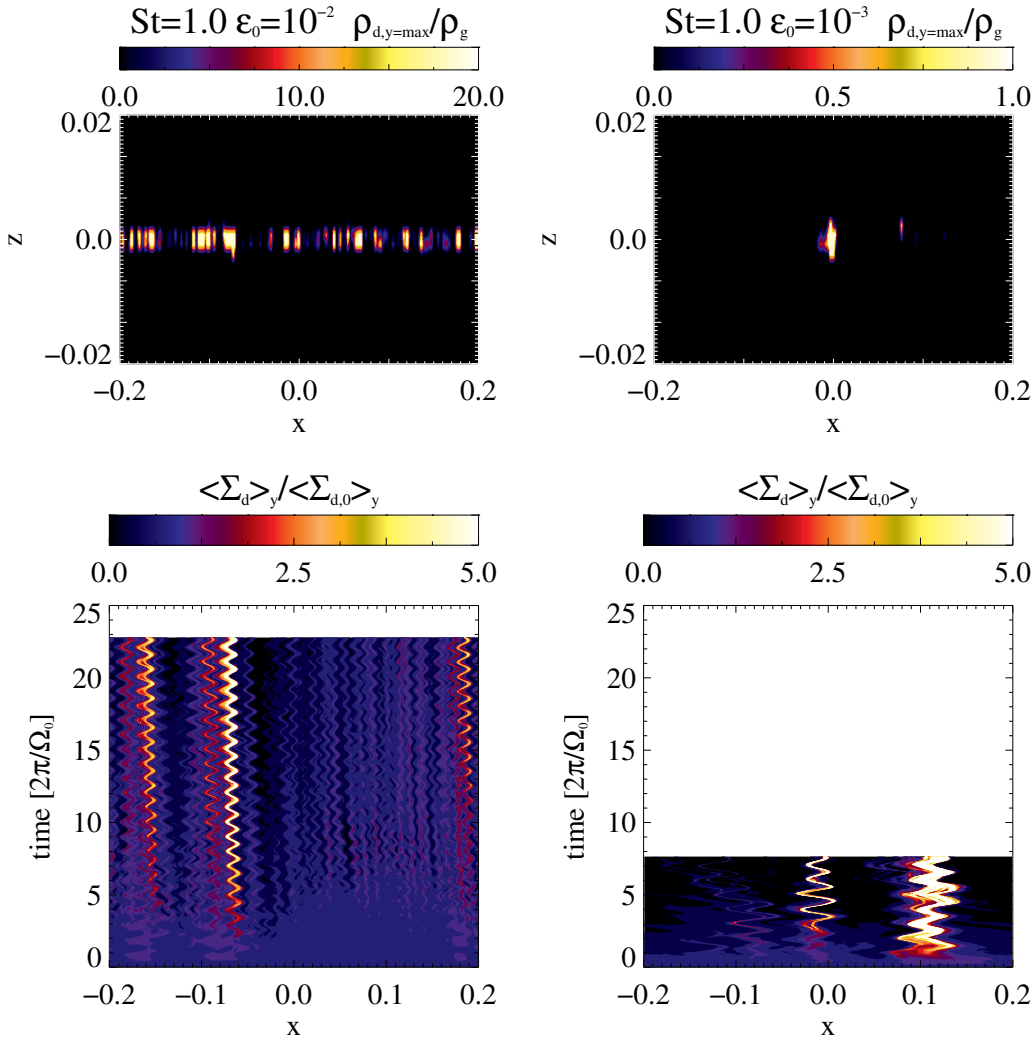

Figure 5.12 The top row shows the dust-to-gas ratio at an azimuthal cut through the box at the location of the highest dust-density. The bottom row shows the time development of the dust surface density Σ_d relative to its initial value $\Sigma_{d,0}$ and averaged over the entire azimuthal domain. On the left side we show the simulation of $St = 1.0$ particles with an $\varepsilon_0 = 10^{-2}$ and on the right side $St = 1.0$ particles with an $\varepsilon_0 = 10^{-3}$. The location of the particle concentration agrees with the location of the vortices. Although the vortex is destroyed for $\varepsilon_0 = 10^{-2}$, there remains a residual concentration at the vortex location. The particle concentration migrates inwards with the vortex (even in the case where the vortex in the mid-plane is destroyed). The small wiggles in the particle concentration correspond to epicyclic motion of the particles within the vortex.

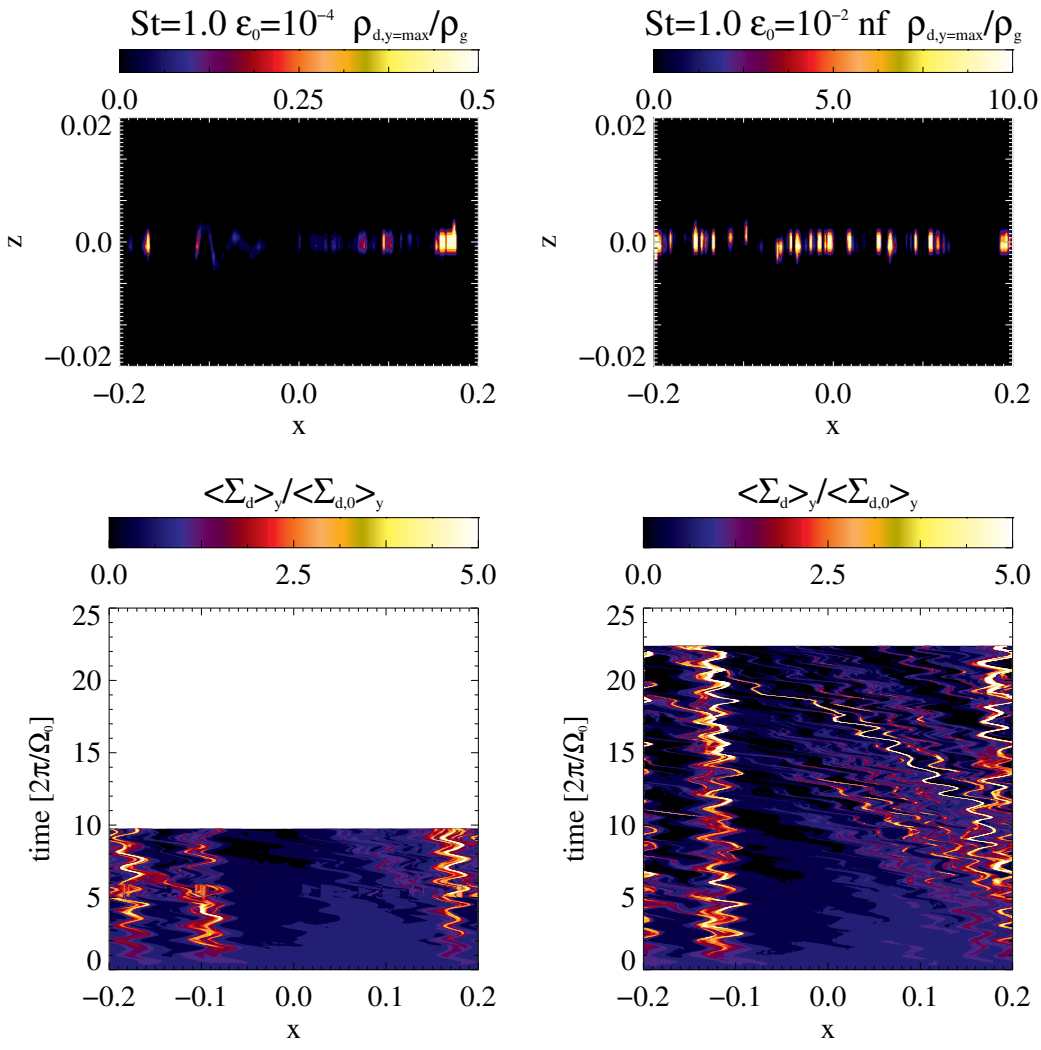

Figure 5.13 The top row shows the dust-to-gas ratio at an azimuthal cut through the box at the location of the highest dust-density. The bottom row shows the time development of the dust surface density Σ_d relative to its initial value $\Sigma_{d,0}$ and averaged over the entire azimuthal domain. On the left side we show the simulation of $St = 1.0$ particles with an $\varepsilon_0 = 10^{-4}$ with feedback, while on the right side we show $St = 1.0$ particles with an $\varepsilon_0 = 10^{-2}$ but without feedback onto the gas. The location of the particle concentration agrees with the location of the vortices. The small wiggles in the particle concentration correspond to epicyclic motion of the particles within the vortex.

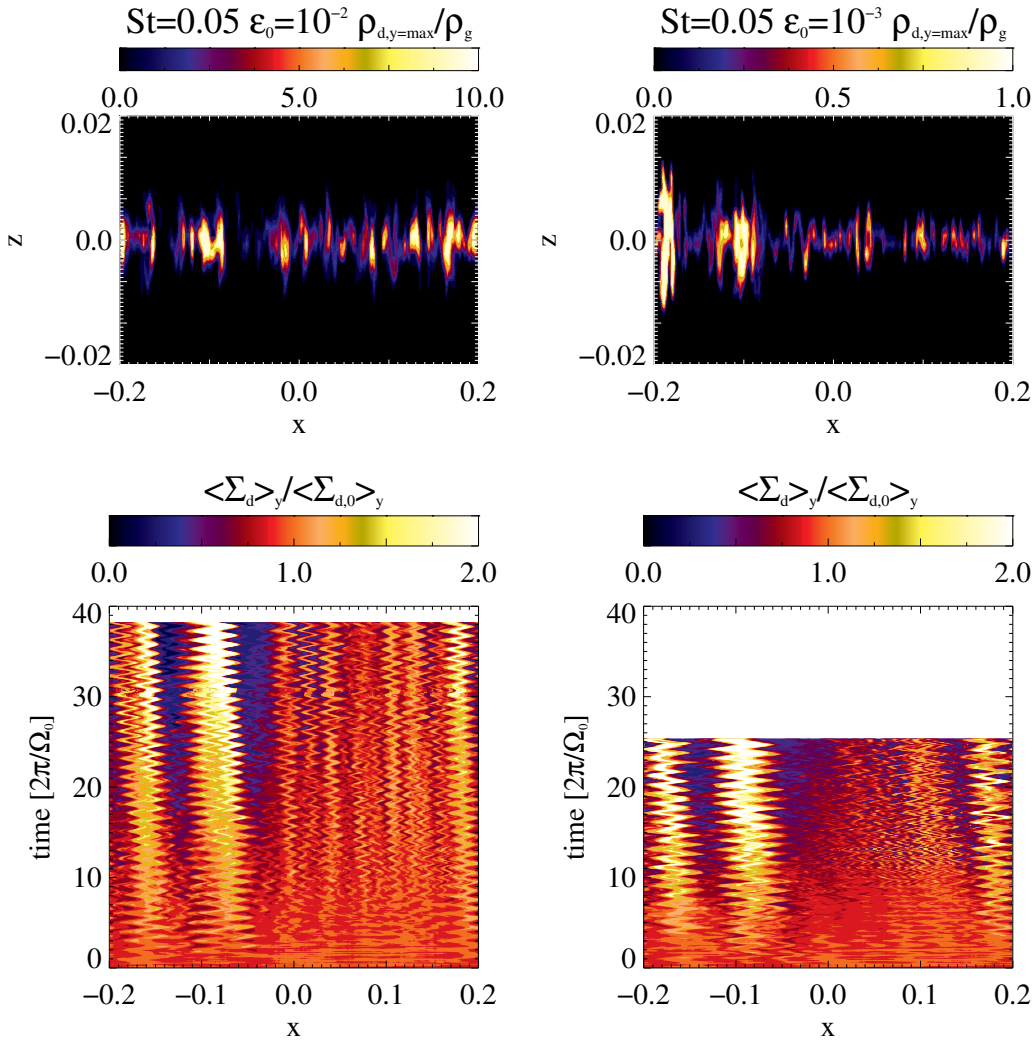

Figure 5.14 The top row shows the dust-to-gas ratio at an azimuthal cut through the box at the location of the highest dust-density. The bottom row shows the time development of the dust surface density Σ_d relative to its initial value $\Sigma_{d,0}$ and averaged over the entire azimuthal domain. On the left side we show the simulation of $St = 0.05$ particles with an $\varepsilon_0 = 10^{-2}$, and on the right side $St = 0.05$ particles with an $\varepsilon_0 = 10^{-3}$. The location of the particle concentration agrees with the location of the vortices. Although the vortex is destroyed for $\varepsilon_0 = 10^{-2}$ there there remains a residual concentration at the vortex location. The particle concentration migrates inwards with the vortex (even in the case where the vortex in the mid-plane is destroyed). The small wiggles in the particle concentration correspond to epicyclic motion of the particles within the vortex.

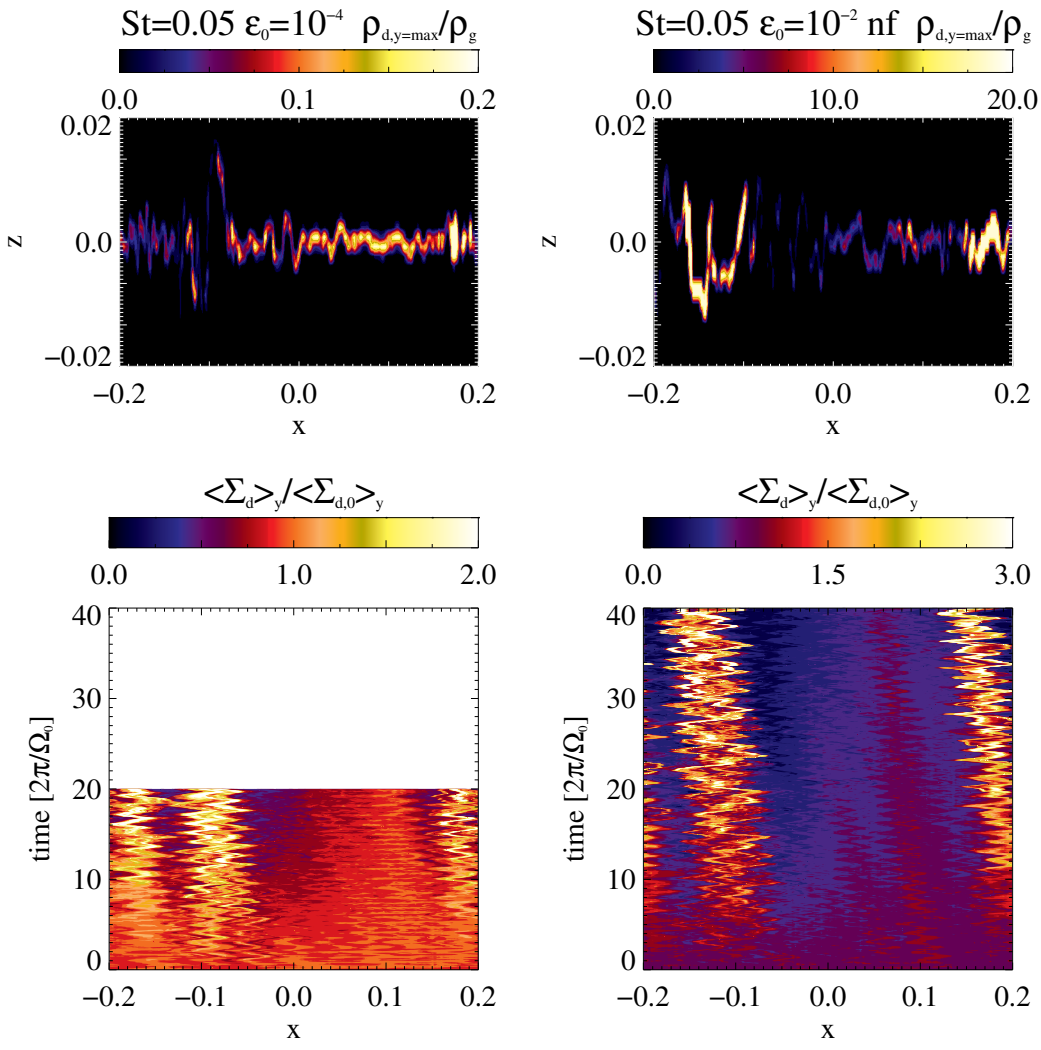

Figure 5.15 The top row shows the dust-to-gas ratio at an azimuthal cut through the box at the location of the highest dust-density. The bottom row shows the time development of the dust surface density Σ_d relative to its initial value $\Sigma_{d,0}$ and averaged over the entire azimuthal domain. On the left side we show the simulation of $St = 0.05$ particles with an $\varepsilon_0 = 10^{-4}$ with feedback, while on the right side we show $St = 0.05$ particles with an $\varepsilon_0 = 10^{-2}$ but without feedback onto the gas. The location of the particle concentration agrees with the location of the vortices. The small wiggles in the particle concentration correspond to epicyclic motion of the particles within the vortex.

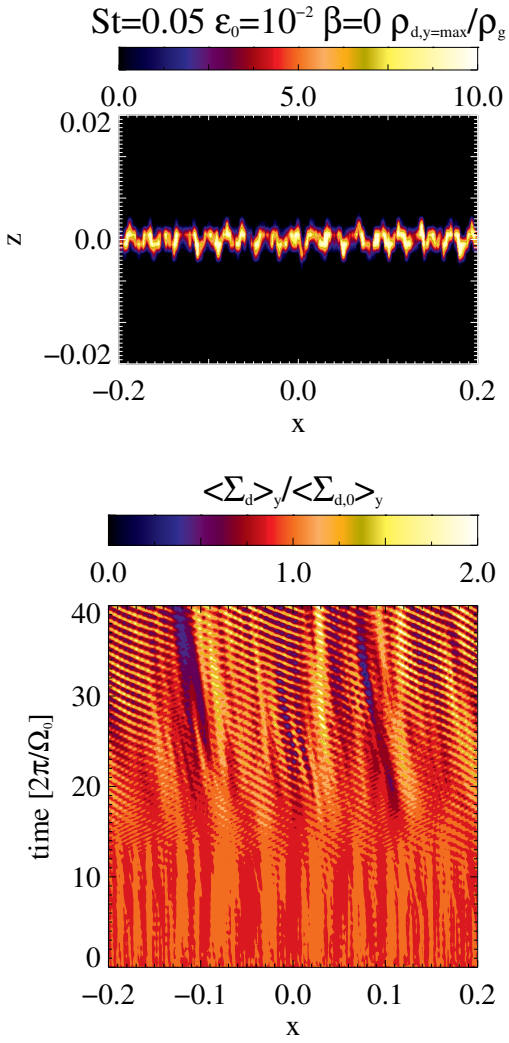

Figure 5.16 The top row shows the dust-to-gas ratio at an azimuthal cut through the box at the location of the highest dust-density. The bottom row shows the time development of the dust surface density Σ_d relative to its initial value $\Sigma_{d,0}$ and averaged over the entire azimuthal domain for $St = 0.05$ particles and baroclinic driving turned off. Since there are no vortices present and the strong localized concentrations seen in the previous figures do not appear here.

Table 5.4. Fraction of dust mass with $\varepsilon \geq 1.0$

run	fraction of M_d with $\varepsilon \geq 1.0$ (%)
3DF05	98.44
3DF05E-3	25.67
3DF05E-4	1.12
3DF1	98.73
3DF1E-3	26.41
3DF1E-4	14.46

normal particle drift velocity (see equation (4.9))which is much faster than the radial drift of vortices.

The vertical slices through the box also show the concentration of the particles at the location of the vortices. The reason why not all particle enhancements in the time development reappear in the vertical slices, e.g. right column of figure 5.12 at $x \sim 0.1$, is because the time-development is averaged over the azimuthal domain whereas the vertical cuts are not. It is quite possible that the maximum of the dust density is in one vortex, while the other vortex is at a different azimuthal position in the simulation with a lower, but still high, dust density. It would not be visible in the vertical cut.

The simulation without baroclinic driving (figure 5.16) shows different behavior than the simulations discussed above. Here particles are distributed more homogeneously, without a localized concentration. The radial drift of particles is faster than vortex migration in the other figures.

As in the 2D simulations we looked at how much dust accumulates at certain dust-to-gas ratios. The result is shown in figure 5.17 for our two particle sizes and three different ε_0. As expected, simulations with higher ε_0 also have more mass in large ε bins. Yet, even simulations with $\varepsilon_0 = 10^{-4}$ pass the limit of $\varepsilon \geq 1.0$, where the streaming instability sets in. While only 1% of $St = 0.05$ particles accumulate in regions with $\varepsilon \geq 1.0$ for $\varepsilon_0 = 10^{-4}$ this is an important step towards higher concentrations and may eventually lead to gravitational collapse. In Table 5.4 we show what mass fraction participates in the streaming.

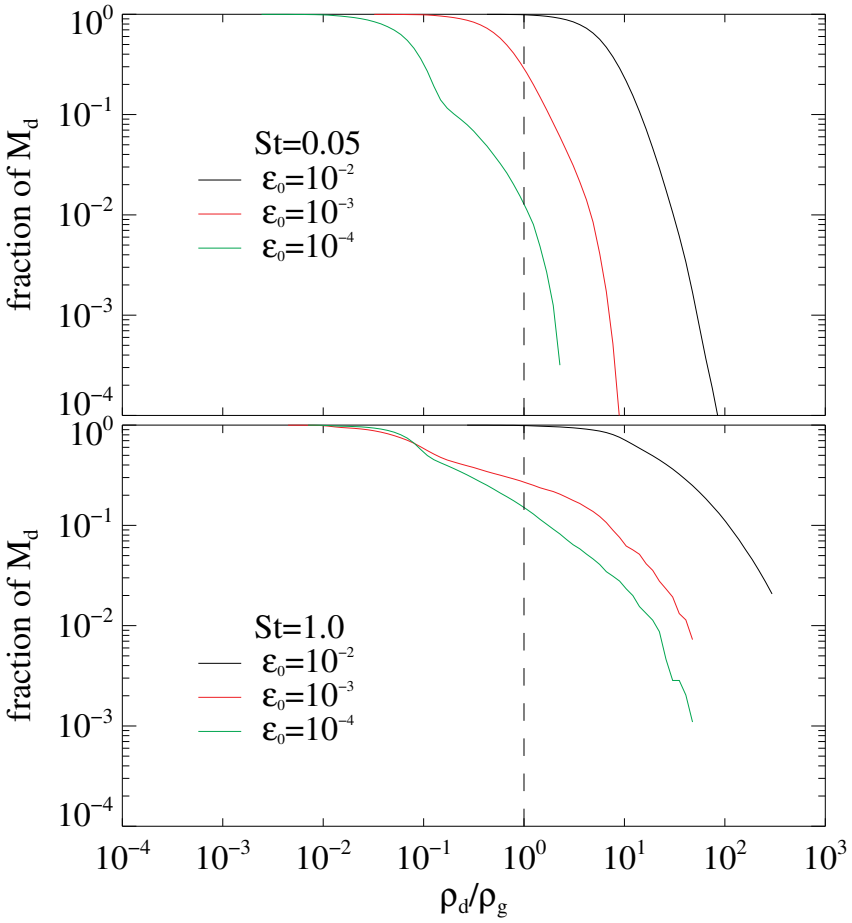

Figure 5.17 Fraction of total dust mass with an dust-to-gas ratio higher than a certain value for $St = 0.05$ and $St = 1.0$ particles and different initial dust-to-gas ratios. For all setups the limit for streaming instability ($\rho_d/\rho_g \geq 1.0$) is passed.

5.5.3 Possible Gravitational Collapse

In chapter 4 we saw that the particle densities we reached were lower than the Roche density. But due to sedimentation, in 3D runs the particle density is higher. We want to compare the achieved particle densities with the Roche density to see if now gravitational collapse would happen if we allowed for self-gravity. We use the same two disk models as in chapter 4. One with the MMSN with $\Sigma_g(5.2\,\mathrm{AU}) = 150\,\mathrm{g\,cm^{-3}}$ (case1 and 2) and a model with a heavy disk with $\Sigma_g(5.2\,\mathrm{AU}) = 800\,\mathrm{g\,cm^{-3}}$ (case 3 and 4). The Roche density at the two radii that we consider is $\rho_R(1\,\mathrm{AU}) = 2.83 \times 10^{-7}\,\mathrm{g\,cm^{-3}}$ (case 1 and 3) and $\rho_R(5.2\,\mathrm{AU}) = 2.01 \times 10^{-9}\,\mathrm{g\,cm^{-3}}$ (case 2 and 4).

Table 5.5. Dust density compared to Roche density

run	ε_{max}	ρ_R/ρ_g case1 (5.2 AU)	ρ_R/ρ_g case2 (1 AU)	ρ_R/ρ_g case3 (5.2 AU)	ρ_R/ρ_g case4 (1 AU)
3DF05	111.2	262	1607	**49**	301
3DF05E-3	8.7	262	1607	49	301
3DF05E-4	2.1	262	1607	49	301
3DF1	945.4	**262**	1607	**49**	**301**
3DF1E-3	227.7	262	1607	**49**	301
3DF1E-4	34.2	262	1607	49	301

In table 5.5 we show the maximum dust-to-gas ratios that were reached at the end of the computational time. The last four columns show the ratio of ρ_R and the gas density for the two disk profiles and the two radii. If ε_{max} exceeds this ratio, it means that the local dust-to-gas ration exceeds ρ_R at that radius, and the particle accumulation will collapse (indicated through bold number in table 5.5).

We see that at 1 AU the maximum dust densities are lower than the Roche density for all runs except for $St = 1.0$ particles with $\varepsilon_0 = 0.01$. Yet if we go to 5.2AU there are three more runs for the heavy disk model that exceed the critical ρ_R. This means that the clumps with these high overdensities should collapse and form bodies that are held together by their own gravity.

It is easier to form planetesimals at larger radii, because ρ_R falls off steeper than ρ_g. Therefore, the ratio ρ_R/ρ_g decreases radially, making it easier for dust densities to pass the critical density.

5.6 Conclusion

In this chapter we have performed 3 dimensional simulations of baroclinic vortices and particles in these vortices. The gas simulations were unstratified whereas we included vertical gravity for $St = 0.05$ and $St = 1.0$ particles.

In the pure gas simulations we saw that a stable baroclinic vortex develops. The strength of the angular momentum transport is only slightly the 2 dimensional values. After several orbits, the elliptical instability develops inside the vortex. Yet, due to continuos baroclinic vorticity production a stady state is established and the elliptical instability does not destroy the vortex. These result

agree with the findings of Lesur and Papaloizou (2010) and Lyra and Klahr (2011).

When we include particles with an initial dust-to-gas ratio of $\varepsilon_0 = 0.01$ and back-reaction we see that the vortex column in the mid-plane is destroyed after a very short time of concentration inside the vortex. We saw a similar picture in the 2 dimensional simulations for $St = 1.0$ particles when the local dust-to-gas ratio exceeded a value of ≈ 10. Due to the sedimentation of dust, this dust-to-gas ratio is reached after only a few orbital periods for both particle sizes. Unlike in the 2 dimensional simulations the vortex cannot be re-established since the dust densities remain constant and do not sink below the critical value. The vortex columns above and below the mid-plane still have an effect on the particle. The initial concentration in the vortex grows as time progresses. This particle overdensity will not drift at the standard radial drift rate, but rather with the slower migration rate of the vortex.

Because we use unstratified gas simulations we overestimate the amount of particles by a factor $\sqrt{2\pi}$. Compared to studies for streaming instability and gravo-turbulent planetesimal formation like Johansen et al. (2009) our $\varepsilon_0 = 0.01$ rather corresponds to $\varepsilon_0 = 0.02$. $\varepsilon_0 = 0.02$ is the dust-to-gas ratio Johansen et al. (2009) needed to trigger the streaming instability. We also see the streaming instability for this dust-to-gas ratio. However, we wanted to test whether streaming can still be triggered for lower ε_0 and smaller particle sizes than the ones used by Johansen et al. (2009).

The vortices are no longer destroyed when $\varepsilon_0 = 10^{-3}$ or $\varepsilon_0 = 10^{-4}$. Instead they remain stable over the simulation period, and accumulate particles. Although the concentration remains below the high concentrations of $\varepsilon_0 = 0.01$ they still reach local $\varepsilon > 1.0$ and with that, triggering the streaming instability.

To determine whether the local particle density enhancements can cause gravitational collapse were we to turn on particle self-gravity, we compare their density with the Roche density. Depending on disk model and radial position in the disk we see that even $St = 0.05$ particles with a high initial dust-to-gas ratio or $St = 1.0$ particles with $\varepsilon_0 = 10^{-4}$ can exceed the Roche density and thus can form a gravitationally bound object.

We conclude that baroclinic vortices in 3D are an efficient mechanism for trapping and concentrating particles. We can trigger streaming instability for smaller particle sizes and lower initial dust-to-gas ratios than in previous studies (e.g. Johansen et al., 2006b, 2009). This is an important step towards gravitational collapse.

Chapter 6

Conclusion

In this thesis we started by calculating disk properties for baroclinic disks around young stars. Our 1+1D model uses the assumption of a constant mass accretion rate and constant α. The temperature profile considers both, accretion luminosity and irradiation, and varies radially due to radially changing opacities. As input for $\dot{M}$ and α we used data from the Ophiuchus star forming region obtained by Andrews et al. (2009, 2010). We derived Richardson numbers that are negative, yet $\mid Ri \mid \ll 1.0$, heat diffusivities based on flux limited diffusion between $\tau_{\rm diff} = 0.1$ and $\tau_{\rm diff} = 100$ local orbits, as well as radial entropy gradient up to $\beta = \sqrt{\beta_K \beta_p} = 1.0$. These results provide the parameter range for our numerical experiments.

After that we conducted a comprehensive parameter study of the baroclinic instability / baroclinic vortex amplification with varying entropy gradients β, thermal cooling $\tau_{\rm cool}$ and diffusion times $\tau_{\rm diff}$. We found that the vortex amplification mechanism works well for all tested values of β ($\beta = 2.0$, 1.0, 0.5). The amplification rate is proportional to β^2, which emphasizes that baroclinic vortex amplification is indeed a nonlinear process. This proportionality also means that it takes much longer until vortices with a more realistic value of $\beta \approx 0.5$ reach a fully grown saturated state compared to high $\beta = 2.0$ configurations. The values of $\tau_{\rm cool}$ and $\tau_{\rm diff}$ have only a minor effect on the saturation values, e.g. enstrophy or α. The value of $\tau_{\rm cool}$ affects the amplification rate and $\tau_{\rm diff}$ the saturation values. We measure values of the angular momentum transport of up to $\alpha \approx 10^{-2}$, but mostly around $\alpha \approx 10^{-3}$. These values are comparable to values from MRI simulations and only depend weakly on the entropy gradient like $\alpha \propto \beta - 1/2$.

An open question for planetesimal formation is still the local enhancement of dust densities above the solar dust-to-gas ratio of 10^{-2}. As Johansen et al. (2009) showed, simple vertical sedimentation is not sufficient to increase the dust-to-gas ratio ε enough to trigger streaming instability and gravitational

collapse. Other methods to further increase local dust concentration are zonal flows (Johansen et al., 2011) or, in our case, vortex trapping.

In our 2 dimensional models of the baroclinic instability we looked for the particle concentration of particles with sizes $St = 0.01$, $St = 0.05$, $St = 1.0$ and $St = 20.0$. If we do not include particle feedback onto the gas, we see that there are high concentrations of particles in the vortices, except for $St = 20.0$ particles. For $St = 0.05$ and $St = 1.0$ particles all particle were eventually trapped in the vortex. The high concentrations mean that back-reaction onto the gas is not negligible. With the feedback mechanism included, we still see high dust concentrations inside the vortex. The limit of $\varepsilon \approx 1.0$ for streaming instability is passed for all particle sizes, except for $St = 20.0$ particles which do not accumulate in vortices. As the particle concentration rises, the growth times for streaming get faster. For $St = 1.0$ particles, the concentration of dust particles gets so high that the vortex structure is strongly perturbed. With the dust concentrating forces dropping, the high particle concentration decreases. This cycle constantly repeats itself. Smaller particles also concentrate high enough to trigger the streaming instability. They spread out over the entire vortex with strong density fluctuations. Even if we decrease the initial dust-to-gas ratio down to $\varepsilon_0 = 10^{-3}$ or $\varepsilon_0 = 10^{-4}$ we still get the same overdensities, even for our smallest particle sizes, which shows that baroclinic vortices are efficient particle traps.

When we compare our collisional velocities to analytical studies that use Kolmogorov turbulence, such as Ormel and Cuzzi (2007), we see that our velocities are about one order of magnitude lower than expected based on α. This means that, despite the strength of angular momentum transport which is comparable to other instabilities, baroclinic vortices provide a gentler environment for particles.

Our 3 dimensional unstratified gas simulations lead to the same conclusions as previous studies by Lesur and Papaloizou (2010) and Lyra and Klahr (2011). A vortex column develops and at some point the elliptical instability sets in. Eventually, a stable balance between vortex perturbation due to elliptical instability and vortex driving due to baroclinic effects is reached.

When we included particles feeling vertical gravity with an $\varepsilon_0 = 0.01$ we saw that, due to the sedimentation and the resulting high dust densities in the mid-plane, the streaming instability is triggered and that the vortex is destroyed at the mid-plane. Yet in the upper and lower parts of the simulation box the vortex column remains stable. The particle overdensities in the mid-plane still follow the radial motion of the remaining vortex column.

As in the 2D simulations we decreased the initial dust-to-gas ratio to $\varepsilon_0 = 10^{-3}$ and $\varepsilon_0 = 10^{-4}$. There we saw that the vortex column is no longer destroyed, and the particle trapping mechanism of the vortex sets in. Although

the overdensities reached are lower than for $\varepsilon_0 = 0.01$, we still reach dust-to-gas ratios of $\varepsilon > 1.0$ and thus trigger the streaming instability.

To estimate if the reached overdensities can be held together solely by their own gravity we estimate the Roche density at different radii. Depending on disk model and radial location of the particle clump we do reach dust densities higher than the Roche density. If self-gravity was included for the dust then gravitational collapse would occur.

Overall, we conclude that baroclinic vortices are a feasible mechanism for transporting angular momentum in the dead zone of a protoplanetary accretion disk, here we define dead zone as the region of the disk where the magnetic diffusive time is smaller than the dynamical time and therefore no MRI can operate. When particles are included, they are efficiently captured by the vortices in 2D as well as in 3D simulations. Even for low initial dust-to-gas ratios and small particle sizes we can reach dust accumulations that trigger the streaming instability and with that fulfill a necessary condition for gravitational collapse. Previous studies of particle concentration had to use higher initial dust-to-gas ratios and/or larger particles.

Yet our high-resolution studies are limited to 2 dimensions without particles. Especially our 3D studies lack proper resolution and realistic entropy gradients. In the future additional studies with higher resolution and self gravity have to be conducted. Also global simulations will be helpful to better study effects such as vortex migration.

Appendix A

Variables and Symbols

Table A.1. Variables and Symbols

Variables and Symbols	Description
h	dimensionless pressure scale-height
H	pressure scale-height
H_d	particle scale-height
H_g	particle scale-height
r	distance to star
R_0	co-rotational radius
a	vortex radius
s	particle radius
r_0	reference radius
dx	impact parameter
r_n	normal distance to impact plane
$\boldsymbol{r}_i$	vectorial position of particle i
$R_\star$	stelar radius
$R_\odot$	Solar radius
R_c	radius od particle clump
$\boldsymbol{u}$	gas velocity
$u_y^{(0)} = 3/2\Omega_0 x$	shear velocity
q	shear parameter
u_K	Keplerian velocity
$\boldsymbol{v}$	particle velocity
$\boldsymbol{v}_i$	vectorial velocity of particle i
v_coll	collision velocity
Δv_{ij}	relative velocity of particles i and j
c_s	sound speed
c Ch. 2 & 3	speed of light
t	time
t_s	vertical settling time
τ_s	particle friction time
Ω	orbital frequency
Ω_0	orbital frequency at co-rotaional radius
ρ, ρ_g	gas density
$\rho_{\mathrm{g},0}$	initial gas density
ρ_0	background density
ρ'	applied density perturbation
ρ_d	dust density
$\rho_{\mathrm{d},0}$	initial dust density

Table A.1 (cont'd)

Variables and Symbols	Description
ρ_s	material density of solids
ρ_R	Roche density
ρ_crit	critical density
β_ρ	gas/dust density gradient
$\Sigma, \Sigma_\mathrm{g}$	gas surface density
$\Sigma_\mathrm{g,0}$	gas surface density
Σ_d	dust surface density
$\Sigma_\mathrm{d,0}$	dust surface density
Σ_0	gas surface density at reference radius
β_Σ	surface density gradient
$M_\star$	mass of central object
M_p	mass of one super-particle
M_g	total mass of gas in simulation domain
M_d	total mass of dust in simulation domain
M_v	total mass of dust captured in vortex
M_c	mass of particle clump
$M_\odot$	Solar mass
M_Earth	mass of the earth
$\dot{M}$	mass accretion rate
p Ch 2	vertically integrated pressure
p	deviation from background pressure
p_0	initial mean pressure
$\bar{p}$	time independent pressure
$p_\mathrm{tot} = \bar{p} + p$	total pressure
β_p	pressure gradient
s	entropy
β_s	entropy gradient
β	entropy/pressure gradient
K	potential temperature
β_K	gradient of potential temperature
ω_z	vertical component of vorticty
$\omega_{z,\mathrm{min}}$	minimum vorticity
ω_z^2	enstrophy
τ_cool	thermal cooling time
τ_diff	thermal diffusion time
τ_α	decay time of α

Table A.1 (cont'd)

Variables and Symbols	Description
$\tau_{\omega_z^2}$	decay time of vorticity
τ	vortex amplification-time
Γ	vortex amplification-time
St	Stokes-number
$\varepsilon = \rho_\mathrm{d}/\rho_\mathrm{g} = (2\mathrm{D})\Sigma_\mathrm{d}/\Sigma_\mathrm{g}$	dust-to-gas-ratio
$\varepsilon_0 = \rho_{\mathrm{d},0}/\rho_{\mathrm{g},0} = (2\mathrm{D})\Sigma_{\mathrm{d},0}/\Sigma_{\mathrm{g},0}$	initial dust-to-gas-ratio
ε_max	maximum dust-to-gas ratio
$c = \rho_\mathrm{d}/\rho_{\mathrm{d},0} = \Sigma_\mathrm{d}/\Sigma_{\mathrm{d},0}$ Ch. 4 & 5	concentration
η	velocity offset between dust and gas velocities
T	temperature
T_0	reference temperature
T_acc	accretion temperature
T_irr	irradiation temperature
T_eff	effective temperature
T_c	mid-plane emperature
$T_\star$	stelar temperature
β_T	temperature gradient
F_acc	accretion flux
F_irr	irradiative flux
F_eff	effective flux
ν	viscosity
α	Shakura-Sunyaev α-parameter
D Ch. 2 & 3	diffusion constant
D Ch. 5	vertical diffusion coefficient
δ	α analogon for vertical diffusion
E_kin	kinetic energy
f_p, $f_{p,s}$	pressure force per unit mass
g_z	vertical gravitational acceleration
$a_{s,z}$	vertical component of drag acceleration
a_t	tangential acceleration
$a_{g,\mathrm{c}}$	gravitational acceleration on particle clump
c_p	specific heat at constant pressure
c_v	specific heat at constant volume
$\gamma = c_p/c_v$	adiabatic index
j	specific angular momentum
N	Brunt-Väisälä frequency

Table A.1 (cont'd)

Variables and Symbols	Description
Sc_z	vertical Schmidt-number
G	gravitational constant
κ	oppacity
τ_{R}	Rosseland mean oppacity
Q	Toomre-parameter
λ	flux limitter
a_R	radiation constant
σ Ch. 2	Stefan-Boltzmann constant
σ Ch. 3 & 5	width of initial density perturbation
σ_{d}	width of initial particle distribution
f_D	6th order hyper-diffusivity
f_ν	6th order hyper-viscosity
f_K	6th order hyper-conductivity
L_x, L_y, L_y	box dimension in x, y, z direction
n_x, n_y, n_z	amount of grid-cells in x, y, z direction
k_x, k_y, k_z	number of modes in x, y, z direction

Bibliography

Andrews, S. M., Wilner, D. J., Hughes, A. M., Qi, C., and Dullemond, C. P. (2009). Protoplanetary Disk Structures in Ophiuchus. *ApJ*, 700:1502–1523.

Andrews, S. M., Wilner, D. J., Hughes, A. M., Qi, C., and Dullemond, C. P. (2010). Protoplanetary Disk Structures in Ophiuchus. II. Extension to Fainter Sources. *ApJ*, 723:1241–1254.

Armitage, P. J. (2009). *Astrophysics of Planet Formation*.

Balbus, S. A. and Hawley, J. F. (1991). A powerful local shear instability in weakly magnetized disks. I - Linear analysis. II - Nonlinear evolution. *ApJ*, 376:214–233.

Balbus, S. A. and Hawley, J. F. (1998). Instability, turbulence, and enhanced transport in accretion disks. *Reviews of Modern Physics*, 70:1–53.

Barge, P. and Sommeria, J. (1995). Did planet formation begin inside persistent gaseous vortices? *A&A*, 295:L1–L4.

Bate, M. R., Lubow, S. H., Ogilvie, G. I., and Miller, K. A. (2003). Three-dimensional calculations of high- and low-mass planets embedded in protoplanetary discs. *MNRAS*, 341:213–229.

Bell, K. R., Cassen, P. M., Klahr, H. H., and Henning, T. (1997). The Structure and Appearance of Protostellar Accretion Disks: Limits on Disk Flaring. *ApJ*, 486:372.

Bell, K. R. and Lin, D. N. C. (1994). Using FU Orionis outbursts to constrain self-regulated protostellar disk models. *ApJ*, 427:987–1004.

Birnstiel, T., Dullemond, C. P., and Brauer, F. (2010). Gas- and dust evolution in protoplanetary disks. *A&A*, 513:A79.

Birnstiel, T., Klahr, H., and Ercolano, B. (2012). A simple model for the evolution of the dust population in protoplanetary disks. *A&A*, 539:A148.

Blum, J. and Wurm, G. (2008). The Growth Mechanisms of Macroscopic Bodies in Protoplanetary Disks. *Annu.Rev.Astron.Astrophys.*, 46:21–56.

Boss, A. P. (1997). Giant planet formation by gravitational instability. *Science, Vol. 276, No. 5320, p. 1836 - 1839*, 276:1836–1839.

Boss, A. P. (2000). Possible Rapid Gas Giant Planet Formation in the Solar Nebula and Other Protoplanetary Disks. *ApJL*, 536:L101–L104.

Boss, A. P. (2007). Testing Disk Instability Models for Giant Planet Formation. *ApJL*, 661:L73–L76.

Brauer, F., Dullemond, C. P., and Henning, T. (2008). Coagulation, fragmentation and radial motion of solid particles in protoplanetary disks. *A&A*, 480:859–877.

Cabot, W. (1984). The nonaxisymmetric baroclinic instability in thin accretion disks. *ApJ*, 277:806–812.

Calvet, N., Hartmann, L., and Strom, S. E. (2000). Evolution of Disk Accretion. *Protostars and Planets IV*, page 377.

Cameron, A. G. W. (1962). The formation of the sun and planets. *Icarus*, 1:13–69.

Carballido, A., Cuzzi, J. N., and Hogan, R. C. (2010). Relative velocities of solids in a turbulent protoplanetary disc. *MNRAS*, 405:2339–2344.

Cerretelli, C. and Williamson, C. H. K. (2003). The physical mechanism for vortex merging. *Journal of Fluid Mechanics*, 475:41–77.

Chamberlin, T. C. (1901). On a Possible Function of Disruptive Approach in the Formation of Meteorites, Comets, and NEBUL&AElig. *ApJ*, 14:17.

Chamberlin, T. C. (1916). The Planetesimal Hypothesis. *Journal of the Royal Astronomical Society of Canada*, 10:473.

Chang, P. and Oishi, J. S. (2010). On the Stability of Dust-laden Protoplanetary Vortices. *ApJ*, 721:1593–1602.

Chavanis, P. H. (2000). Trapping of dust by coherent vortices in the solar nebula. *A&A*, 356:1089–1111.

Chiang, E. I. and Goldreich, P. (1997). Spectral Energy Distributions of T Tauri Stars with Passive Circumstellar Disks. *ApJ*, 490:368.

Chiang, E. I. and Goldreich, P. (1999). Spectral Energy Distributions of Passive T Tauri Disks: Inclination. *ApJ*, 519:279–284.

Cuzzi, J. N., Dobrovolskis, A. R., and Hogan, R. C. (1994). Turbulent diffusion and concentration of chondrules in the protoplanetary nebula. *LPI Contributions*, 844:6–7.

D'Alessio, P., Calvet, N., and Hartmann, L. (2001). Accretion Disks around Young Objects. III. Grain Growth. *ApJ*, 553:321–334.

D'Alessio, P., Calvet, N., Hartmann, L., Lizano, S., and Cantó, J. (1999). Accretion Disks around Young Objects. II. Tests of Well-mixed Models with ISM Dust. *ApJ*, 527:893–909.

D'Alessio, P., Canto, J., Calvet, N., and Lizano, S. (1998). Accretion Disks around Young Objects. I. The Detailed Vertical Structure. *ApJ*, 500:411.

Davidson, P. A. (2004). *Turbulence : an introduction for scientists and engineers*.

Dominik, C. and Tielens, A. G. G. M. (1997). The Physics of Dust Coagulation and the Structure of Dust Aggregates in Space. *ApJ*, 480:647.

Dubrulle, B., Morfill, G., and Sterzik, M. (1995). The dust subdisk in the protoplanetary nebula. *Icarus*, 114:237–246.

Dullemond, C. P., Apai, D., and Walch, S. (2006). Crystalline Silicates as a Probe of Disk Formation History. *ApJL*, 640:L67–L70.

Dullemond, C. P. and Dominik, C. (2005). Dust coagulation in protoplanetary disks: A rapid depletion of small grains. *A&A*, 434:971–986.

Dullemond, C. P., Hollenbach, D., Kamp, I., and D'Alessio, P. (2007). Models of the Structure and Evolution of Protoplanetary Disks. *Protostars and Planets V*, pages 555–572.

Dzyurkevich, N., Flock, M., Turner, N. J., Klahr, H., and Henning, T. (2010). Trapping solids at the inner edge of the dead zone: 3-D global MHD simulations. *A&A*, 515:A70.

Flock, M., Dzyurkevich, N., Klahr, H., Turner, N. J., and Henning, T. (2011). Turbulence and Steady Flows in Three-dimensional Global Stratified Magnetohydrodynamic Simulations of Accretion Disks. *ApJ*, 735:122.

Fromang, S., Lyra, W., and Masset, F. (2011). Meridional circulation in turbulent protoplanetary disks. *A&A*, 534:A107.

Fromang, S. and Papaloizou, J. (2006). Dust settling in local simulations of turbulent protoplanetary disks. *A&A*, 452:751–762.

Gammie, C. F. (1996). Layered Accretion in T Tauri Disks. *ApJ*, 457:355.

Godon, P. and Livio, M. (1999). Vortices in Protoplanetary Disks. *ApJ*, 523:350–356.

Goldreich, P. and Lynden-Bell, D. (1965). I. Gravitational stability of uniformly rotating disks. *MNRAS*, 130:97.

Goldreich, P. and Ward, W. R. (1973). The Formation of Planetesimals. *ApJ*, 183:1051–1062.

Güttler, C., Blum, J., Zsom, A., Ormel, C. W., and Dullemond, C. P. (2010). The outcome of protoplanetary dust growth: pebbles, boulders, or planetesimals?. I. Mapping the zoo of laboratory collision experiments. *A&A*, 513:A56.

Haisch, Jr., K. E., Lada, E. A., and Lada, C. J. (2001). Disk Frequencies and Lifetimes in Young Clusters. *ApJL*, 553:L153–L156.

Hartmann, L., Calvet, N., Gullbring, E., and D'Alessio, P. (1998). Accretion and the Evolutiion of T Tauri Disks. *ApJ*, 495:385.

Hoyle, F. (1960). The Origin of the Solar Nebula. *QJRAS*, 1:28.

Hubeny, I. (1990). Vertical structure of accretion disks - A simplified analytical model. *ApJ*, 351:632–641.

Janson, M., Bonavita, M., Klahr, H., and Lafrenière, D. (2012). How do Most Planets Form? - Constraints on Disk Instability from Direct Imaging. *ApJ*, 745:4.

Jeans, J. (1931a). Contributions to a British Association Discussion on the Evolution of the Universe. *Nature*, 128:701–704.

Jeans, J. H. (1931b). Stellar Structure. *Nature*, 127:89.

Ji, H., Burin, M., Schartman, E., and Goodman, J. (2006). Hydrodynamic turbulence cannot transport angular momentum effectively in astrophysical disks. *Nature*, 444:343–346.

Johansen, A., Andersen, A. C., and Brandenburg, A. (2004). Simulations of dust-trapping vortices in protoplanetary discs. *A&A*, 417:361–374.

Johansen, A., Klahr, H., and Henning, T. (2006a). Gravoturbulent Formation of Planetesimals. *ApJ*, 636:1121–1134.

Johansen, A., Klahr, H., and Henning, T. (2011). High-resolution simulations of planetesimal formation in turbulent protoplanetary discs. In A. Sozzetti, M. G. Lattanzi, & A. P. Boss, editor, *IAU Symposium*, volume 276 of *IAU Symposium*, pages 89–94.

Johansen, A., Klahr, H., and Mee, A. J. (2006b). Turbulent diffusion in protoplanetary discs: the effect of an imposed magnetic field. *MNRAS*, 370:L71–L75.

Johansen, A., Oishi, J. S., Mac Low, M.-M., Klahr, H., Henning, T., and Youdin, A. (2007). Rapid planetesimal formation in turbulent circumstellar disks. *Nature*, 448:1022–1025.

Johansen, A. and Youdin, A. (2007). Protoplanetary Disk Turbulence Driven by the Streaming Instability: Nonlinear Saturation and Particle Concentration. *ApJ*, 662:627–641.

Johansen, A., Youdin, A., and Mac Low, M.-M. (2009). Particle Clumping and Planetesimal Formation Depend Strongly on Metallicity. *ApJL*, 704:L75–L79.

Johnson, B. M. and Gammie, C. F. (2005). Vortices in Thin, Compressible, Unmagnetized Disks. *ApJ*, 635:149–156.

Kant, I. (1755). *Allgemeine Naturgeschichte und Theorie des Himmels*.

Kerswell, R. R. (2002). Elliptical instability. *Annual Review of Fluid Mechanics*, 34:83–113.

Klahr, H. (2004). The Global Baroclinic Instability in Accretion Disks. II. Local Linear Analysis. *ApJ*, 606:1070–1082.

Klahr, H. and Lin, D. N. C. (2005). Dust Distribution in Gas Disks. II. Self-induced Ring Formation through a Clumping Instability. *ApJ*, 632:1113–1121.

Klahr, H. H. and Bodenheimer, P. (2003). Turbulence in Accretion Disks: Vorticity Generation and Angular Momentum Transport via the Global Baroclinic Instability. *ApJ*, 582:869–892.

Klahr, H. H. and Henning, T. (1997). Particle-Trapping Eddies in Protoplanetary Accretion Disks. *Icarus*, 128:213–229.

Klahr, H. H. and Lin, D. N. C. (2001). Dust Distribution in Gas Disks: A Model for the Ring around HR 4796A. *ApJ*, 554:1095–1109.

Kley, W., Bitsch, B., and Klahr, H. (2009). Planet migration in three-dimensional radiative discs. *A&A*, 506:971–987.

Knobloch, E. and Spruit, H. C. (1986). Baroclinic waves in a vertically stratified thin accretion disk. *A&A*, 166:359–367.

Korotaev, G. K. (1997). Radiating Vortices in Geophysical Fluid Dynamics. *Surveys in Geophysics*, 18:567–618.

Kozai, Y. (1962). Secular perturbations of asteroids with high inclination and eccentricity. *AJ*, 67:591.

Laplace, P. S. and Young, T. (1832). *Elementary illustrations of the celestial mechanics of Laplace.*

Lesur, G. and Papaloizou, J. C. B. (2009). On the stability of elliptical vortices in accretion discs. *A&A*, 498:1–12.

Lesur, G. and Papaloizou, J. C. B. (2010). The subcritical baroclinic instability in local accretion disc models. *A&A*, 513:A60.

Li, H., Colgate, S. A., Wendroff, B., and Liska, R. (2001). Rossby Wave Instability of Thin Accretion Disks. III. Nonlinear Simulations. *ApJ*, 551:874–896.

Li, H., Finn, J. M., Lovelace, R. V. E., and Colgate, S. A. (2000). Rossby Wave Instability of Thin Accretion Disks. II. Detailed Linear Theory. *ApJ*, 533:1023–1034.

Lithwick, Y. and Naoz, S. (2011). The Eccentric Kozai Mechanism for a Test Particle. *ApJ*, 742:94.

Lovelace, R. V. E., Li, H., Colgate, S. A., and Nelson, A. F. (1999). Rossby Wave Instability of Keplerian Accretion Disks. *ApJ*, 513:805–810.

Lüst, R. and Schlüter, A. (1955). Drehimpulstransport durch Magnetfelder und die Abbremsung rotierender Sterne. Mit 4 Textabbildungen. *Zeitschrift für Astrophysik*, 38:190.

Lynden-Bell, D. and Pringle, J. E. (1974). The evolution of viscous discs and the origin of the nebular variables. *MNRAS*, 168:603–637.

Lyra, W., Johansen, A., Klahr, H., and Piskunov, N. (2008). Global magnetohydrodynamical models of turbulence in protoplanetary disks. I. A cylindrical potential on a Cartesian grid and transport of solids. *A&A*, 479:883–901.

Lyra, W., Johansen, A., Zsom, A., Klahr, H., and Piskunov, N. (2009). Planet formation bursts at the borders of the dead zone in 2D numerical simulations of circumstellar disks. *A&A*, 497:869–888.

Lyra, W. and Klahr, H. (2011). The baroclinic instability in the context of layered accretion. Self-sustained vortices and their magnetic stability in local compressible unstratified models of protoplanetary disks. *A&A*, 527:A138.

Lyra, W. and Mac Low, M.-M. (2012). Rossby wave instability at dead zone boundaries in 3D resistive magnetohydrodynamical global models of protoplanetary disks. *ArXiv e-prints*.

Masset, F. S. (2002). The co-orbital corotation torque in a viscous disk: Numerical simulations. *A&A*, 387:605–623.

Mathis, J. S., Rumpl, W., and Nordsieck, K. H. (1977). The size distribution of interstellar grains. *ApJ*, 217:425–433.

Mayor, M. and Queloz, D. (1995). A Jupiter-mass companion to a solar-type star. *Nature*, 378:355–359.

Meru, F. and Bate, M. R. (2010). Exploring the conditions required to form giant planets via gravitational instability in massive protoplanetary discs. *MNRAS*, 406:2279–2288.

Mizuno, H. (1980). Formation of the Giant Planets. *Progress of Theoretical Physics, Vol. 64, No. 2, pp. 544-557*, 64:544–557.

Moffat, A. F. J. (1969). A Theoretical Investigation of Focal Stellar Images in the Photographic Emulsion and Application to Photographic Photometry. *A&A*, 3:455.

Mordasini, C., Alibert, Y., and Benz, W. (2009). Extrasolar planet population synthesis. I. Method, formation tracks, and mass-distance distribution. *A&A*, 501:1139–1160.

Moulton, F. R. (1905). On the Evolution of the Solar System. *ApJ*, 22:165.

Nakagawa, Y., Sekiya, M., and Hayashi, C. (1986). Settling and growth of dust particles in a laminar phase of a low-mass solar nebula. *Icarus*, 67:375–390.

Natta, A., Meyer, M. R., and Beckwith, S. V. W. (2000). Silicate Emission in T Tauri Stars: Evidence for Disk Atmospheres? *ApJ*, 534:838–845.

Oishi, J. S. and Mac Low, M.-M. (2009). On Hydrodynamic Motions in Dead Zones. *ApJ*, 704:1239–1250.

Okuzumi, S. (2009). Electric Charging of Dust Aggregates and its Effect on Dust Coagulation in Protoplanetary Disks. *ApJ*, 698:1122–1135.

Okuzumi, S., Tanaka, H., Takeuchi, T., and Sakagami, M.-a. (2011a). Electrostatic Barrier Against Dust Growth in Protoplanetary Disks. I. Classifying the Evolution of Size Distribution. *ApJ*, 731:95.

Okuzumi, S., Tanaka, H., Takeuchi, T., and Sakagami, M.-a. (2011b). Electrostatic Barrier Against Dust Growth in Protoplanetary Disks. II. Measuring the Size of the "Frozen" Zone. *ApJ*, 731:96.

Ormel, C. W. and Cuzzi, J. N. (2007). Closed-form expressions for particle relative velocities induced by turbulence. *A&A*, 466:413–420.

Ormel, C. W., Dullemond, C. P., and Spaans, M. (2010). Accretion among preplanetary bodies: The many faces of runaway growth. *Icarus*, 210:507–538.

Paardekooper, S.-J., Lesur, G., and Papaloizou, J. C. B. (2010). Vortex Migration in Protoplanetary Disks. *ApJ*, 725:146–158.

Papaloizou, J. and Lin, D. N. C. (1984). On the tidal interaction between protoplanets and the primordial solar nebula. I - Linear calculation of the role of angular momentum exchange. *ApJ*, 285:818–834.

Papaloizou, J. C. B., Nelson, R. P., Kley, W., Masset, F. S., and Artymowicz, P. (2007). Disk-Planet Interactions During Planet Formation. *Protostars and Planets V*, pages 655–668.

Papaloizou, J. C. B. and Pringle, J. E. (1984). The dynamical stability of differentially rotating discs with constant specific angular momentum. *MNRAS*, 208:721–750.

Papaloizou, J. C. B. and Pringle, J. E. (1985). The dynamical stability of differentially rotating discs. II. *MNRAS*, 213:799–820.

Pascucci, I., Wolf, S., Steinacker, J., Dullemond, C. P., Henning, T., Niccolini, G., Woitke, P., and Lopez, B. (2004). The 2D continuum radiative transfer problem. Benchmark results for disk configurations. *A&A*, 417:793–805.

Petersen, M. R., Julien, K., and Stewart, G. R. (2007a). Baroclinic Vorticity Production in Protoplanetary Disks. I. Vortex Formation. *ApJ*, 658:1236–1251.

Petersen, M. R., Stewart, G. R., and Julien, K. (2007b). Baroclinic Vorticity Production in Protoplanetary Disks. II. Vortex Growth and Longevity. *ApJ*, 658:1252–1263.

Pollack, J. B., Hubickyj, O., Bodenheimer, P., Lissauer, J. J., Podolak, M., and Greenzweig, Y. (1996). Formation of the Giant Planets by Concurrent Accretion of Solids and Gas. *Icarus*, 124:62–85.

Rice, W. K. M., Lodato, G., and Armitage, P. J. (2005). Investigating fragmentation conditions in self-gravitating accretion discs. *MNRAS*, 364:L56–L60.

Rüdiger, G., Arlt, R., and Shalybkov, D. (2002). Hydrodynamic stability in accretion disks under the combined influence of shear and density stratification. *A&A*, 391:781–787.

Safronov, V. S. (1972). *Evolution of the protoplanetary cloud and formation of the earth and planets.*

Schartman, E., Ji, H., Burin, M. J., Cutler, R., Heitzenroeder, P., Liu, W., Raftopoulos, S., Waksman, J., Goodman, J., Stone, J., and Kageyama, A. (2006). Princeton MagnetoRotational Instability (MRI) Experiment: Overview and Recent Progress in the Search for the MRI. In *American Astronomical Society Meeting Abstracts #207*, volume 207 of *American Astronomical Society Meeting Abstracts*, page 211.07.

Shakura, N. I. and Sunyaev, R. A. (1973). Black holes in binary systems. Observational appearance. *A&A*, 24:337–355.

Sicilia-Aguilar, A., Hartmann, L., Calvet, N., Megeath, S. T., Muzerolle, J., Allen, L., D'Alessio, P., Merín, B., Stauffer, J., Young, E., and Lada, C. (2006a). Disk Evolution in Cep OB2: Results from the Spitzer Space Telescope. *ApJ*, 638:897–919.

Sicilia-Aguilar, A., Hartmann, L. W., Fürész, G., Henning, T., Dullemond, C., and Brandner, W. (2006b). High-Resolution Spectroscopy in Tr 37: Gas Accretion Evolution in Evolved Dusty Disks. *AJ*, 132:2135–2155.

Tanaka, H., Himeno, Y., and Ida, S. (2005). Dust Growth and Settling in Protoplanetary Disks and Disk Spectral Energy Distributions. I. Laminar Disks. *ApJ*, 625:414–426.

Tanaka, H., Takeuchi, T., and Ward, W. R. (2002). Three-Dimensional Interaction between a Planet and an Isothermal Gaseous Disk. I. Corotation and Lindblad Torques and Planet Migration. *ApJ*, 565:1257–1274.

Tassoul, J.-L. (2000). *Stellar Rotation*. Cambridge University Press.

Terebey, S., Shu, F. H., and Cassen, P. (1984). The collapse of the cores of slowly rotating isothermal clouds. *ApJ*, 286:529–551.

Thommes, E. W., Duncan, M. J., and Levison, H. F. (2003). Oligarchic growth of giant planets. *Icarus*, 161:431–455.

Toomre, A. (1964). On the gravitational stability of a disk of stars. *ApJ*, 139:1217–1238.

Turner, N. J. and Drake, J. F. (2009). Energetic Protons, Radionuclides, and Magnetic Activity in Protostellar Disks. *ApJ*, 703:2152–2159.

Vallis, G. K. (2006). *Atmospheric and Oceanic Fluid Dynamics*.

Varnière, P. and Tagger, M. (2006). Reviving Dead Zones in accretion disks by Rossby vortices at their boundaries. *A&A*, 446:L13–L16.

Velikov, E. (1959). *Soviet Physics JETP*, 995(9):36.

Ward, W. R. (1997). Protoplanet Migration by Nebula Tides. *Icarus*, 126:261–281.

Weidenschilling, S. J. (1977a). Aerodynamics of solid bodies in the solar nebula. *MNRAS*, 180:57–70.

Weidenschilling, S. J. (1977b). The distribution of mass in the planetary system and solar nebula. *Ap&SS*, 51:153–158.

Weidenschilling, S. J. (1980). Dust to planetesimals - Settling and coagulation in the solar nebula. *Icarus*, 44:172–189.

Weidenschilling, S. J. and Davis, D. R. (1985). Orbital resonances in the solar nebula - Implications for planetary accretion. *Icarus*, 62:16–29.

Weizsäcker, C. F. V. (1943). Über die Entstehung des Planetensystems. Mit 2 Abbildungen. *Zeitschrift für Astrophysik*, 22:319.

Wetherill, G. W. and Stewart, G. R. (1989). Accumulation of a swarm of small planetesimals. *Icarus*, 77:330–357.

Williamson, J. H. (1980). Low-Storage Runge-Kutta Schemes. *Journal of Computational Physics*, 35:48.

Wurm, G. and Blum, J. (2000). An Experimental Study on the Structure of Cosmic Dust Aggregates and Their Alignment by Motion Relative to Gas. *ApJL*, 529:L57–L60.

Youdin, A. and Johansen, A. (2007). Protoplanetary Disk Turbulence Driven by the Streaming Instability: Linear Evolution and Numerical Methods. *ApJ*, 662:613–626.

Youdin, A. N. and Goodman, J. (2005). Streaming Instabilities in Protoplanetary Disks. *ApJ*, 620:459–469.

Zsom, A., Ormel, C. W., Güttler, C., Blum, J., and Dullemond, C. P. (2010). The outcome of protoplanetary dust growth: pebbles, boulders, or planetesimals? II. Introducing the bouncing barrier. *A&A*, 513:A57.

Acknowledgements

The simulations for this thesis were performed on the Theo cluster of the Max Planck Society in Garching and on the BlueGene/P cluster at the Forschungszentrum Jülich under the project number HHD19.

Thanks to IMPRS-HD and the DFG Forschergruppe 759: "The Formation of Planets: The Critical First Growth Phase" for travel support.

And now to the more personal acknowledegments. Thank you, Prof. Henning and Hubert Klahr for giving me the opportunity to do this thesis at the MPIA. Especially to Hubert for supervising me the last 3+ years. There were quite a few meetings when I left his office knowing more than I did before I entered. Be it about science, numerics or movies.

A huge thank you also goes out to the theory groups of Hubert Klahr and Kees Dullemond for interesing discussions and a great work environment, especially to Mario Flock, Christoph Mordasini, Karsten Dittrich, Helen Morrison (also for watching Maggi when I was on trips), Kai-Martin Dittkrist, Andras Zsom and Til Birnstiel.

Most of this thesis was conducted with the PENCIL CODE which I had quite a few problems with in the beginning. So thanks to Wladimir Lyra and Anders Johansen for solving one or the other coding issue for me (or the confusion on my head). Also thank you Wlad, for introducing me to the Kade fellowship and bring me to the American Museum of Natural History for three month to work with you and Mordecai-Mark Mac Low. This time brought many experiences which I will never forget.

MPIA did not only offer a good working environment, but also other things. I especially enjoyed the half hour science free time at the students coffee or the occasional chat with Ina Beckmann or Frank Witzel. Thanks guys!

Most importantly I want to thank my parents. They have been supporting me my entire life and more or less everything I did. Thank you for letting me know that I can always count on you, for picking me up when I am down and encouraging me with "Halt die Ohren steif!"

Last but not least I want to thank Mathias Jäger, who over the last 2 years has made my life much more enjoyable and stable. I hope for many years to come.